Photonic crystal based widely tunable laser diodes and integrated optoelectronic components

Dissertation zur Erlangung des

naturwissenschaftlichen Doktorgrades

der Bayerischen Julius-Maximilians-Universität

Würzburg

vorgelegt von

Sven Mahnkopf

geboren in Berlin-Lichterfelde

Würzburg 2005

To my Wife and Family

Eingereicht am 20. Januar 2005
bei der Fakultät für Physik und Astronomie.

1. Gutachter: Prof. Dr. A. Forchel
2. Gutachter: Prof. Dr. J. Geurts
der Dissertation.

1. Prüfer: Prof. Dr. A. Forchel
2. Prüfer: Prof. Dr. J. Geurts
3. Prüfer: Prof. Dr. W. Kinzel
im Promotionskolloqium.

Tag des Promotionskolloqiums: 10. Juni 2005

Doktorurkunde ausgehändigt am: ....

Contents

Chapter 1
Summary / Zusammenfassung

1.1 Summary

In a first aspect of this work, the development of photonic crystal based widely tunable laser diodes and their monolithic integration with photonic crystal based passive waveguide and coupler structures is explored theoretically and experimentally. In these devices, the photonic crystal is operated in the photonic bandgap which can be used for the realization of effective reflectors and waveguide structures. Such tunable light sources are of great interest for the development of optical network systems that are based on wavelength division multiplexing. In a second aspect of this work, the operation of a photonic crystal block near the photonic band edge is investigated with respect to the so-called superprism effect. After a few introductory remarks that serve to motivate this work, chapter 3 recapitulates some aspects of semiconductor lasers and photonic crystals that are essential for the understanding of this work so that the reader should be readily equipped with the tools to appreciate the results presented in this work.

Operation of 2D photonic crystal in the bandgap: Reflectors

Operating a photonic crystal block such that the normalized frequency of the light propagating in the structure coincides with the location of the photonic bandgap, allows one to control the propagation of light on a very confined lateral area and thus facilitates a very high integration density of the optoelectronic circuitry. In a first aspect of this work, 2D PhC's are used as efficient reflectors in InP-based laser diodes to confine the propagation of light in the longitudinal direction while a planar waveguide geometry and a ridge waveguide structure provide transverse and lateral photon confinement, respectively. Novel widely tunable laser diodes

will be presented whose partial resonators are coupled through photonic crystal sections. The emission wavelength is discontinuously switched exploiting the so called Vernier effect: the relative shift of the longitudinal mode spectrum of one partial resonator against the other produces a discontinuous wavelength switching. A simultaneous shift of the partial resonators' longitudinal mode spectra results in a fine tuning of the emission wavelength. The lasers exhibit quasi-continuous tuning ranges of 25 nm and discontinuous tuning ranges of up to 50 nm. Maximum output powers are in the range of 6-9 mW and side mode suppression ratios are in the range of 30 dB. The design features a thermally limited 3 dB modulation bandwidth of approximately 11 GHz and linewidth in the range of 7 to 8 MHz.

In order to stabilize the output power over the tuning range of the laser, an amplifier section is monolithically integrated with the tunable laser source. Through an appropriate selection of bias currents into the amplifier section, it is possible to stabilize the laser's output power at 9 mW throughout the laser's tuning range.

Operation of 2D photonic crystal in the bandgap: PhC channel waveguides

In a second aspect of this work, photonic crystals are used to not only confine light in the longitudinal direction, but to provide full confinement of photons in the waveguide plane by introducing chains of defects in a photonic crystal slab to build laser resonators and to efficiently guide light around ultra-sharp waveguide bends. A photonic crystal coupled-cavity laser design will be presented that exhibits tuning ranges of 30 nm and side mode suppression ratios of up to 41 dB. Maximum output powers are in the range of 3 mW. Depending on the width of the photonic crystal channel waveguides constituting the laser resonators, external quantum efficiencies between 25 mW/A and 48 mW/A and threshold currents between 13 mA and 19 mA are reported experimentally. The design features a thermally limited 3 dB modulation bandwidth of 17 GHz and a linewidth of approximately 15 MHz. The switching characteristics of the device feature avoided crossings that stem from the coupling of the fundamental modes of the partial resonators at the photonic crystal interface. From a comparison of the theoretical

and experimentally observed energy gap of the avoided crossing, the losses of the photonic crystal intra-cavity coupling section can be estimated.

Furthermore, the propagation of light emitted from such laser sources through double bends composing a Y-coupler structure is investigated. The double bends form breaches in the periodicity of the photonic crystal channel waveguide that lead to reflections at the waveguide boundaries and possible couplings onto higher order modes (HOM). Since the HOM's exhibit higher losses compared to the fundamental mode, an escape mechanism for light propagating in the bend structure is opened producing signal attenuation. Different Y-coupler topologies are proposed and their transmission properties are experimentally compared with each other. It is found that the lowest signal attenuation of about 10 dB is observed for a coupler topology featuring high index contrast slit-like structures.

Operation of 2D photonic crystal near the bandgap: Superprism studies

Besides the obviously extraordinary properties of photonic crystals that stem from the existence of a photonic bandgap in which the propagation of light is prohibited, the investigation of the dispersion properties near the photonic bandgap is at least equally interesting. A small variation in the incident beam parameters, i.e. wavelength and incident angle, can result in a dramatic change of the isofrequency contour curvature and hence to various effects including beam collimation, beam focussing, and a significant change of the propagation direction of light inside the structure. The latter effect can lead to angular dispersions that exceed those of conventional bulk prism by several orders of magnitude and is therefore commonly referred to as the superprism effect. Chapter 6 initially provides some insight into the collimating and refractive properties of photonic crystals operated near the photonic bandgap. The superprism effect is then demonstrated for the examples of semicircular photonic crystal blocks with square and triangular lattice topologies and angular dispersions in the range of 0.5 °/nm are reported experimentally. It is furthermore investigated whether the introduction of a mode matching structure at the waveguide / photonic crystal interface can improve the transmission properties through the integrated structure. The performance of the superprism is found to not meet the requirements of wavelength division multi-

plexing applications with respect to resolution and signal attenuation. Concepts for an optimization of the design are discussed.

1.2 Zusammenfassung

In einem ersten Aspekt der vorliegenden Arbeit wird die Entwicklung von weit abstimmbaren Halbleiterlasern auf der Basis photonischer Kristalle sowie deren monolithische Integration mit passiven, auf photonischen Kristallen basierenden Wellenleiter- und Kopplerstrukturen theoretisch und experimentell untersucht. In diesen Bauelementen werden die photonischen Kristalle im Bereich der photonischen Bandlücke betrieben, was zur Realisierung effektiver Reflektoren und Wellenleiterstrukturen ausgenutzt werden kann. Kompakte, weit abstimmbare Halbleiterlaser sind für die Entwicklung von optischen Netzwerksystemen, die auf dem wavelength division multiplexing (WDM) beruhen, von fundamentaler Bedeutung. In einem zweiten Aspekt der Arbeit wird der Betrieb von photonischen Kristallen im Bereich der photonischen Bandkante im Hinblick auf den sogenannten Superprisma-Effekt untersucht.

Nach einigen einleitenden Worten, die diese Arbeit motivieren, werden in Kapitel 3 die für das Verständnis der Arbeit wesentlichen Grundlagen von Halbleiterlasern und photonischen Kristallen rekapituliert.

Betrieb des 2D photonischen Kristalls in der Bandlücke: Reflektoren

Der Betrieb eines photonischen Kristallblocks im Bereich der photonischen Bandlücke erlaubt die Kontrolle des sich im Halbleitermaterial ausbreitenden Lichts auf sehr engem Raum und ermöglicht mithin eine sehr hohe Integrationsdichte der optoelektronischen Bauelemente. Insbesondere kann die photonische Bandlücke dazu genutzt werden, photonische Kristalle als effektive Spiegel, zur lateralen Wellenleiterbegrenzung und zur Realisierung von sehr engen Wellenleiterknicken einzusetzen. Diese Eigenschaften werden in der vorliegenden Arbeit anhand von Experimenten untersucht. Es werden weit abstimmbare Laser demonstriert, deren Teilresonatoren durch photonische Kristallsegmente miteinander gekoppelt sind. Die Emissionswellenlänge wird mittels des sogenannten Vernier-Effekts diskontinuierlich abgestimmt: die Verschiebung des longitudinalen Modenspektrums eines Partialresonators relativ zu einem zweiten Resonator führt zu einem diskontuierlichen Schalten der Emissionswellenlänge. Eine simultane

Verschiebung der longitudinalen Modenspektren beider Partialresonatoren führt zu einer Feinabstimmung der Emissionswellenlänge. Die Laser weisen quasikontinuierliche Abstimmbereiche von 25 nm und diskontinuierliche Abstimmbereiche von bis zu 50 nm auf. Maximale Ausgangsleistungen sind im Bereich von 6-9 mW, Seitenmodenunterdrückungen im Bereich von 30 dB. Das Design weist eine thermisch begrenzte 3 dB Modulationsbandbreite von etwa 11 GHz und eine Linienbreite im Bereich von 7 bis 8 MHz auf.

Mit dem Ziel einer Stabilisierung der Ausgangsleistung über den Abstimmbereich des Lasers wird ein separat kontaktiertes Verstärkungssegment monolithisch mit dem abstimmbaren Laser integriert. Durch geeignete Auswahl der Ströme in das Verstärkungssegment ist es möglich, die Ausgangsleistung des Lasers über den Abstimmbereich auf 9 mW zu stabilisieren.

Betrieb des 2D photonischen Kristalls in der Bandlücke: Wellenleiter

In einem zweiten Aspekt der Arbeit werden photonische Kristalle nicht nur zum longitudinalen Photoneneinschluß sondern zur vollständigen Kontrolle der Lichtpropagation in der Wellenleiterebene genutzt. Dies geschieht durch die Einführung von Defektreihen innerhalb des photonischen Kristalls, die in dieser Arbeit zur Bildung von Laserresonatoren und effizienten Wellenleiterknicken genutzt werden. Ein neuartiges weit abstimmbares Laserdesign wird vorgestellt, in dem gekoppelte Kavitäten durch photonische Kristalle definiert werden. Der Laser weist einen Abstimmbereich von 30 nm und Seitenmodenunterdrückungen von etwa 41 dB auf. Maximale Ausgangsleistungen liegen im Bereich von 3 mW. Je nach Breite der die Laserresonatoren bildenden photonischen Kristallwellenleiter weisen die Laser externe Quanteneffizienzen zwischen 25 mW/A und 48 mW/A und Schwellströme zwischen 13 mA und 19 mA auf. Das Design zeichnet sich ferner eine thermisch begrenzte Modulationsbandbreite von 17 GHz und eine Linienbreite von etwa 15 MHz aus. Das Abstimmverhalten ist durch Anti-Kreuzungspunkte gekennzeichnet, die sich durch die Kopplung der beiden Fundamentalmoden der Partialresonatoren an der durch den photonischen Kristall definierten Schnittstelle ausbilden. Ein Vergleich der theoretischen und der experimentell beobachteten Kopplungsstärke ermöglicht die Abschätzung der

Beugungsverluste im photonischen Kristall Koppelsegment.

Ferner wird die Propagation des von diesen Laserstrukturen emitterten Lichts durch zu Kombiniererstrukturen integrierten Wellenleiterdoppelknicken untersucht. Die Doppelknicke stellen Brüche in der Periodizität des photonischen Kristallwellenleiters dar, die zu Reflexionen im Bereich der Knicke und mögliche Kopplung an höhere Moden führen. Da die höheren Moden größere Verluste gegenüber der Fundamentalmode aufweisen, ist ein Verlustmechanismus für das in der Knickstruktur propagierende Licht geöffnet, der zu einer Dämpfung des optischen Signals führt. In diesem Zusammenhang werden verschiedene Kombiniererrtypen vorgeschlagen und miteinander verglichen. Es stellt sich heraus, daß die geringste Dämpfung von etwa 10 dB für Kopplerstrukturen beobachtet wird, die im Bereich der Knicke eine schlitzartige Struktur mit hohem Indexkontrast aufweisen.

Betrieb des 2D photonischen Kristalls am Rand der Bandlücke: Superprismastudien

Neben den offensichtlich außergewöhnlichen Eigenschaften der photonischen Kristalle, die auf der Existenz einer photonischen Bandlücke beruhen, in der die Propagation von Licht in der Wellenleiterebene verboten ist, ist die Untersuchung der Dispersionseigenschaften am Rand der photonischen Bandlücke zumindest ebenso interessant. Eine geringe Veränderung der Photonenenergie bzw. des Eingangswinkels des einfallenden Lichtstrahls kann in diesem Bereich zu einer drastischen Veränderung der Krümmung der Isofrequenzlinien führen und mithin zu einer Vielzahl von Effekten wie der Strahlkollimation, Strahlbündelung und einer signifikanten Veränderung der Propagationsrichtung des Lichts innerhalb der Struktur. Letzterer kann zu Winkeldispersionen führen, die um mehrere Größenordnungen über denen eines konventionellen Prismas liegen und wird daher häufig als 'Superprisma'-Effekt bezeichnet. Kapitel 6 gibt zunächst Einblick in das Verständnis der kollimierenden und refraktiven Eigenschaften von photonischen Kristallen am Rand der photonischen Bandlücke. Der Superprisma-Effekt wird anhand von triangulären und quadratischen Gitterstrukturen experimentell demonstriert, wobei eine Winkeldispersion im Bereich von etwa 0.5 °/nm beobachtet wird. Es wird untersucht, inwieweit eine Modenanpassung am Ein-

gang des photonischen Kristallblocks zu einer Verbesserung der Transmissions-
eigenschaften durch die Gesamtstruktur führen kann. Es stellt sich heraus, daß
Auflösung und Verluste der vorgestellten Superprismastruktur den Anforderun-
gen für Anwendungen im Bereich des Wavelength Division Multiplexing nicht
genügen. Konzepte für eine Optimierung des Designs werden diskutiert.

Chapter 2
Introduction

Over the past 40 years, electronics has enjoyed tremendous advancements in almost every aspect of information processing. As postulated by Moore's law, the data density on an electronic chip has approximately doubled every 18 months, so that today's computer processors already integrate 5 million transistors onto a chip with an area of about 3 cm^2. Although this trend is likely to continue for another decade, the past few years have shown that the rapid integration process will inevitably saturate as a consequence of the inherent physical limitations of electronics. The most important confining factors are limitations with respect to heat dissipation and increasing leakage currents which effectively prevent a further down-scaling. Not even the development of new gate-oxide materials will open sufficient room for the further miniaturization that is required in the not so distant future. First signatures of the saturation effect as a consequence of continued miniaturization are already becoming manifest: today's computers already require external cooling schemes in order to avoid a destructive overheating of the densely integrated electronic hardware.

On the other hand, the drastically increased demand for bandwidth that has resulted from the extraordinary growth in internet traffic thrives the demand for high bandwidth transmission not only on long-haul networks, but also on metropolitan and access networks. It is commonly anticipated that todays copper-based access networks do not have the capacity to support the predicted bandwidth demands.

The above arguments are forcing both network providers as well as the computer industry to investigate alternative solutions to overcome the already emerging bottlenecks. Any possible solution has to meet at least two key requirements: the constituent material system has to be compatible with other materials and devices on a single chip, and it has to be allow for the integration of many functions on the same chip in order to reduce costs of operation and production.

An interesting alternative is to operate not on electronic states but on a light scale. For communication networks, the large bandwidths, low signal attenuation and distortions, and low power requirements of optical fiber networks make them a promising solution to satisfy the demands of any future network. Compared to electronic data rates of only a few Gigabits per second, the bandwidth of a single-mode fiber of 50 Terabits per second is almost four orders of magnitude higher. First wavelength division multiplexing (WDM) based demonstrators have been realized at data rates > 10 Terabits per second.

Unfortunately, optical circuits have inherent physical limitations as well. One of the most challenging aspects of optical signal processing is the efficient confinement of light on an optical microchip which puts a question on the aspect of reducing the chip size as a key requirement of significant cost reduction[1]. It is this aspect that makes photonic crystals an emerging meta-material that is hoped to change all that.

Photonic crystals are artificially created meta-materials in which the index of refraction is modulated periodically on a length scale that is compatible to the wavelength of light. In analogy to the formation of electronic band structures in which the electron is experiencing the periodic modulation of the potential energy from the lattice structure, also the periodic modulation of the dielectric constant gives rise to the formation of energy bands for photons and in particular to the formation of a photonic bandgap (provided the lattice dimensions have been chosen appropriately). Within the photonic bandgap, no optical modes are allowed to exist so that the propagation into the crystal is prohibited. The anomalous dispersion properties can be appreciated when designing optoelectronic circuitry. The bandgap can be used to build very efficient reflectors and waveguides, ultrasmall waveguide bends, light sources, and filter structures, virtually any optoelectronic component we know today. Although enabling factors such as design tools for optical circuits equivalent to those presently existing for electronic circuits are not readily available yet, the transfer of signal processing from the electronic regimes to the optical regime is very appealing and has already resulted in the proposal and realization of numerous novel photonic devices.

---

[1]For example, the limited component integration in today's optical network nodes make these components too costly for a deployment in metropolitan and access networks.

For both optical microchips as optical processors and optical communication networks, active laser sources are required to allow the subsequent processing of information. Light sources with a variable emission wavelength obviously promise parallel data processing and are therefore an important component in the development of the new technology and therefore have attracted great research interest. Already in today's optical networks, wavelength tunable laser diodes can significantly simplify the maintenance of transmission systems by reducing the complexity of component stocks for network providers.

A common concept to realize tunable laser diodes is based on the Vernier effect which employs the contra-directional coupling of two or more mode combs that are defined in separately contacted segments. A common approach to realize tunable laser diodes is to define sampled gratings [Col1993, Col1999, Oug1996, Del1998a, Del1998b] or superstructure gratings [Toh1993a, Toh1993b, Toh1996, Gaug1997] with distributed Bragg reflectors that are placed adjacent to a gain region. Index modulation here is entirely due to changes of the carrier density resulting in a blue shift of the respective mode comb. As an alternative, lasers with gain-coupled distributed feedback [Kamp1999] defined through binary superimposed gratings lateral to an active gain section have been investigated avoiding an additional regrowth step that is necessary for the buried sampled or superstructure grating structures. In this case, the tuning mechanism is based on the heating of the active regions resulting in a red shift of the respective mode comb [Muel2001]. These developments are however fundamentally limited by the problem of light confinement in weakly guiding waveguide structures resulting in large component sizes and therefore contradicting the manufacturers' increasing demand for higher component density.

Therefore, a significant part of this work is devoted to exploring the possibility of integrating tunable laser diodes based 2D photonic crystals with other photonic crystal based devices. 2D PhC's have the advantage of being compatible with standard VLSI processing technologies. Light confinement in the vertical direction can be accomplished either through a strong index confinement as realized in membrane-type topologies or through the weak index-guiding of an planar waveguide structure. The latter topology is the preferred topology for active devices based on photonic crystals due to its inherently advantageous heat dissipation

compared to the first topology. Despite the more stringent demands on device fabrication due to the necessity of etching deep air cylinders through the complete planar waveguide structure to reduce out-of-plane scattering losses, this work presents two different widely tunable laser designs with PhC reflectors. A first design realizes a combination of ridge waveguides and photonic crystals. Lateral metal gratings provide gain-coupled distributed feedback to two independently contacted resonators that are mutually longitudinally confined by PhC reflectors. The PhC reflectors will introduce a new design freedom to tunable laser diodes through the flexible control of the intra-cavity coupling properties. A second design longitudinally couples two photonic crystal channel waveguides of slightly different lengths and therefore slightly different longitudinal mode spacings. In these devices, both the lateral as well as the longitudinal photon confinement is provided by the PhC waveguide boundary. The periodic modulation of the refractive index of the waveguide boundary can be used to stabilize laser operation. Both designs allow the monolithic integration with other devices such as optical amplifiers and modulators to build more complex photonic integrated circuits. The combined ridge waveguide / PhC reflector design is monolithically integrated with an amplifier section. By doing so, it will be shown that the output power can be stabilized over the laser's entire tuning range. Secondly, two tunable coupled photonic crystal channel waveguide designs are monolithically integrated with a Y-coupler structure to build a two-channel tunable laser diode.

The extraordinary dispersion properties of 2D PhC's do not only lead to the formation of photonic bandgaps that can be used to efficiently build reflectors and waveguides, they can lead to extraordinary beam steering and light deflection properties in the low group velocity regime near the photonic bandgap. In a separate chapter, this work therefore presents the significant change in propagation direction of light of different wavelengths and incident angles. This effect which is also commonly referred to as the superprism effect relies on the fact that the dispersion surfaces of PhC's can differ very significantly from the cone-shaped dispersion surfaces of standard bulk material. Consequently, the isofrequency contours can differ dramatically depending on the wavelength of the incident light whereas they will always remain circular for bulk material.

Chapter 3

Theoretical Background

3.1 Semiconductor Laser Fundamentals

In this chapter, after a brief review of how a laser operates, a few details are discussed that will be relevant for some of the phenomena that will be discussed in chapters 4 and 4, most notably the change of the refractive index due to carrier and thermal effects and its effect on the emission wavelength of the laser.

Semiconductor lasers require gain, feedback, and external excitation for successful operation. The region that provides optical gain is referred to as the active region. The gain medium is surrounded by cladding layers of a larger bandgap and is placed between two mirrors that provide the feedback required for lasing operation. The external excitation can be either through external optical radiation or through carrier injection in the transverse direction of the laser.

3.1.1 III-V Compound Semiconductors

The emission wavelength of a semiconductor laser can be selected through the selection of its material system and therefore its band gap energy E_g. Figure 3.1(a) shows the size of the bandgap as a function of the lattice constant for various material systems. Selected respective emission wavelengths are indicated on the right hand side. It should be noted that the quaternary lattice-matched material system $In_xGa_{1-x}As_yP_{1-y}$ has two degrees of freedom. The free parameters x and y are determined through the lattice constant of InP and the desired photoluminescence emission wavelength.

To create an efficient laser device, heterojunctions are used in which the active region is surrounded by larger bandgap p- and n-doped cladding layers[1]. As the

---

[1]High doping levels ensure a high concentration of electron-hole pairs that can contribute to stimulated recombination. In III-V compound semiconductors, p-doping is accomplished by
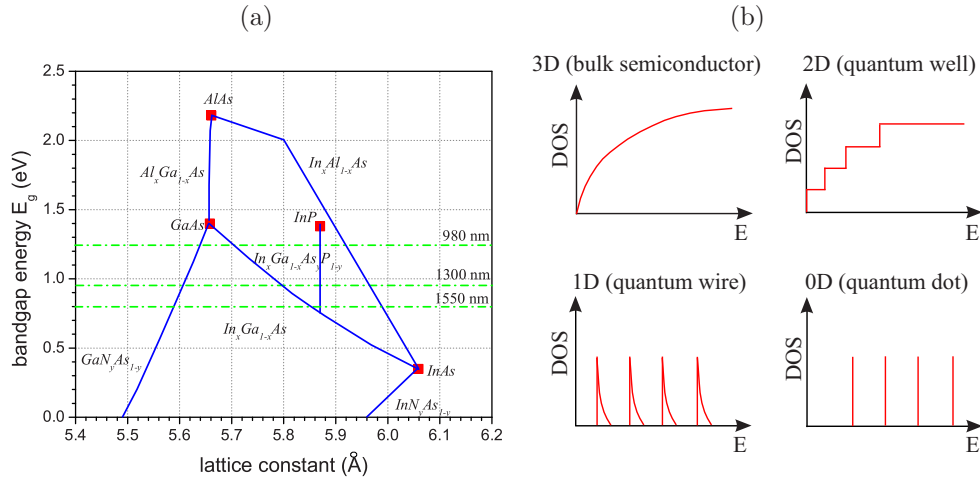
Figure 3.1: (a) Bandgap energy versus lattice constant (b) Density of state (DOS) as a function of energy for different active material dimensions.

quality of the interface between the constituent materials of different bandgaps affects the laser characteristics, the choice of heterojunction materials is limited: the lattice constants of the materials cannot differ by more than 0.1% to avoid lattice defects.

The injected carriers are trapped in the quantum film either through a separate confinement (SCH) or graded index separate confinement heterostructure (GRINSCH). In both cases, the material surrounding the active layer has a higher band energy so that electrons, once injected into the system move towards the active structure where they possess the lowest energy. Once trapped in the active region, they recombine under emission of a photon whose energy equals the energy of the bandgap. A disadvantage of the SCH structure against the GRINSCH structure is that it has a slightly reduced carrier injection efficiency due to the band gap discontinuities prevalent in the doped double heterostructures and possible reflections of carriers at the potential barriers.

For III-V based semiconductors, a larger bandgap coincides with a smaller refractive index so that the cladding has a larger bandgap as well as a smaller refractive index than the active region. As a consequence, heterostructures provide

---

replacing triple (quintuple) valency elements by double (quadruple) valency dopants, whereas n-doping is achieved by replacing triple (quintuple) elements by quadruple (sextuple) valency dopants.

simultaneous carrier and photon confinement in the active region. The photons are confined to the active layer by total internal reflection at the active region/ cladding interfaces. Lateral photon confinement can be achieved for example by index or gain guiding. Two different concepts of lateral photon confinement will be discussed in chapters 4.2 and 5.2.

The active region is typically chosen to be of low-dimensional order, e.g. two-dimensional in quantum film lasers, one-dimensional in quantum wires or zero-dimensional in quantum dot lasers. In these lower dimensional systems, a quantization of the energy levels into discrete values occurs which has a number of advantageous implications. It results in an increased carrier density at the gap due to a higher density of states. The simultaneous reduction of the active volume leads to reduced threshold levels. Figure 3.1(b) schematically illustrates the change in density of states (DOS) as the dimensionality is decreased from a three-dimensional bulk semiconductor to a zero-dimensional quantum dot. The small layer thickness of low-dimensional active materials furthermore allows the inclusion of non-lattice-matched materials in the active layer so that an increased range of wavelengths can be covered with one material system. The resulting strain from the non-lattice matched material does not relax due to the small layer thickness.

Throughout this work, a 1.55 μm InGaAsP quantum well structure with four or six compressively strained (1%) wells separated by three or five quaternary lattice matched barriers is used. Inducing compressive strain on the quantum film results in an increase in the bandgap as well as the destruction of the heavy hole (HH) - light hole (LH) degeneracy of the electronic band structure. Compressively strained quantum films typically facilitate larger material gain as well as reduced transparency carrier densities compared to non-strained structures. The strain furthermore introduces significantly different material gains for TE- and TM-polarization. The epitaxial details of the various structures used in the experiments are given in Appendix D.
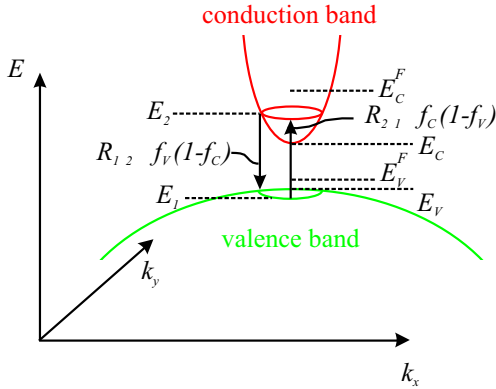
Figure 3.2: Schematic illustration of energy levels in a semiconductor laser. Quasi-Fermi levels considering non-equilibrium conditions.

3.1.2   Conditions for laser operation

Fundamentally, the semiconductor laser operation is based on the stimulated emission of photons due to a recombination of injected carriers at the pn-junction. In order to realize light amplification based on stimulated emission, one has to ensure that the number of stimulated emission events is larger than its reverse process, the absorption. Considering a two-level system as illustrated in Figure 3.2, stimulated recombination occurs between electrons located below the quasi Fermi level in the conduction band and holes located above the quasi Fermi level in the valence band. The electrons and holes are distributed according to Fermi-Dirac distributions in their respective bands

$$f_C = \frac{1}{1 + e^{(E_2 - E_C^F)/k_B T}} \tag{3.1}$$

$$f_V = \frac{1}{1 + e^{(E_V^F - E_1)/k_B T}} \tag{3.2}$$

where f_C and f_V describe the probability of finding a carrier in the conduction and valence band, respectively, and E_C^F and E_V^F are the quasi Fermi energy levels of the electrons and holes, respectively. The ratio of the occupancy densities N_i is described by the Maxwell-Boltzmann distribution

$$\frac{N_2}{N_1} = \frac{g_2}{g_1} \exp\left(-\frac{E_2 - E_1}{k_B T}\right) \tag{3.3}$$

where g_i describes the degree of degeneracy in each level[2]. Inversion of occupancy $N_2/g_2 > N_1/g_1$ is established when the photon density N_p increases in time which is satisfied if the rate of stimulated emission events is larger than the number of absorption events:

$$\frac{dN_p}{dt} = R'_{sp} + (R_{21} - R_{12}) > 0 \qquad .$$ (3.4)

The transition rates R_{21}, R_{12}, and R'_{sp} are schematically illustrated in Figure 3.3. R_{sp} denotes the total rate of spontaneous emission events in which an electron in the conduction band radiatively recombines with a hole in the valence band. $R'_{sp} = \beta_{sp} R_{sp}$ counts the spontaneous emission events into the relevant mode only[3]. R_{12} and R_{21} describe the rate of stimulated absorption and recombination events, respectively. During a stimulated absorption event, an incoming photon lifts an electron from the valence band to the conduction band, thus creating an electron-hole pair. During stimulated recombination event, an incoming photon triggers the radiative recombination of an electron-hole pair resulting in the creation of a second photon of the same energy[4]. R_{nr} denotes the non-radiative transition rate in which the recombination of an electron-hole pair is accompanied by the thermal excitation of an electron in the conduction band. The recombination can be at a lower energy defect state. These transition rates are related to the occupancy densities N_1 and N_2 by the Einstein coefficients A_{21} and B_{21} for spontaneous and stimulated emission. The occupancy of level 2 is determined by the product of the probability f_C of finding an electron in the conduction band and the probability $1 - f_V$ of non-occupancy of the valence band with electrons, i.e. the probability of occupancy of a hole in the valence band. The same applies

---

[2]As one can see, in the thermodynamic equilibrium it is impossible to achieve a population inversion, N_1 will always be larger than or equal to N_2. In order to achieve population inversion one has to include an additional energy source in order to elevate the occupancy of level 2, the process of which is called pumping and will be discussed later in this section. It can be described in the Boltzmann distribution through a negative temperature.

[3]β_{sp} denotes the so called spontaneous emission factor.

[4]This characterizes a major difference between bosons and fermions. Bosons such as photons have a tendency to be created of the same state whereas the creation of fermions such as electrons is governed by the Pauli exclusion principle.
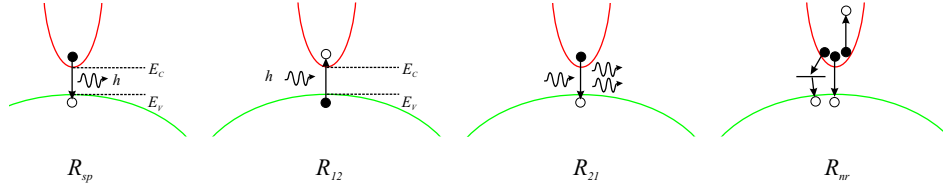
Figure 3.3: Transitions in a semiconductor laser

for level 1 so that for $g_1 = g_2 = 1$ the inversion of occupancy can be rewritten as

$$f_C(1 - f_V) - f_V(1 - f_C) > 0 \qquad (3.5)$$

which is satisfied if

$$E_C^F - E_V^F > E_2 - E_1 = h\nu \qquad . \qquad (3.6)$$

The inversion of occupancy can be achieved by pumping the system. In the case of semiconductor lasers either through current injection or external electromagnetic radiation referred to as optical pumping, in the case of solid state lasers or dye lasers through optical pumping, through electron impact in gas lasers, or through chemical reactions in chemical lasers. For electrically pumped lasers, one can define a pump rate R

$$R = \frac{\eta_i I}{qV} \qquad (3.7)$$

which enters the rate equations. η_i denotes the injection efficiency, V is the volume of the active region, and q is the electron charge. Below threshold, the pumping process increases the number of free carriers in the active region of the diode. In order to obtain the carrier density as a function of the pump rate which in turn is proportional to the segment bias, one has to account for various carrier recombination effects that have been extensively discussed in the literature:

$$R = AN(I) + BN(I)^2 + CN(I)^3 \qquad (3.8)$$

where A, B, and C account for non-radiative, radiative, and Auger recombinations, respectively. With the radiative term dominating, the carrier density increases approximately with the square root of the segment bias until it is clamped at laser threshold.
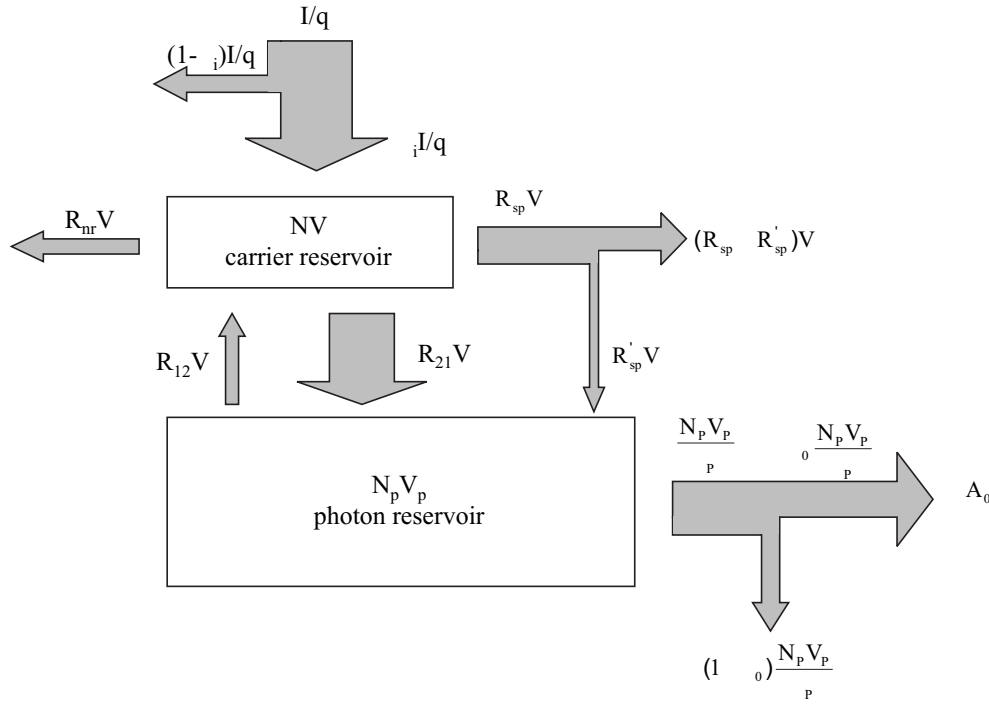
Figure 3.4: Schematic illustration of rates (number of particles per unit time) used in rate equation analysis [Col1995]

3.1.3   Rate equations

In order to obtain a quantitative understanding of the flow/propagation of carriers and photons in a laser diode during operation, it is helpful to look at the rates of carriers N entering and exiting the carrier reservoir of the active region on one hand, and photons N_p entering and leaving a photon reservoir in which the optical modes reside. Figure 3.4 provides an overview of the changes in the reservoirs of a typical semiconductor laser diode [Col1995]. The rate of change in carriers and photons can be written as a balance of rates entering and leaving the respective reservoirs as follows:

$$V\frac{dN}{dt} = \frac{\eta_i I}{q} - (R_{sp} + R_{nr})V - (R_{21} - R_{12})V \tag{3.9}$$

$$V_p\frac{dN_p}{dt} = (R_{21} - R_{12})V - \frac{N_p}{\tau_p}V_p + R'_{sp}V \tag{3.10}$$

Here, V again denotes the volume of the active region and V_p the volume in which the optical mode resides. The various transition rates have been introduced in Fig. 3.3. Non-radiative recombinations $R_{nr}V$ result in heating of the gain region. Those carriers that do not reach the carrier reservoir recombine elsewhere in the

device to generate either heat or light. Photons that do not deplete the photon reservoir through stimulated absorption events leave the cavity at a rate $N_p V_p / \tau_p$ either through the desired output channel to be collected as useful output power A_0 or through any other undesired output channel such as free carrier absorption in the active region, absorption outside the active region, or scattering at rough surfaces to generate either heat or light.

Defining an optical confinement factor $\Gamma = V/V_p$ and rewriting $(R_{21} - R_{12}) = ugN_p$ where g and u describe the gain per unit length and group velocity, respectively, one obtains the density rate equations

$$\frac{dN}{dt} = \frac{\eta_i I}{qV} - (R_{sp} + R_{nr}) - ugN_p \tag{3.11}$$

$$\frac{dN_p}{dt} = \left[\Gamma ug - \frac{1}{\tau_p} \right] N_p + \Gamma R'_{sp} \tag{3.12}$$

The differentials of the density rate equations are

$$d\left[\frac{dN}{dt}\right] = \frac{\eta_i}{qV} dI - \underbrace{\left(\frac{dR_{sp}}{dN} + \frac{dR_{nr}}{dN}\right)}_{\frac{1}{\tau_{\Delta N}}} dN - ugdN_p - N_p udg \tag{3.13}$$

$$d\left[\frac{dN_p}{dt}\right] = \left[\Gamma ug - \frac{1}{\tau_p}\right] dN_p + N_p \Gamma udg + \Gamma \underbrace{\frac{dR'_{sp}}{dN}}_{\frac{1}{\tau'_{\Delta N}}} dN \tag{3.14}$$

Assuming that the gain g generally depends on the carrier density N and the photon density N_p, we can express the gain as

$$dg = \frac{\partial g}{\partial N} dN + \frac{\partial g}{\partial N_p} dN_p \tag{3.15}$$

so that we can rewrite the differential rate equations as

$$\frac{d}{dt}(dN) = \frac{\eta_i}{qV} dI - \underbrace{\left[\frac{1}{\tau_{\Delta N}} + u\frac{\partial g}{\partial N} N_p\right]}_{\Xi_{NN}} dN - \underbrace{\left[\frac{1}{\Gamma \tau_p} - \frac{R'_{sp}}{N_p} - u\frac{\partial g}{\partial N_p} N_p\right]}_{\Xi_{NP}} dN_p \tag{3.16}$$

$$\frac{d}{dt}(dN_p) = \underbrace{\left[\frac{\Gamma}{\tau'_{\Delta N}} + \Gamma u\frac{\partial g}{\partial N} N_p\right]}_{\Xi_{PN}} dN + \underbrace{\left[\frac{\Gamma R'_{sp}}{N_p} + \Gamma u\frac{\partial g}{\partial N_p} N_p\right]}_{\Xi_{PP}} dN_p \tag{3.17}$$

or in matrix notation

$$\frac{d}{dt}\begin{pmatrix} dN \\ dN_p \end{pmatrix} = \begin{pmatrix} -\Xi_{NN} & -\Xi_{NP} \\ \Xi_{PN} & -\Xi_{PP} \end{pmatrix} \begin{pmatrix} dN \\ dN_p \end{pmatrix} + \frac{\eta_i dI}{qV} \begin{pmatrix} 1 \\ 0 \end{pmatrix} \tag{3.18}$$

The current dI serves as a driving force of the system.

3.1.4 Quantum noise

First, we want to evaluate the small signal response $dN(t)$ and $dN_p(t)$ of our laser structure on a sinusoidal modulation of the input current. Assuming

$$
\begin{aligned}
dI(t) &= I_0 \exp j\omega t & (3.19) \\
dN(t) &= N_0 \exp j\omega t & (3.20) \\
dN_p(t) &= N_{p0} \exp j\omega t & (3.21)
\end{aligned}
$$

and considering that $d/dt \to j\omega$ due to the separation of time dependence, we can write

$$
\begin{pmatrix} \Xi_{NN} + j\omega & \Xi_{NP} \\ -\Xi_{PN} & \Xi_{PP} + j\omega \end{pmatrix} \begin{pmatrix} N_0 \\ N_{p0} \end{pmatrix} = \frac{\eta_i I_0}{qV} \begin{pmatrix} 1 \\ 0 \end{pmatrix} \tag{3.22}
$$

Solving for the small signal responses of the carrier and photon densities and applying Cramer's rule yields

$$
\begin{aligned}
N_0 &= \frac{\eta_i I_0}{qV} \det{}^{-1} \begin{pmatrix} \Xi_{NN} + j\omega & \Xi_{NP} \\ -\Xi_{PN} & \Xi_{PP} + j\omega \end{pmatrix} \det \begin{pmatrix} 1 & \Xi_{NP} \\ 0 & \Xi_{PP} + j\omega \end{pmatrix} \\[2mm]
&= \frac{\eta_i I_0}{qV} \frac{\Xi_{PP} + j\omega}{(\Xi_{NP}\Xi_{PN} + \Xi_{NN}\Xi_{PP})} \frac{\overbrace{(\Xi_{NP}\Xi_{PN} + \Xi_{NN}\Xi_{PP})}^{\equiv \omega_R^2}}{(\Xi_{NP}\Xi_{PN} + \Xi_{NN}\Xi_{PP}) - \omega^2 + j\omega \underbrace{(\Xi_{NN} + \Xi_{PP})}_{\equiv \gamma}} \\[2mm]
&= \frac{\eta_i I_0}{qV} \frac{\Xi_{PP} + j\omega}{\omega_R^2} \frac{\omega_R^2}{\omega_R^2 - \omega^2 + j\omega\gamma} \equiv \frac{\eta_i I_0}{qV} \frac{\Xi_{PP} + j\omega}{\omega_R^2} H(\omega) & (3.23) \\[2mm]
N_{p0} &= \frac{\eta_i I_0}{qV} \det{}^{-1} \begin{pmatrix} \Xi_{NN} + j\omega & \Xi_{NP} \\ -\Xi_{PN} & \Xi_{PP} + j\omega \end{pmatrix} \det \begin{pmatrix} \Xi_{NN} + j\omega & 1 \\ -\Xi_{PN} & 0 \end{pmatrix} \\[2mm]
&= \frac{\eta_i I_0}{qV} \frac{\Xi_{PN}}{\omega_R^2} H(\omega) & (3.24)
\end{aligned}
$$

The term

$$
H(\omega) = \frac{\omega_R^2}{\omega_R^2 - \omega^2 + j\omega\gamma} \tag{3.25}
$$

is referred to as the modulation transfer function, ω_R is referred to as the relaxation resonance frequency, and γ is referred to as the damping factor.

If the current from equation (3.18) is replaced by general noise terms $F_N(t)$ and $F_P(t)$ for the carriers and photons, respectively, equation (3.18) reads as

$$\frac{d}{dt} \begin{pmatrix} dN \\ dN_p \end{pmatrix} = \begin{pmatrix} -\Xi_{NN} & -\Xi_{NP} \\ \Xi_{PN} & -\Xi_{PP} \end{pmatrix} \begin{pmatrix} dN \\ dN_p \end{pmatrix} + \begin{pmatrix} F_N(t) \\ F_P(t) \end{pmatrix} \tag{3.26}$$

Moving to frequency space by replacing the time-dependent variables by their Fourier transforms, we obtain (see above)

$$\begin{pmatrix} \Xi_{NN} + j\omega & \Xi_{NP} \\ -\Xi_{PN} & \Xi_{PP} + j\omega \end{pmatrix} \begin{pmatrix} N_0(\omega) \\ N_{p0}(\omega) \end{pmatrix} = \begin{pmatrix} F_N(\omega) \\ F_P(\omega) \end{pmatrix} \tag{3.27}$$

Similarly to the evaluation of the small-signal response, we obtain

$$N_0(\omega) = \frac{H(\omega)}{\omega_R^2} \det \begin{pmatrix} F_N(\omega) & \Xi_{NP} \\ F_P(\omega) & \Xi_{PP} + j\omega \end{pmatrix} \tag{3.28}$$

$$N_{p0}(\omega) = \frac{H(\omega)}{\omega_R^2} \det \begin{pmatrix} \Xi_{NN} + j\omega & F_N(\omega) \\ -\Xi_{PN} & F_P(\omega) \end{pmatrix} \tag{3.29}$$

The carrier and photon spectral densities are then defined as

$$
\begin{aligned}
S_N(\omega) &= \frac{1}{2\pi} \int \langle N_0(\omega)N_0(\omega')^*\rangle d\omega' = \frac{|H(\omega)|^2}{2\pi\omega_R^4} \left[\Xi_{NP}^2 \int \langle F_P(\omega)F_P(\omega')^*\rangle d\omega' \right. \\
&\quad -2\Xi_{PP}\Xi_{NP} \int \langle F_P(\omega)F_N(\omega')^*\rangle d\omega' \\
&\quad \left. +(\Xi_{PP}^2 + \omega^2) \int \langle F_N(\omega)F_N(\omega')^*\rangle d\omega' \right] \\
&= \frac{|H(\omega)|^2}{\omega_R^4} \left[\Xi_{NP}^2\langle F_P F_P\rangle - 2\Xi_{PP}\Xi_{NP}\langle F_P F_N\rangle \right. \\
&\quad \left. +(\Xi_{PP}^2 + \omega^2)\langle F_N F_N\rangle \right] \\
S_{N_P}(\omega) &= \frac{1}{2\pi} \int \langle N_{P0}(\omega)N_{P0}(\omega')^*\rangle d\omega' \\
&= \frac{|H(\omega)|^2}{\omega_R^4} \left[(\Xi_{NN}^2 + \omega^2)\langle F_P F_P\rangle - 2\Xi_{NN}\Xi_{PN}\langle F_P F_N\rangle \right. \\
&\quad \left. +\Xi_{PN}^2\langle F_N F_N\rangle \right]
\end{aligned}
$$

$$\tag{3.30}$$

$$\tag{3.31}$$

The $\langle F_i F_j\rangle$ are the Langevin quantum noise sources that can be interpreted as noise correlation strengths.

Similarly, one obtains for the noise spectrum of the output power fluctuations $\Delta A = (\eta_0 h\nu/\tau_p)N_{p0}(t) + F_0(t)$:

$$S_{\Delta A}(\omega) = h\nu A_0 \left[\frac{a_1 + a_2\omega^2}{\omega_R^4}|H(\omega)|^2 + 1 \right] \tag{3.32}$$

so that we obtain the following expression for the relative intensity noise (RIN)

$$\frac{RIN}{\Delta f} = \frac{2S_{\Delta A}(\omega)}{A_0^2} = \frac{2h\nu}{A_0} \left[\frac{a_1 + a_2\omega^2}{\omega_R^4}|H(\omega)|^2 + 1 \right] \tag{3.33}$$

As a result of these quantum noise sources, Fabry-Perot lasers typically exhibit rather large linewidths in the range if a few ten MHz. Many attempts have been made to reduce the quantum noise in semiconductor lasers. With respect to phase or frequency noise, almost all concepts build on the coupling of the primary laser cavity to a second cavity. This second cavity can either be a normal Fabry-Perot resonator or a confocal Fabry-Perot (CFP) resonator. The devices we will investigate in chapters 4 and 5 will rely on the coupling of one cavity to a second cavity. Since the linewidth depends on the pump level, the minimal linewidths one can achieve with this mechanism are in the range of a few MHz. Attempts for a simultaneous reduction of amplitude and phase noise by means of a dispersive feedback coupling mechanism [Mah1998, Shevy1999] have resulted in significant reductions, fundamentally limited only by Heisenberg's uncertainty principle which can be expressed as

$$S_N(\omega) \cdot S_{N_p}(\omega) \geq \frac{1}{4r_0^2} \tag{3.34}$$

where r_0^2 is the number of photons per second.

3.2 Photonic band structures: Photonic Crystals

Photonic crystals can be described as the periodic modulation of the dielectric material in one, two, or three dimensions. Just as the band structure of a metal is described by a periodic modulation of the electric potential in a perfect lattice structure on a scale of a few Angstroms, the band structure for photons is caused

by the artificial modulation of the dielectric function on a wavelength scale of light. The band diagram features frequency windows called photonic bandgaps in which no eigenfunction can satisfy Maxwell's equations and therefore frequency bands in which no optical modes are allowed to exist.

3.2.1 Eigenvalue Problem

The propagation of light as an electromagnetic wave in a dielectric material can be described by Maxwell's equations

$$\vec{\nabla}\vec{D} = \rho \tag{3.35a}$$

$$\vec{\nabla}\vec{B} = 0 \tag{3.35b}$$

$$\vec{\nabla} \times \vec{E} + \frac{\partial}{\partial t}\vec{B} = 0 \tag{3.35c}$$

$$\vec{\nabla} \times \vec{H} - \frac{\partial}{\partial t}\vec{D} = \vec{j} \tag{3.35d}$$

where dielectric displacement $\vec{D}$ and the magnetic field $\vec{H}$ are related to the observables of the electric field $\vec{E}$ and the magnetic density $\vec{B}$ by

$$\vec{B} = \mu_0(\vec{H} + \vec{M}) = \mu_0(\vec{H} + \hat{\chi}_m\vec{H}) = \mu_0\hat{\mu}_r\vec{H} \doteq \mu_0\vec{H} \tag{3.36a}$$

$$\vec{D} = \epsilon_0\vec{E} + \vec{P} = \epsilon_0\left\{\vec{E} + \hat{\chi}_e^{(1)}\cdot\vec{E} + \hat{\chi}_e^{(2)}\cdot\vec{E}\vec{E} + \hat{\chi}_e^{(3)}\cdot\vec{E}\vec{E}\vec{E} + \ldots\right\}$$

$$= \epsilon_0\left\{1 + \hat{\chi}_e^{(1)}\right\}\cdot\vec{E} + \vec{P}^{NL} = \epsilon_0\hat{\epsilon}_r\cdot\vec{E} + \vec{P}^{NL} \doteq \epsilon_0\epsilon_r\vec{E} \tag{3.36b}$$

where $\chi_e^{(n)}$ is the nth-order electric susceptibility that expresses the material-mediated interaction between n fields[5], $\hat{\chi}_m$ and μ_r are the magnetic susceptibility and permeability, respectively. Considering nonlinear effects, the dielectric constant ϵ is a function of space and the electric field amplitude $\hat{\epsilon} = \hat{\epsilon}\left(\vec{r}, \vec{E}\right)$. All electro-optic effects result from the modification of the material's refractive index in response to the presence of a light signal which is of great interest as it will allow for a truly all-optical signal processing where one can influence the

---

[5]The second-order susceptibility is the source of the second order nonlinearities, such as the second harmonic generation (SHG) and the linear electro-optic effect, the third order susceptibility is the source of third order effects such as third harmonic generation (THG), the quadratic electro-optic effect (also referred to as Kerr effect), and electro-chromism (shift of a medium's absorbance spectrum in the presence of an electric field).

propagation light with light itself: it opens the possibility of an optical rather than electrical mediated change of the refractive index which would facilitate drastically increased switching speeds and hence would be a milestone for the development of an all-optical switching of circuitry. Since non-linear effects are generally weak, they require either very large device dimensions or strong field confinements (to achieve very large field amplitudes) to become noticeable. The use of photonic crystals can enhance the nonlinear effects due to the strong field confinements that can be realized as will be seen later [Sol2004, Min2004]. The present work is limited to an investigation of effects where the optical response remains linear. Consequently, for the materials investigated in this work, $\chi^{(n)}$ vanishes for $n > 1$. Furthermore, the materials are assumed to be non-magnetic and isotropic so that the relative material constants become scalar and the magnetic material constant becomes unity.

Looking only at the optical properties of a (passive) photonic crystal, there are furthermore no free carriers ($\vec{\rho} = 0$) and no currents ($\vec{j} = 0$) so that Maxwell's equations simplify to

$$\vec{\nabla}(\epsilon(\vec{r})\vec{E}(\vec{r},t)) = 0 \tag{3.37a}$$

$$\vec{\nabla}H(\vec{r},t) = 0 \tag{3.37b}$$

$$\vec{\nabla} \times \vec{E}(\vec{r},t) + \mu_0 \frac{\partial}{\partial t}\vec{H}(\vec{r},t) = 0 \tag{3.37c}$$

$$\vec{\nabla} \times \vec{H}(\vec{r},t) - \epsilon_0\epsilon(\vec{r})\frac{\partial}{\partial t}\vec{E}(\vec{r},t) = 0 \tag{3.37d}$$

By rotation of (3.37c) and insertion of (3.37d) one can separate the electric and magnetic field and express them in terms of two second order differential equations:

$$\frac{1}{\epsilon(\vec{r})}\vec{\nabla} \times (\vec{\nabla} \times \vec{E}(\vec{r},t)) \equiv \hat{\Theta}_E\vec{E}(\vec{r},t) = -\frac{1}{c^2}\frac{\partial^2}{\partial t^2}\vec{E}(\vec{r},t) \tag{3.38}$$

$$\vec{\nabla} \times \left(\frac{1}{\epsilon(\vec{r})} \cdot \vec{\nabla} \times \vec{H}(\vec{r},t)\right) \equiv \hat{\Theta}_H\vec{H}(\vec{r},t) = -\frac{1}{c^2}\frac{\partial^2}{\partial t^2}\vec{H}(\vec{r},t) \tag{3.39}$$

where $c = (\epsilon_0\mu_0)^{-1/2}$ is the speed of light in vacuum. The solutions of 3.39 will be of the form

$$\vec{E}(\vec{r},t) = \vec{E}(\vec{r})e^{-i\omega t} \tag{3.40}$$

$$\vec{H}(\vec{r},t) = \vec{H}(\vec{r})e^{-i\omega t} \tag{3.41}$$

where ω denotes the eigenfrequency and $\vec{E}(\vec{r})$ and $\vec{H}(\vec{r})$ denote the eigenfunctions of the two wave equations. Plugging 3.41 into 3.39 we can rewrite the eigenvalue problem as

$$\hat{\Theta}_E \vec{E}(\vec{r}) = \frac{\omega^2}{c^2} \vec{E}(\vec{r}) \tag{3.42}$$

$$\hat{\Theta}_H \vec{H}(\vec{r}) = \frac{\omega^2}{c^2} \vec{H}(\vec{r}) \tag{3.43}$$

These equations represent an eigenvalue problem of the operators $\hat{\Theta}_E$ and $\hat{\Theta}_H$ whose eigenfunctions $\vec{E}(\vec{r}, t)$ $\vec{H}(\vec{r}, t)$ describe the field distributions of the electric and magnetic fields, respectively.

Equation (3.39) is also referred to as the Master equation due to its fundamental importance, it mathematically expresses the central problem of this work: the propagation of electromagnetic waves in photonic crystals.

3.2.2   Symmetries and Invariances

In this chapter, the symmetry operations of those topologies are discussed that are investigated in this work: the 2D triangular and square topologies. The invariances resulting from the symmetries have very important implications as will be seen. The translational invariance gives rise to the application of the Bloch theorem, the rotational invariance allows the limitation to a discussion of the irreducible Brillouin zone, thus saving significant computational effort, and in some cases even to a reduction of the main symmetry axes, the invariance under re-scaling which is actually a direct consequence from Maxwell's equations allows the convenient verification of thought experiments on a millimeter scale.

Symmetries of selected topologies

As a rule of thumb any symmetry leads to a conservation rule.

In this chapter we discuss the invariances for the cases of triangular and square arrays of circles extending infinitely along the z-axis. The symmetries will have implications that will assist in solving the Master equation in the following chapter.

The symmetry operations of the Γ-point of the 2D triangular point lattice form

the point group

$$
\begin{aligned}
C_{6_\nu} &= \{E, C_6, C_6^{-1}, C_3, C_3^{-1}, C_2, \sigma_x, \sigma_x', \sigma_x'', \sigma_y, \sigma_y', \sigma_y''\} \\
&= \{E, 2C_6, 2C_3, C_2, 3\sigma_x, 3\sigma_y\} \tag{3.44}
\end{aligned}
$$

Similarly, the symmetry operations of the Γ-point of the 2D square point lattice form the point group

$$
\begin{aligned}
C_{4_\nu} &= \{E, C_4, C_4^{-1}, C_2, \sigma_x, \sigma_y, \sigma_d', \sigma_d''\} \\
&= \{E, 2C_4, C_2, 2\sigma_\nu, 2\sigma_d\} \tag{3.45}
\end{aligned}
$$

Discrete Translational Invariance and Bloch Theorem

The introduction of a periodicity in the dielectric function in the form of a triangular or square shaped array of air cylinders in a dielectric can also be expressed in terms of a translational operator $\hat{T}$:

$$
\hat{T}\,\epsilon(\vec{r}) \equiv \epsilon(\vec{r} + \vec{R}) = \epsilon(\vec{r}) \tag{3.46}
$$

$$
\vec{R} = n_i \vec{a}_i \qquad n_i \in \mathbb{Z}, \text{ and } i \in \mathbb{N} \tag{3.47}
$$

The simplest form of a photonic crystal therefore is the 1D photonic crystal, a periodic modulation of the dielectric function in the propagation direction of light[6]. Constructive interference between modes and therefore a selection of longitudinal modes is achieved when the Bragg condition $\lambda/n = \gamma\Lambda$ is satisfied where γ denotes the grating order.

Assuming that all electromagnetic fields can be expanded by a Fourier series, or in other words by plane waves of the form $e^{i\vec{k}\vec{r}}$, we can write down an eigenvalue equation for the translation operator $\hat{T}$ as follows:

$$
\hat{T}\vec{H}(\vec{r}) = \frac{1}{2\pi}\int_{-\infty}^{\infty}\vec{h}(\vec{k})e^{i\vec{k}(\vec{r}+\vec{R})}d\vec{k} = e^{i\vec{k}\vec{R}}\frac{1}{2\pi}\int_{-\infty}^{\infty}\vec{h}(\vec{k})e^{i\vec{k}\vec{r}}d\vec{k} = e^{i\vec{k}\vec{R}}\vec{H}(\vec{r}) \tag{3.48}
$$

so the field $\vec{H}(\vec{r})$ being an eigenfunction of the operator $\hat{\Theta}_H$ is kept invariant under discrete translations $\hat{T}$:

$$
\hat{\Theta}_H = \hat{T}^{-1}\hat{\Theta}_H\hat{T} \tag{3.49}
$$

---

[6]Some authors introduce the terminology of photonic crystals only for periodicities in more than one dimension.
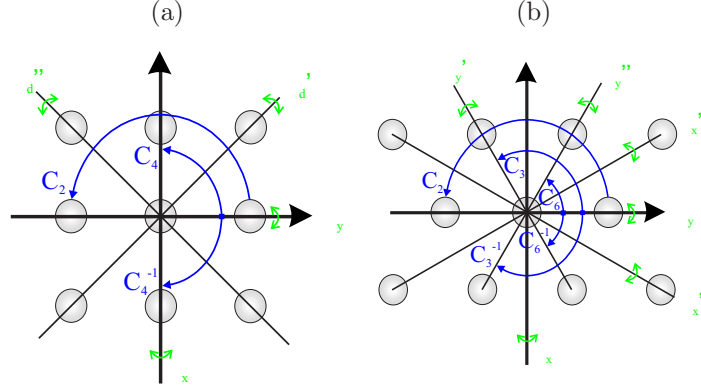
Figure 3.5: Symmetry operations of (a) Square lattice (b) Triangular lattice.

so that $\hat{T} = e^{i\vec{k}\vec{R}}$ and $\hat{\Theta}_H$ commute:

$$[\hat{T}, \hat{\mathcal{H}}] = 0 \quad . \tag{3.50}$$

Consequently, the eigenfunctions are the mutual eigenmodes of both $\hat{T}$ and $\hat{\Theta}_H$. According to Bloch's theorem, $\vec{H}(\vec{r})$ has to satisfy the condition $\vec{H}(\vec{r} + \vec{R}) = \exp{(i\vec{k}\vec{R})}\vec{H}(\vec{r})$ which is satisfied by the so called Bloch modes

$$\vec{H}_{\vec{k}n}(\vec{r}) = \vec{u}_{\vec{k}n}(\vec{r})e^{i\vec{k}\vec{r}} \quad \text{with} \quad \vec{u}_{\vec{k}n}(\vec{r} + \vec{R}) = \vec{u}_{\vec{k}n}(\vec{r}) \tag{3.51}$$

where n is called the band index and denotes different eigenmodes for a given wave vector $\vec{k}$. The Bloch modes of ideal 2D and 3D PhC's, being the eigenfunctions of a Hermetian operator form a complete and orthonormal set of functions. The eigenvalues of $\hat{\Theta}_H$ exhibit the same periodicity as the reciprocal lattice, i.e. $\omega_n(\vec{k}) = \omega_n(\vec{k} + \vec{G})$ so that one can reduce the computation of the eigenvalue problem to the first Brillouin zone.

For the case of ideal 2D PhC's, the vertical translation group is continuous, therefore eliminating any z-dependencies. Maxwell's vectorial equations (3.37c) and (3.37d) can be decoupled into two independent sets of scalar equations referred to as the transverse electric (TE) and transverse magnetic (TM) group:

1. The Transverse Electric (TE) Group

$$\frac{\partial}{\partial t}E_x = \frac{1}{\epsilon}\left[\frac{\partial}{\partial y}H_z - \frac{\partial}{\partial z}H_y\right] \doteq \frac{1}{\epsilon}\frac{\partial}{\partial y}H_z \tag{3.52a}$$

$$\frac{\partial}{\partial t}E_y = \frac{1}{\epsilon}\left[\frac{\partial}{\partial z}H_x - \frac{\partial}{\partial x}H_z\right] \doteq -\frac{1}{\epsilon}\frac{\partial}{\partial x}H_z \tag{3.52b}$$

$$\frac{\partial}{\partial t}H_z = \frac{1}{\mu}\left[\frac{\partial}{\partial y}E_x - \frac{\partial}{\partial x}E_y\right] \tag{3.52c}$$

2. The Transverse Magnetic (TM) Group

$$\frac{\partial}{\partial t}H_x = \frac{1}{\mu}\left[\frac{\partial}{\partial z}E_y - \frac{\partial}{\partial y}E_z\right] \doteq -\frac{1}{\mu}\frac{\partial}{\partial y}E_z \tag{3.53a}$$

$$\frac{\partial}{\partial t}H_y = \frac{1}{\mu}\left[\frac{\partial}{\partial x}E_z - \frac{\partial}{\partial z}E_x\right] \doteq \frac{1}{\mu}\frac{\partial}{\partial x}E_z \tag{3.53b}$$

$$\frac{\partial}{\partial t}E_z = \frac{1}{\epsilon}\left[\frac{\partial}{\partial x}H_y - \frac{\partial}{\partial y}H_x\right] \tag{3.53c}$$

Throughout this work, we are focusing on the Transverse Electric (TE) group as its bandgap is wider and semiconductor laser diodes with compressively strained quantum films emit TE-polarized light which will be coupled into passive PhC structures.

Strictly speaking, since in any real structure, an infinitely extended rod is obviously impossible to realize, this model only represents an approximation to the real situation. The model is however fairly accurate since the optical modes are vertically confined through the introduction of a planar waveguide that is narrow enough to be fully perforated by the 2D PhC. In order to facilitate a localization of the light in-plane, the commonly known waveguiding based on total internal reflection within the waveguide due to index guiding is adopted for the two-dimensional planar photonic crystal structures. But since the waveguide structure breaks the translational symmetry in the z-direction, the TE- and TM-modes of the two-dimensional system are no true eigenstates of the 3D system. By examining the symmetry properties of the modes with respect to the planar waveguide plane, one can however identify modes that behave very much like TE- and TM-polarized electromagnetic waves.

A second consequence of the limited extension of the system in the vertical direction is the potential diffraction of light out of the waveguide plane which can

become the dominant loss mechanism if the rods are only shallowly etched into the waveguide core. If on the other hand, operating in a regime in which the rods extend well into the lower cladding of the waveguide structure, the losses can be very small and will be mainly due to out-of-plane scattering events at imperfections such as surface roughness and other deviations from the otherwise typically cylindrical shape of the rods. In this regime, a perturbative approach can be adopted to model the losses inside the structure [Ben2000] in which the 2D model is extended by the introduction of an imaginary effective index inside the holes. The 3D dielectric constant is separated into a horizontal and vertical component and corrected for by a perturbation from the holes which act as radiating dipoles. The solution of the scalar wave equation is a separable field in which one part solves the 2D PhC eigenvalue problem. It has been shown that for many 3D topologies, these simple corrections to the 2D model produce excellent agreements with experimental findings, so that the modified 2D model can often replace computationally expensive 3D calculations.

Rotational Invariance

The invariance under a 60 degree and 90 degree rotation for the triangular pattern and the square pattern, respectively, allows one to reduce a discussion of the dispersion characteristics to the so-called irreducible Brillouin zone. The hexagonal shape of the first Brillouin zone can be reproduced by a rotation of the irreducible BZ. Often it is already sufficient to discuss the dispersion behavior along the main symmetry axes of the crystal. Figure 3.6 depicts the first BZ, the irreducible BZ and identifies the high symmetry points of the respective lattice topology.

Invariance under re-scalation (Skaling Law) and under time reversal

With the following few operations [Sak2001], one can show that Maxwell's equations are invariant under a re-scaling of space and time reversal.
Re-scaling the variables for space and time to the dimensionless quantities

$$\vec{r}' = \frac{\vec{r}}{a} \qquad t' = \frac{ct}{a} \tag{3.54}$$

and defining a new dielectric function and vector field

$$\epsilon'(\vec{r'}) = \epsilon(\vec{r}) \qquad \vec{E}'(\vec{r'}, t') = \vec{E}(\vec{r}, t) \tag{3.55}$$

one can see that $\vec{E}'(\vec{r'}, t')$ satisfies the following wave equation:

$$\frac{1}{\epsilon'(\vec{r'})} \vec{\nabla}_{\vec{r'}} \times (\vec{\nabla}_{\vec{r'}} \times \vec{E}'(\vec{r'}, t')) = -\frac{\partial^2}{\partial t'^2} \vec{E}'(\vec{r'}, t') \tag{3.56}$$

which is the same dimensionless wave equation that $\vec{E}(\vec{r}/a, ct/a)$ satisfies.

This has very important implications. It is possible to undertake experiments on a millimeter scale using microwaves to verify some thought experiments before turning to the dimensions of light with its significantly higher fabricational challenges.

Furthermore, from the Master equation (3.39), one can immediately see that a time reversal keeps the wave equation invariant. It can be shown that as a direct consequence of the time reversal symmetry of the wave equation, the dispersion relation exhibits inversion symmetry, i.e.

$$\omega_n(\vec{k}) = \omega_n(-\vec{k}) \tag{3.57}$$

where n denotes the band index. The inversion symmetry of the dispersion relation will play an important role in chapters 6.2 and 6.3 for the determination of the propagation direction of light inside a PhC superprism.

 In Appendix A, three approaches for a numerical solution of the Master equation are presented: the transfer matrix method, the plane wave expansion method, and the finite difference time domain method. These methods partly exploit the invariances and symmetries discussed in the previous two chapters for their respective topologies. Figure 3.6(a) shows the calculated eigenfrequencies obtained from a plane wave method for a two-dimensional photonic crystal with square lattice structure. The air filling fraction which is defined as the ratio of the volumes occupied by low-index material (typically air) and high-index material (typically semiconductor) within the lattice's unit cell is $f = \pi(r/a)^2 =0.42$ for this example. The square topology of the lattice in real space is reproduced in reciprocal space. The band structure exhibits three high symmetry points at the
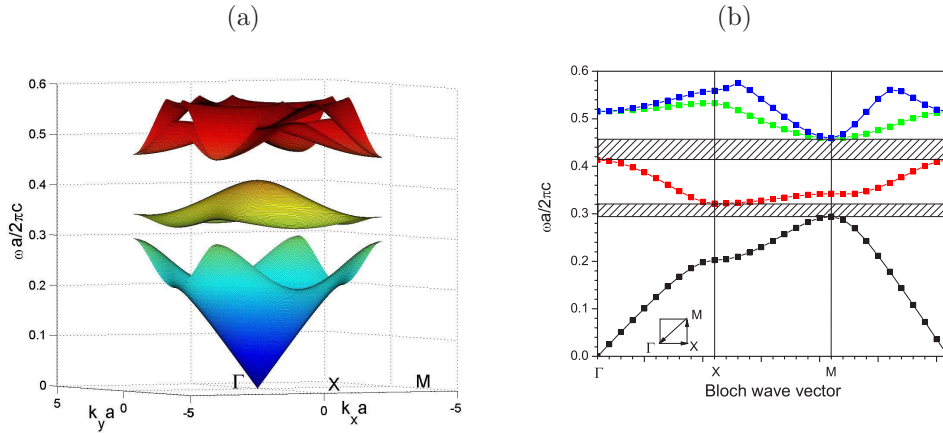
Figure 3.6: Eigenenergies as a function of in-plane Bloch wave vectors for the example of a two-dimensional photonic crystal with square lattice topology for TE-polarized light (a) as a function of the in-plane wave vector with components k_x and k_y (b) along the axes connecting the high symmetry points Γ, M, and X.

edges of the first Brillouin zone: its center labelled as the Γ-point, the k-vector closest to the Γ-point, labelled as X, and the k-vector farthest away from the Γ-point, labelled as the M-point. The area spanned by these high symmetry points is referred to as the irreducible Brillouin zone. The eigenenergies within this area sufficiently describe the band structure of the first Brillouin zone and thus the rest of the lattice. The remaining regions of the first Brillouin zone can be reconstructed by symmetry arguments.

In many cases, it is sufficient to reduce the description of the band structure to the k-vectors along the axes connecting the high symmetry points, henceforth referred to as the Γ-M, Γ-X, and X-M directions of the two-dimensional square lattice. This reduced picture is shown in Figure 3.6(b). The inset shows the selection of k-vectors chosen for this diagram, the shaded areas indicate the bandgaps for TE-polarized light. The energy range in which neither TE- nor TM-polarized light is allowed to exist is denoted as a complete bandgap, the energy range in which no modes are allowed to exist only for a particular symmetry direction is referred to as a stop band.

3.2.3   Comparison with electronic band structures

At this point, it is very instructive to compare the Master equation (3.43) with the Schrödinger equation

$$\left(-\frac{\hbar^2}{2m}\vec{\nabla}^2 + F(\vec{r})\right)\Psi(\vec{r}) \equiv \hat{\mathcal{H}}(\vec{r})\Psi(\vec{r}) = E\Psi(\vec{r}) \qquad . \qquad (3.58)$$

The Hamilton operator $\hat{\mathcal{H}}$ is determined by the electric potential $F(\vec{r})$ which represents a perturbation to the system. In a solid where the potential electrical energy is varying periodically with the distance of the atomic layers[7] this leads to the formation of energy bands and a bandgap for electrons. As the operator $\hat{\Theta}_H$ is essentially determined by the dielectric function, a periodic modulation of the dielectric function similarly leads to the formation of a "photonic" bandgap. This is the central idea behind the photonic bandgap theory. The simplicity of the concept and the amazing consequences it has in controlling the propagation of light has made research on photonic crystals one of the most exciting fields of research in the past decade.

Since F is invariant with respect to a translation $\hat{T}$ by a vector $\vec{R}$, i.e. $F(\vec{r}) \equiv F(\vec{r} + \vec{R})$, also the Hamilton operator will be invariant with respect to such a transformation so that $\hat{T} = e^{i\vec{k}\vec{R}}$ and $\hat{\mathcal{H}}$ commute, just as $\hat{T}$ and $\hat{\Theta}_H$ were commuting for the photonic crystal.

Both $\hat{\Theta}_H$ and $\hat{\mathcal{H}}$ are Hermetian operators which has two important implications for the solution of the eigenvalue problem:

1. Their eigenfunctions are building a complete and orthonormal basis in their respective spaces.

2. Their eigenvalues E and ω are real and represent the observables of the system. Due to the apparent analogy, throughout this work, the words energy and frequency (and angular frequency) are sometimes interchanged when referring to electromagnetic modes.

Assuming $\epsilon(\vec{r})$ and F are scalars, it becomes apparent that F and $1/\epsilon$ represent perturbations that have a similar impact on the system's eigenvalues. The interpretation of the inverse dielectric function as an effective potential allows one to

---

[7]on wavelength scale of the de Broglie wavelength

deduce the electromagnetic equivalents to two important theorems of quantum mechanics, the variational theorem and the non-crossing theorem.

Variational theorem

One often has to resort to approximations if one wants to solve the Schrödinger equation (3.58). Among the approximation schemes are: the time-independent perturbation theory, the time-dependent (Dirac-) perturbation theory, the semi-classical WKB-method[8], and approximations according to the variational theorem, to name a few. In later chapters, reference will be sometimes made to the variational theorem as it can be easily extended to electromagnetism and assist in understanding many questions with respect to the distribution of electromagnetic fields in the periodic dielectric structure of the photonic crystal. It is based on the so called extremum theorem and finds its derivatives in the Ritz variational theorem and the Hartree equations.

Considering the similarity of the roles of $\hat{F}$ and $(1/\epsilon)$ play in their respective eigenvalue equations (3.58) and (3.43), one can formulate an electromagnetic variational principle: the modes will lower their eigenvalues if they have large amplitudes in regions of small perturbation (F or $1/\epsilon$). For the periodic dielectric structures that will be investigated in this work, this means that a mode can lower its energy if its electric field is located in regions of high dielectric constant (small $1/\epsilon$). As one can see, it is sometimes instructive to interpret the inverse dielectric constant as an effective potential.

The electromagnetic variational principle will also help to understand the formation of stop bands in the dispersion relations of a photonic crystal. Since the lowest mode in a periodic dielectric lattice structure will locate its electric field in regions of high dielectric constant, the next higher mode will be forced to partially penetrate regions of lower dielectric constant in order to stay orthogonal to the lower mode, resulting in a higher energy that produces an avoided crossing point. Consequently, degeneracies cannot occur for modes of common symmetry in the dispersion relations of photonic crystals.

---

[8]This method was proposed simultaneously and independently by the three scientists Wentzel, Kramers, and Brillouin, giving an obvious reason for its name.

Non-crossing theorem

A very important theorem of quantum mechanics that extends into many fields of physics was first postulated by von Neumann and Wigner [Neum1929]. They argued that unless certain symmetry conditions apply to a system of two quantum states, the two states generally do not cross under the adiabatic change of a single parameter q. The coupling between two states can often be described by a Hermetian operator such as the Hamilton operator or operator $\hat{\Theta}_H$ and the system's perturbation is then characterized by the tensor's off-diagonal matrix elements.

In the band structure of a solid where the perturbation is given by the periodic modulation of the potential energy, it explains the energy splitting at the edge of the Brillouin zone. One might ask which states couple and why they couple at the boundary of the Brillouin zone. The answer lies in the fact that in the electronic lattice of a solid, the wave functions experience a Bragg reflection at the Brillouin zone boundary to form a standing wave if their respective wavevector ends at Brillouin zone boundary. The coupling between the forward and backward propagating waves at the boundary then produces the observed energy splitting. As discussed in chapter 3.2.3, the interpretation of the inverse dielectric constant as an effective potential is again very instructive. The situation is more complex however due to the higher dimension of the system's eigenfunctions compared to a perturbation of the Hamilton operator. The eigenfunctions of $\hat{\Theta}_H$ are the magnetic field vectors of the respective band so that one has to take into account their symmetry in order to understand the various avoided crossing phenomena of the dispersion relations: only eigenfunctions of common symmetry will interact to form avoided crossing points.

While the parallels are numerous and compelling, it should be noted that there are of course also major differences between electromagnetic modes and quantum mechanical eigenstates. One lies in the fact that the eigenfunctions of $\hat{\Theta}_H$ are vectors rather than scalars, thus introducing a more complex symmetry behavior and making the formulation of boundary conditions more complex. The propagation of electromagnetic modes in a PhC strongly depends on their respective

polarization state. Secondly, one should not forget that photons are bosons while electrons are fermions which has many important consequences, one of which is that photonic bands do not 'fill up'. A comprehensive comparison between the quantum mechanics in a periodic potential and the electromagnetism in a periodic dielectric is given in [Joa1995].

Chapter 4

Operation of 2D PhC in the bandgap: Reflectors

In this chapter, the effect of 2D photonic crystals operated in the bandgap embedded in planar waveguide structures is discussed. The main focus of this chapter lies in the application of the embedded 2D photonic crystals as reflectors and very effective waveguide and coupler structures which is documented in various experiments.

In an introductory chapter 4.1, two competing schemes of confining light in the vertical direction, i.e. in the direction normal to the waveguide plane on one hand and within the waveguide plane using photonic crystals are discussed. Chapter 4.2 describes the application of 2D photonic crystal reflectors in an integrated tunable coupled-cavity laser design. This chapter first introduces the Vernier concept of extending the tuning range of a semiconductor laser and the role of the 2D photonic crystal reflectors in an integrated tunable laser design. The following chapter 5.1 furthers the discussion of how light is influenced by embedding a 2D PhC in a planar waveguide structure by introducing chains of defects in the bulk PhC lattice and the nature of light propagating in such a defect structure. Chapter 5.2 presents a tunable semiconductor laser design based on longitudinally coupled photonic crystal channel waveguides. Finally, chapter 5.4 presents a two-channel tunable laser diode design based on photonic crystals including a discussion how to efficiently guide light through photonic crystal waveguide bends.

4.1   Light confinement in planar waveguide structures

There are a multitude of possible implementations of 2D PhC structures due to the freedom of choosing the nature of the lateral and vertical photon confinement. In view of the introductory remarks of the first chapter where it was stated that a key motivation to the investigation of photonic crystals is to be finally able to control and manipulate the flow of light in very small dimensions, hence overcoming the deficiencies of classical optical devices which typically require device dimensions of several cm^2, almost all research groups in this field investigate structures that provide a strong lateral photon confinement with a very few exceptions in which weak lateral confinement is provided in a polymer material system [Eich2002]. This strong lateral confinement is accomplished by choosing material systems that provide a strong index contrast. An often realized system is to define pores or rods of low index material such as air or SiO_2 in a high index semiconductor backbone with a typical refractive index in the range of 3.5. This allows the fabrication of ultra-small bends on one hand, but on the other hand increases the out of plane losses in straight waveguide sections due to incoherent (Rayleigh-type) scattering at the waveguide boundaries. Setting the dimensions of a 2D PhC such that the wavelength range passing through or generated within the structure coincides with the spectral position of the photonic bandgap, the photonic crystal can serve as a very efficient reflector and waveguide as it provides strong lateral photon confinement.

The question of how to control the propagation of light in the vertical direction becomes necessary in any real structure as it is in fact three-dimensional considering the fact that only finite vertical structures can be defined. Vertical confinement can be either realized by choosing a large index contrast as well or one can use the weak index guiding provided for example by a planar waveguide structure.

In the former family of devices, the optical modes are guided by total internal reflection (TIR) within a thin membrane plane. Members of this family include designs in which either air or a low index material is used as a host of the high index waveguide core. Example material systems are Si (n=3.5) on SiO_2 (n=1.45)

or a high index core on top of an air gap, often referred to as the membrane or air bridge structure. The in-plane waveguiding is essentially comparable for both types with a slight asymmetry in the vertical mode structure for the air/Si/SiO$_2$ system. In order to facilitate waveguiding by TIR in these structures, the height of the membrane has to be in the range of a quarter wavelength, i.e. for light at around 1.55 μm this demands widths in the range of 400 nm. Therefore, the demanded aspect ratios of the etched air cylinders are only about 1:1, thus presenting a fabricational advantage compared to the latter systems with low vertical index contrast. It allows the fabrication of nearly perfectly shaped air cylinders and is therefore the preferred choice when investigating devices with very small areas such as high-Q defect cavities or small-bandwidth waveguides where a high degree of light trapping is preferred compared to using large bandwidths as efficient light guiding mechanism. Unfortunately, the bandwidth of these structures can in many cases be very limited due to strong scattering losses of modes above the light line of the cladding [1], known as the so called light cone problem [Och2001a]. Consequently, only modes within a narrow frequency band that typically exhibit low group velocities are allowed to exist. A carefully designed waveguide, however, can exhibit a guided Bloch mode that completely avoids the intrinsic losses and leads to a truly loss-less mode propagation [Baets2003, Baets2004]. On the other hand, the air gap below the membrane prevents an efficient flow of heat generated in the structure so that it effectively prevents the implementation of laser structures on these systems.

In a second family, the low vertical index contrast systems, vertical confinement is provided by the weak index guiding of a planar waveguide structure. Fabricational demands are higher since the low-index (typically air) pores have to extend over the thickness of the complete waveguide structure in order to reduce scattering losses out of the planar waveguide plane. Etch depths required for these kind of systems are in the range of three to four μm. By approximating the holes in the waveguide core as radiating electric dipoles presenting a perturbation

---

[1] The light line or, more generally, the light cone of the cladding is defined as the dispersion relation of light propagating in a dielectric medium of refractive index n given by $\omega(k) = ck/n_{cl}$. Modes above the light cone can couple onto the continuum of radiative modes and propagate into free space.

to the perfect 2D structure, it has been shown that the field can be separated into an in-plane and a vertical distribution with the in-plane distribution solving the 2D problem. All Bloch modes propagating in the plane of the waveguide are above the light line of the cladding which only has a slightly smaller refractive index compared to the waveguide core so that a truly lossless propagation can only be implemented using the high index contrast air bridge topology. Nonetheless, it was shown that in any real system involving complex photonic circuitry, the intrinsic losses of weakly confined structures can be smaller than those of highly confined topologies due to two facts. Firstly, the stronger confinement in the air bridge structures results in a stronger interaction of its modes with the waveguide boundary. Secondly, compared to an effective mode index of at least 3 in the weakly confined system, the effective index of modes in the highly confined system is in the range of 2.6, supporting the radiation mechanism. Unlike the air-bridge structure, the deeply etched weakly confined topology facilitates an efficient flow of heat away from the active layers which is essential for the realization of any active device. On the other hand, the larger optical mode volumes in the weakly confined systems limit their application to control the rate of spontaneous emission due to smaller available Purcell factors[2].

The question arises which of two complementary systems described above is the better one. The answer is not straightforward and depends on the application. Generally, for applications in which small optical mode volumes are desirable such as the Purcell effect and enhancement of non-linear effects, the highly confined air bridge structure is the favorable configuration. Applications involving complex photonic circuitry with multiple sharp waveguide bends or devices integrating active and passive components can be better implemented in the deeply etched, weakly confined topology. Consequently, throughout this work, a system of deeply etched air cylinders in an active or passive planar waveguide structure is investigated, therefore providing high lateral but low transverse photon confinement.

First, the existence of a photonic bandgap, a spectral region in which no modes are allowed to exist, is used to build very efficient reflectors and waveguide struc-

---

[2]The Purcell factor is proportional to the cavity-Q and inversely proportional to the effective optical mode volume.
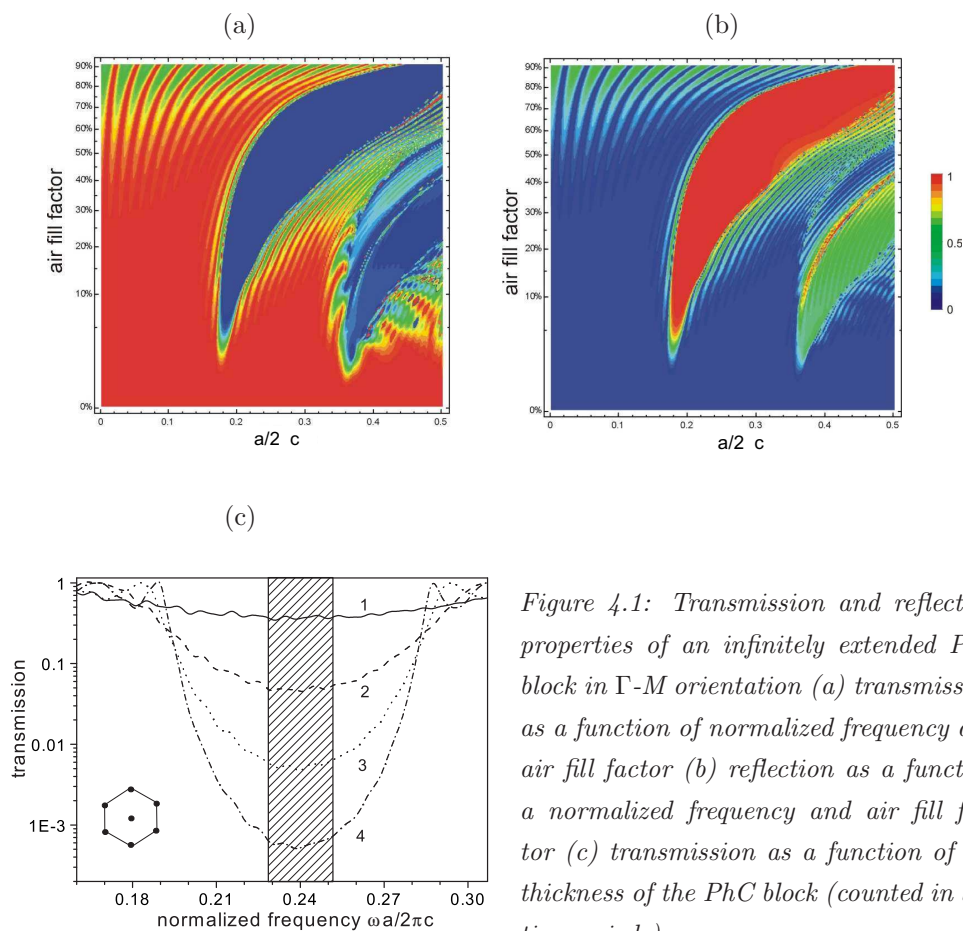
(a)

(b)

(c)

Figure 4.1: Transmission and reflection properties of an infinitely extended PhC block in Γ-M orientation (a) transmission as a function of normalized frequency and air fill factor (b) reflection as a function a normalized frequency and air fill factor (c) transmission as a function of the thickness of the PhC block (counted in lattice periods).

tures. Two resonators are coupled contra-directionally to build a widely tunable laser diode. Two such tunable laser sources are then integrated into a two channel light source by combining their light output into a common output waveguide by means of a photonic crystal based Y-coupler structure.

Within the waveguide plane, light is confined through the periodic modulation of the dielectric function on a length scale of the wavelength of light. The periodicity of the lattice and the resulting folding of the dispersion curves results in the formation of frequency gaps in which no light is allowed to propagate. Using the finite difference time domain algorithm outlined in Appendix A.2, one is able to compute the transmitted optical power as a function of normalized frequency $\omega a/2\pi c$. Figure 4.1 shows such a transmission diagram for the case of an infinitely extended array of air cylinders in a dielectric.

If one wants to use a photonic crystal block as a reflector in an integrated laser design, it is desirable to have the freedom of selecting the reflectivity of the mirror. This can be achieved by two means:

1. A variation of the PhC crystal lattice parameters

2. A variation in the number of PhC rows in either lattice orientation.

Through an appropriate selection of these parameters, it is possible to select any desired mirror reflectivity from 0 to 1: low reflectivities can be achieved through a small number of rows and lattice parameters outside the photonic bandgap whereas high reflectivities can be achieved through a large number of rows and lattice parameters that create a photonic bandgap that coincides with the wavelength of the incident light. Figure 4.1 shows a so called gap map, the calculated transmission and reflection of an infinitely extended PhC block in Γ-M orientation as a function of the air fill factor and normalized frequency. The plots are obtained from a calculation based on the transfer matrix method described in Appendix A.1.

Figure 4.1(c) shows the calculated transmission through a triangular PhC block of one to four lattice periods in Γ-M orientation with the air fill factor and lattice period chosen such that the bandgap of the infinitely extended crystal has its center at approximately 1550 nm. As expected, the transmission decreases exponentially with a linear increase in the number of rows. Although one can achieve the desired reflectivity solely through an adjustment of the lattice parameters alone, it becomes difficult to select intermediate values since the reflectivity changes dramatically with small changes of energy in the vicinity of the photonic bandgap. As a consequence, intermediate reflectivities will only hold for a very small frequency range which is inappropriate for the widely tunable laser sources investigated in this work and furthermore make the design very sensitive to fabricational variations for example of the air fill factor. A better approach to achieve intermediate reflectivities is to operate inside the photonic bandgap and to select the appropriate number of PhC rows. For example, operating inside the photonic bandgap and selecting a width of the photonic crystal block of one lattice period results in a transmission that varies only between 37±2% in the relevant normalized frequency window from 0.23 to 0.25, thus providing a sufficiently uniform

reflectance for the various frequencies of the incident beams.

4.2 Application to coupled resonators with photonic crystal reflectors and gain-coupled distributed feedback

In this chapter, the application of photonic crystal reflectors in an integrated tunable laser design will be discussed. As motivated in chapter 2, active laser sources are required for both optical communication networks as well as any future photonic microchip to allow the processing of information. Light sources with a variable emission wavelength obviously promise parallel data processing and are therefore an important component in the development of the new technology. Already in today's optical networks, wavelength tunable laser diodes can significantly simplify the maintenance of transmission systems by reducing the complexity of component stocks for network providers.

Tuning mechanisms

The wavelength in a semiconductor laser can be tuned either by a modulation of the temperature of the active layers or by an increase in carrier density. The maximum tuning range one can achieve by temperature modulation is in the range of 10 nm. Considering heating due to losses in the active layers as well as Joule heating, the temperature changes with the square of the segment bias [Bra1994]. Therefore, the following approximation for the change in temperature can be made:

$$
\begin{aligned}
\Delta T(I) &= R_T V_j I^{nr} + R_T R_d I^2 \\
&= R_T V_j \left[(I - I^{th})(1 - \eta_{tot}) + I^{th} \right] + R_T R_d I^2
\end{aligned}
\tag{4.1}
$$

where V_j the junction voltage, I^{th} the threshold current, η_{tot} is the total continuous-wave quantum efficiency that is vanishing below threshold, R_T is the thermal impedance, and R_d is an effective differential resistance of the laser structure

$$
R_d = \left[\frac{\rho_a d_a}{A} \left(\frac{d_a}{2 K_a R_T A} + 1 \right) + \sum_l \frac{\rho_l d_l}{A} \right]
\tag{4.2}
$$

where ρ_a, d_a, and K_a are the thickness, ohmic resistivity and thermal conductivity of the active layer, d_l and ρ_l are the thickness and ohmic resistivity of the other layers of the device structure, and A is the area through which current and heat are flowing [Bra1994]. The maximum tuning range by a variation in the carrier density is in the range of 5 nm.

Carrier injection in a laser diode typically results in a combination of both tuning schemes:

$$\Delta\lambda(\Delta N, \Delta T) = \frac{\partial\lambda}{\partial n'}\frac{\partial n'}{\partial N}\Delta N + \frac{\partial\lambda}{\partial n'}\frac{\partial n'}{\partial T}\Delta T \ . \tag{4.3}$$

The change in carrier density ΔN can be calculated according to equation (3.8), the increase in temperature can be calculated according to (4.1). The increase in device temperature leads to a reduction in the size of the bandgap and therefore the excitonic energies so that the emitted photons exhibit larger wavelengths. In a separate measurement where the laser's emission wavelength is recorded as a function of the temperature of the heat sink, $\frac{\partial\lambda}{\partial n'}\frac{\partial n'}{\partial T}$ is found to be approximately 0.095 nm/K. The corresponding measurement setup is described in Appendix C.1. The factor $\frac{\partial\lambda}{\partial n'}\frac{\partial n'}{\partial N}$ is assumed to be 8.3 10^{-25} nm m^3 and accounts for the carrier effects of bandfilling (Burstein-Moss effect) and intraband free carrier absorption, also known as plasma effect.

Vernier effect

A common concept to extend the tuning range of a semiconductor laser is to contra-directionally couple two or more laser resonators whose longitudinal modes are shifted relative to each other. In semiconductor lasers, the shift is commonly accomplished by applying currents in the different sections of the laser. Depending on whether the region is active or passive the above described carrier and heating effects lead to a spectral shift of the longitudinal modes. The tuning principle is based on the coupling of the longitudinal modes of two waveguides and is schematically illustrated in Figure 4.2. Changes in the refractive index by current injection into one waveguide lead to a spectral shift according to (4.3) of its cavity modes relative to the second unperturbed mode comb and therefore a modified interference spectrum. Laser emission occurs where two modes have sufficient overlap. The two sets of modes overlap periodically leading to a cycli-
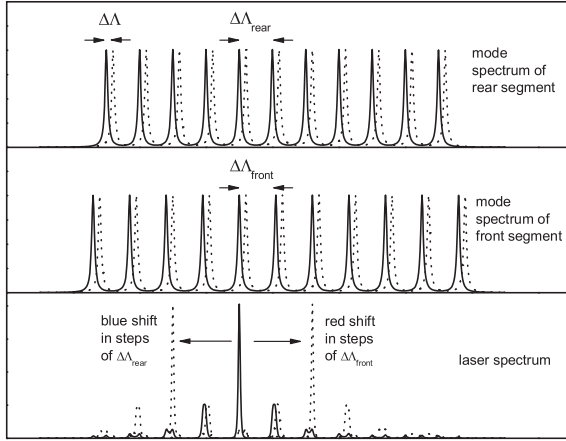
Figure 4.2: Illustration of the Vernier effect.

cal switching behavior. The result is a discontinuous switching of the emission
wavelength on a grid defined by the alternate cavity mode spacing according to
(5.1).

In particular, varying the current in the resonator with larger longitudinal mode
spacing result in discrete shifts of the emission wavelength towards smaller wave-
lengths in steps defined by the mode spacing of the resonator with smaller mode
spacings. The finite number of longitudinal modes in the gain spectrum leads to
a cyclical overlap between the two mode combs, resulting in a cyclical wavelength
switching. Changing the current in the resonator with smaller longitudinal mode
spacing similarly changes the emission wavelength cyclically towards larger wave-
lengths on a wavelength grid defined by the larger mode spacing. This tuning
mechanism is referred to as the Vernier effect.

As the current into both resonators is increased simultaneously, both mode combs
shift towards higher wavelengths resulting in a continuous red shift of the laser
wavelength and thus a fine tuning of the emission wavelength. This tuning scheme
can be used to bridge the gaps between the coarse set of modes fixed by the lon-
gitudinal mode spacing defined by the grating structure. It shall be noted here
that the tuning concept illustrated in Figure 4.2 is an oversimplified picture of
the real physical situation. The symmetry of the coupled modes in fact prohibits
a modal overlap as discussed in chapter 3.2.3. The basic idea of the wavelength
switching however still holds and leads to an enhanced tuning range that can be
qualitatively understood considering the Vernier concept.

In this work, two tunable laser designs are investigated that both utilize the

Vernier tuning concept. In a first design, discussed in this chapter, the longitudinal mode spectra of the two coupled resonators are defined by a multi-wavelength distributed feedback grating defined laterally to two ridge waveguide segments. In a second, more compact design that will be discussed in chapter 5.2, the longitudinal mode spectra are defined through the free spectral range of their respective photonic crystal channel waveguides.

The first device combines the concept of photonic crystals and multi-wavelength distributed feedback leading to an enhanced design freedom to control the optical properties of the device. A binary superimposed grating (BSG) defines the mode comb in each resonator with respect to the number of modes, their spectral position, and amplitude. The introduction of a photonic crystal between the resonators facilitates control over the intra-cavity coupling properties.

Device processing

The fabrication process is schematically illustrated in Figure 4.3(a) through (h). The devices are based on a gas source molecular beam epitaxy grown InGaAsP quantum well structure with four compressively strained (1%) wells and lattice matched barriers. A separate confinement heterostructure is used for transversal photon confinement. The details of the epitaxial layer system A52980 on which the devices are based on are described in Appendix D. A 1 cm^2 sample piece is cleaved from the four inch diameter wafer.

In a first fabrication step, two longitudinally arranged 2.5 μm wide and 400 μm long ridge waveguides are defined with an intermediate gap of 8 μm. For this purpose, a 1500 nm thick PMMA resist layer is coated onto the organically cleaned sample surface. The two rectangular areas defining the ridges are aligned parallel to one of the cleaved sample facets and patterned into the resist by electron beam lithography (current 2 nA, dose 650 μC/cm^2) (a). The sample is developed for about one minute in a solution containing methylisobutylketon (MIBK) and isopropanol at a ratio of 1:3 and subsequently dipped in isopropanol for about 10 s (b). As a rule of thumb, in any lift-off process, the resist layer should be three to five times as thick as the deposited mask layer in order to ensure a successful lift-off step. Therefore, an etch mask of 40 nm thick BaF$_2$ and 60 nm Cr is evaporated onto the sample by electron beam evaporation with the unexposed mask
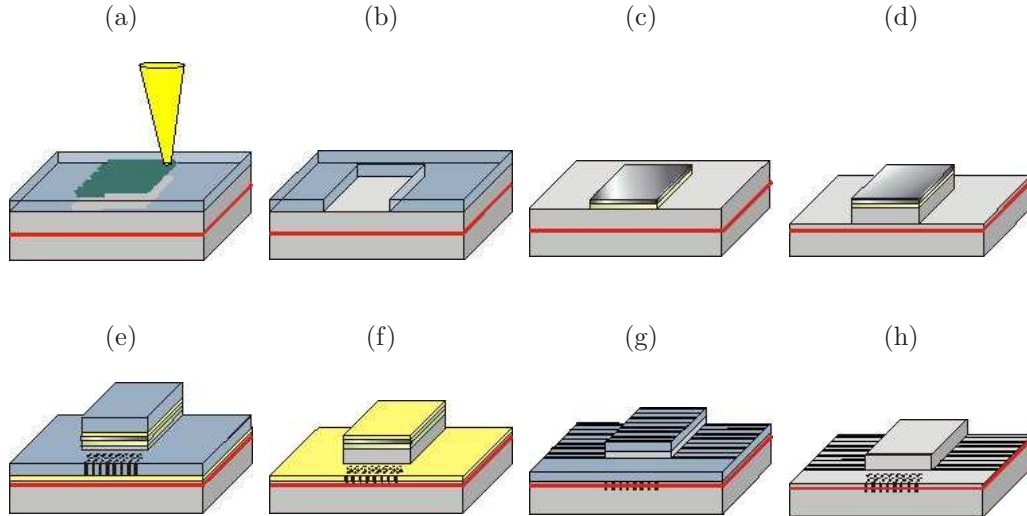
Figure 4.3: Process steps for the fabrication of the tunable laser diode with gain-coupled distributed feedback and photonic crystal reflectors.

areas being removed by lift-off in a heat bath of 1-methyl-2-pyrrolidon heated at 353 K (c). The ridges are etched to a residual etch depth of about 150-180 nm to the waveguide structure (d) as this distance was shown to provide optimum coupling of the fundamental mode to a lateral grating (see finite elements simulation later in this chapter).

In a second fabrication step, photonic crystal sections with one period in Γ-M orientation are defined between and at the end of the partial resonators. A 200 nm thick SiO_2 mask is sputtered onto the sample followed by a 500 nm thick polymethylmethacrylate (PMMA) resist layer. The photonic crystal pattern is defined using electron beam lithography (600 pA, dose 600 $\mu C/cm^2$) in the resist as illustrated in Figure 4.3(e). The sample is developed for about one minute. The pattern is subsequently transferred into the SiO_2 mask using a CHF_3 /Ar based dry etch process and finally etched around 3 μm into the semiconductor using a highly anisotropic Cl_2 /Ar based electron cyclotron resonance reactive ion etching process [Happ2001] as illustrated in Fig. 4.3(g). The photonic crystals have lattice periods of 360 nm and air fill factors of 33% leading to the desired reflectivities of about 65%. The dimensions have been chosen such that the lasing wavelength lies in the center of the photonic bandgap. The rear facet consists

of a highly reflective photonic crystal mirror section with 4 lattice periods of the same dimensions resulting in reflectivities near unity.

In a third process step, the binary superimposed grating is structured laterally to the ridge segments by electron lithography. For this purpose, the sample is coated with 150 nm PMMA and the grating pattern is defined by electron beam lithography at a current of 600 pA and a dose of about 510 $\mu C/cm^2$ (g). A 50 nm thick Cr layer is deposited by electron beam evaporation and selectively removed by lift-off at those sample regions that were not exposed (h).

In a fourth process step, the sample is passivated. BCB is infiltrated into the air pores as well as deposited beyond the height of the ridge waveguide and dried by placing the sample onto a hot plate whose temperature is gradually decreased from 523 K down to 363 K within a time frame of 1 hour. The excessive BCB on top of the ridges is removed in an oxidization process involving CHF_3 and O_2.

In a final fabrication step, the contacts are defined on the sample surface. While the n-contact extends over the entire bottom of the sample surface, the p-contact is defined only on those regions where current injection is intended, in this case on top of the ridge sections. In order to allow a convenient positioning of the probe arms on the p-contact, wide contact pads of about 200 μm by 200 μm are defined adjacent, yet electrically connected, to the ridges. For this purpose, the sample is coated with 1500 nm PMMA electron beam resist and exposed in the relevant regions on top of the ridges by electron beam lithography (current 3 nA, dose 422 $\mu C/cm^2$). The exposed PMMA areas are selectively removed and 25 nm Ti, 165 nm Pt, and 500 nm Au are evaporated on the p-side of the sample. A lift off process removes the metal areas where no current injection is intended. The n-contact is deposited onto the bottom side of the sample and consists of the following series of metal layers: a 390 nm thick Au/Ge layer, 130 nm Ni, and 420 nm Au. While the Au/Ge layer is deposited by thermal evaporation, the Ni and Au layers are again deposited by electron beam evaporation. The n-contact is then heated for about 30s in a nitrogen atmosphere. Finally, front facets are cleaved.

A main challenge during the fabrication was the overlay of the various layers due to the spatial drift of the electron beam with exposure time and temperature. Particularly the placement of the PhC sections between the ridge waveguides pre-
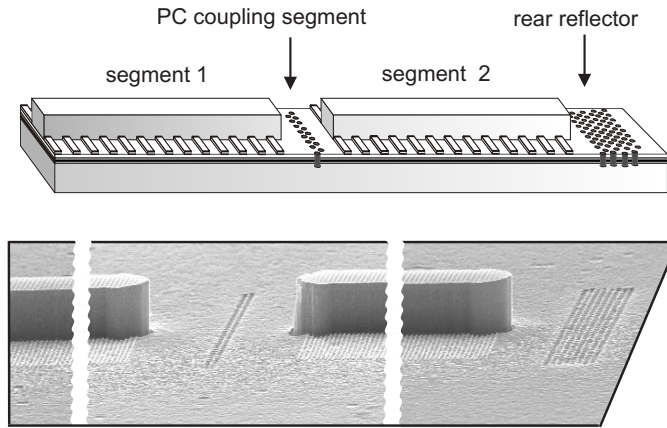
Figure 4.4: Top left: SEM micrograph of ridge waveguide resonator with lateral Cr grating that defines the BSG lattice. Top right: SEM micrograph of photonic crystal rear mirror. Bottom: total design with the two resonators and two contact pads for independent current injection.
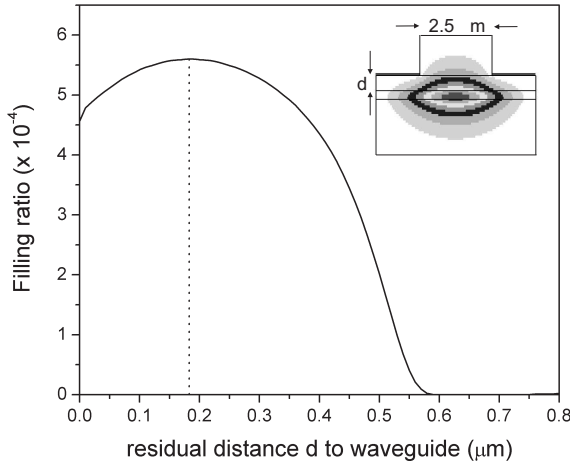

Figure 4.5: Calculated filling factor of lateral grating as a function of residual distance d from waveguide.

sented a major challenge that could only be overcome by separating the exposure into several sections, therefore allowing for an intermediate realignment of the levels to predefined reference marks.

Figure 4.4 shows an example of such a laser design. The device allows the monolithic integration with other devices such as optical amplifiers and modulators to build more complex photonic integrated circuits as will be demonstrated later in this chapter.

BSG gratings

The binary superimposed metallic gratings modify both the real and the imaginary part (or gain) of the refractive index and hence the longitudinal mode spectra of partial resonators 1 and 2. The nature of the coupling is referred to as complex coupling since the metallic grating modifies both the real and the

imaginary part of the refractive index. For comparison, a grating that modulates either only the real or imaginary part of the refractive index is referred to as index coupling or gain coupling, respectively. The imaginary part of the index contrast between Cr and the surrounding material, here BCB, exceeds the real part so that gain coupling is dominating for the devices investigated in this chapter.

Binary superimposed gratings allow the definition of multiple reflection peaks as well as their spectral positions and amplitudes through complex coupled distributed feedback to the laser cavities. Multiple Bragg reflections at the desired spectral positions λ_j are defined by the respective grating periods

$$\Lambda_j = \lambda_j/2n(\lambda_j) \tag{4.4}$$

where $n(\lambda)$ describes the chromatic waveguide dispersion. The superimposed grating is then obtained by an analog superposition of the individual gratings

$$f(x) = \sum_{j=1}^{N} a_j \sin\left(\frac{2\pi x}{\Lambda_j} + \Psi_j\right) \tag{4.5}$$

and a subsequent digitization according to [Avr1998]:

$$n_i(\lambda) = \left\{ \begin{array}{lll} n(\lambda) + \Delta n/2 & : & f[s(i-1/2)] > 0 \\ n(\lambda) - \Delta n/2 & : & f[s(i-1/2)] < 0 \end{array} \right\} \tag{4.6}$$

where i and s denote the resonator number and resonator length, respectively. The amplitude factor a_j can be used to weigh the reflection peaks in the desired manner, Ψ_j is a phase constant that is used for further optimization of the reflection spectrum. The result is a binary modulation of the complex refractive index that can be conveniently implemented using standard electron beam lithography. By means of a finite elements algorithm, it has been found that a residual depth of 180 nm to the waveguide provides optimum coupling of the lateral metal grating to the fundamental mode propagating in the ridge waveguide. Fig. 4.5 displays the filling ratio of the metal grating, which is given by the overlap of the evanescent field of the fundamental mode (FM) propagating in the ridge waveguide with the metal grating, as a function of residual depth to the waveguide. The inset of Fig. 4.5 shows the lateral distribution of the electric field of the fundamental mode propagating in the ridge waveguide of width 2.5 μm. The high absorption
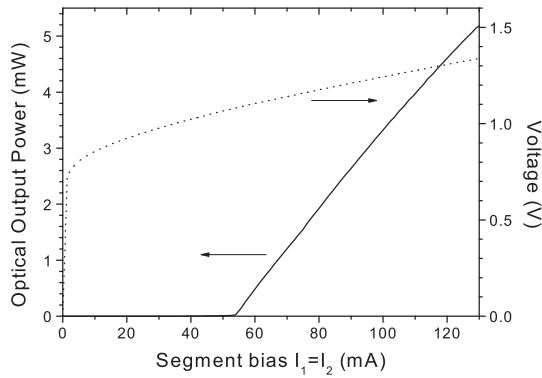
Figure 4.6: PI-characteristics and voltage drop across laser diode design with gain-coupled distributed feedback.
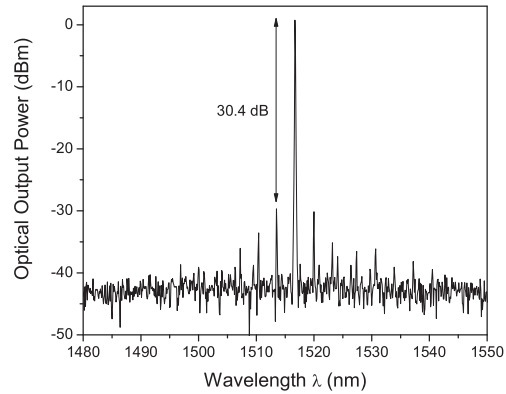
Figure 4.7: Exemplary output spectrum for front resonator bias current I_1=68 mA and rear resonator bias current I_2=40 mA.

coefficient of the metal grating requires only moderate filling ratios of about $5 \cdot 10^4$ to obtain an appreciable coupling between the FM and the metal grating.

In our example, the binary superimposed gratings define reflection spectra with 10 modes spaced 3.1 nm and 3.3 nm apart respectively.

Figure 4.6 shows the voltage drop across the laser diode and the emitted output power as a function of segment bias. Maximum output powers are in the range of 6-9 mW. The laser exhibits a junction voltage of about 0.9 V, a differential resistance of 4 Ω at a threshold of 53 mA, and an external quantum efficiency of about 68 mW/A. This external quantum efficiency is typical for InGaAsP-based quantum well lasers [Muel2001]: since the probability for Auger recombination events increases exponentially as the (electronic) bandgap decreases [Col1995], In-GaAsP quantum well lasers with their comparatively large emission wavelength suffer from reduced internal quantum efficiencies as a result of large Auger recombination rates. Fig. 4.7 shows an exemplary emission spectrum for a front and rear resonator current of I_1=68 mA and I_2=40 mA, respectively. The side mode suppression ratio in this example is 30.4 dB, but can generally vary between 20 to 35 dB depending on the bias conditions. The spectrum also shows the side modes defined by the BSG grating.
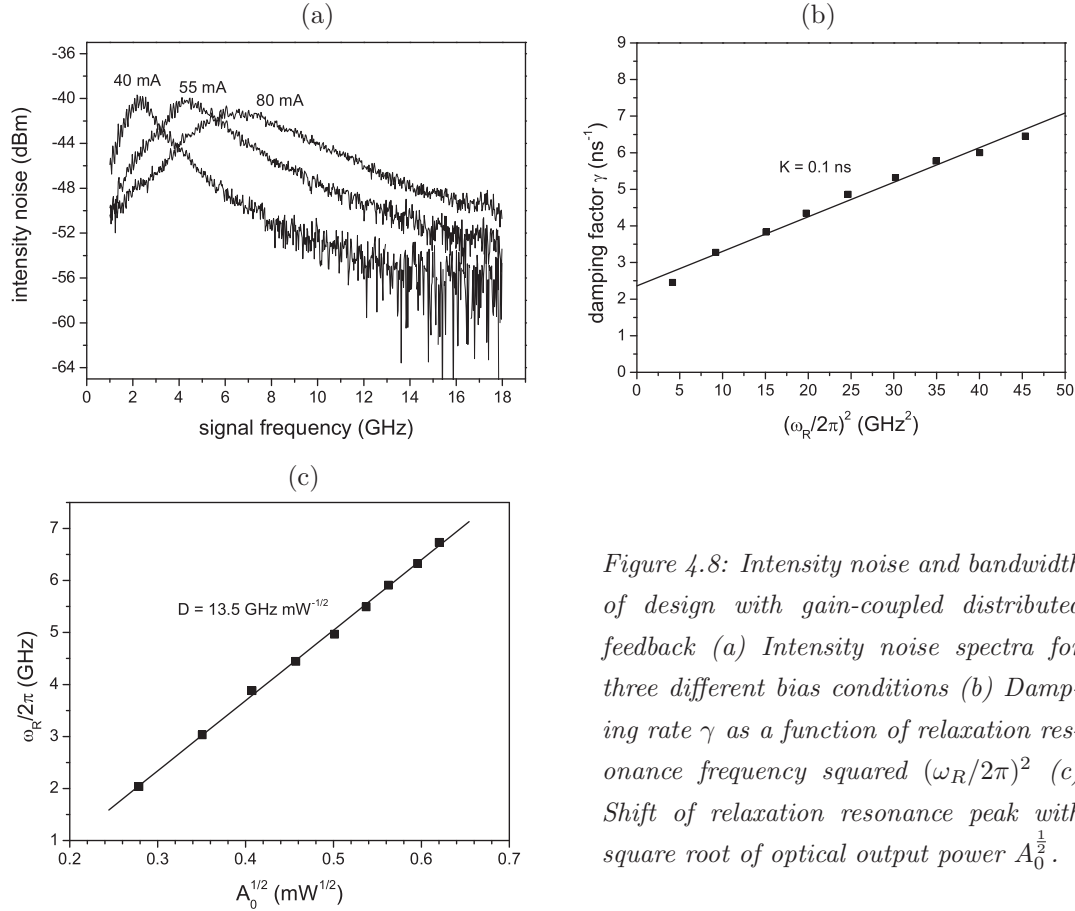
Figure 4.8: Intensity noise and bandwidth of design with gain-coupled distributed feedback (a) Intensity noise spectra for three different bias conditions (b) Damping rate γ as a function of relaxation resonance frequency squared $(\omega_R/2\pi)^2$ (c) Shift of relaxation resonance peak with square root of optical output power $A_0^{\frac{1}{2}}$.

Dynamic device properties

In order to further assess the optical properties of this laser design, its dynamic properties are evaluated by measuring its intensity noise spectrum and linewidth. Firstly, the frequency resolved optical output power is collected under fixed bias conditions using the measurement setup illustrated in Appendix C.2. Figure 4.8(a) shows the measured intensity noise as a function of frequency. The frequency at which the response drops to half of its dc value is referred to as the 3 dB cutoff. As can be seen, the relaxation resonance shifts towards higher frequency with increased output power. The measured data is fitted to the following function

$$\frac{RIN}{\Delta f} = \frac{A_1 + A_2\omega^2}{(\omega^2 - \omega_R^2)^2 + \gamma^2\omega^2} + A_3 \qquad (A_i \text{ fitting parameters}) \qquad (4.7)$$

which is obtained by plugging eqn. (3.25) into (3.33). Using the definitions
introduced in chapter 3.1.3, the relaxation resonance frequency ω_R and damping
rate γ can be expressed as

$$
\begin{aligned}
\omega_R^2 &= \Xi_{NP}\Xi_{PN} + \Xi_{NN}\Xi_{PP} = \frac{u}{\tau_p}\frac{\partial g}{\partial N}N_p + \left[\frac{\Gamma u N_p}{\tau_{\Delta N}}\frac{\partial g}{\partial N_p} + \frac{\Gamma R'_{sp}}{N_p\tau_{\Delta N}}\right]\left[1 - \frac{\tau_{\Delta N}}{\tau'_{\Delta N}}\right] \\
&\quad + \frac{1}{\tau'_{\Delta N\tau_p}} \approx \frac{u}{\tau_p}\frac{\partial g}{\partial N}N_p \simeq N_p \tag{4.8a}
\end{aligned}
$$

$$
\begin{aligned}
\gamma &= \Xi_{NN} + \Xi_{PP} = u\frac{\partial g}{\partial N}\left[1 + \Gamma\frac{\partial g/\partial N_p}{\partial g/\partial N}\right]N_p + \frac{1}{\tau_{\Delta N}} + \frac{\Gamma R'_{sp}}{N_p} \\
&\approx \tau_p\omega_R^2\left[1 + \Gamma\frac{\partial g/\partial N_p}{\partial g/\partial N}\right] + \left[\frac{1}{\tau_{\Delta N}} + \frac{\Gamma R'_{sp}}{N_p}\right] \equiv K\left(\frac{\omega_R}{2\pi}\right)^2 + \gamma_0 \quad . \tag{4.8b}
\end{aligned}
$$

Above threshold, the first term in (4.8b) dominates so that the relaxation reso-
nance frequency runs linearly with the square root of the optical output power
$A_0 \simeq N_p$ which is proportional to the photon density N_p. Using this approxima-
tion, the damping rate γ runs linearly with the square of the relaxation resonance
frequency.

As the relaxation resonance frequency is increased by driving the laser at higher
output power, the frequency response becomes flatter due to the parabolic de-
pendence of the damping rate on ω_R. For large damping factors, the signal drops
below the 3 dB cutoff at smaller frequencies than ω_R so that a maximum achiev-
able bandwidth exists. One can define a damping-limited maximum intrinsic
bandwidth $\omega_{3dB}^{damping}$ and a thermally limited modulation bandwidth $\omega_{3dB}^{thermal}$ as
follows:

$$
\omega_{3dB}^{damping} = \frac{2\pi\sqrt{2}}{K} \tag{4.9}
$$

$$
\omega_{3dB}^{themal} = \omega_R\sqrt{1 + \sqrt{2}} \quad . \tag{4.10}
$$

The intensity noise is recorded under several bias conditions that correspond to
a series of optical output powers. The location of the relaxation resonances ω_R
and corresponding damping factors γ are extracted from the frequency responses
under these different bias conditions.

Fig. 4.8(b) displays the damping rate γ as a function of the square of the re-
laxation resonance frequency. The K-factor defined in eqn. (4.8b) is extracted
after a linear curve fit and is found to be approximately 0.1 ns. The maximum
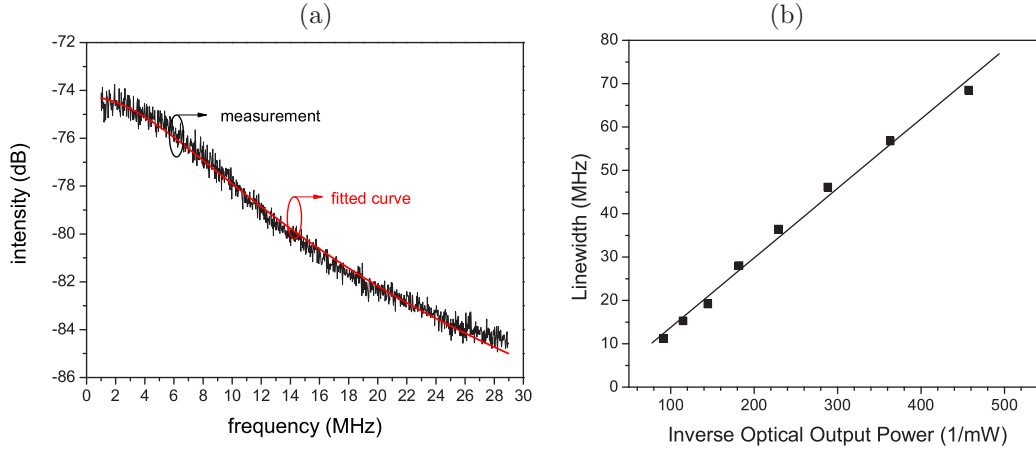
Figure 4.9: (a) Linewidth measurement (b) Shift of linewidth as a function of inverse optical output power A_0^{-1}.

intrinsic bandwidth is therefore given by $\omega_{3dB}^{damping}$=89 GHz.

Fig. 4.8(c) shows the shift of the relaxation resonance peak as a function of the square root of the optical output power. As can be expected, the relaxation shifts linearly and its slope D is approximately 13.5 GHz mW$^{-1/2}$. A saturation of the relaxation resonance frequency could be observed above 7 GHz so that the thermally limited modulation bandwidth is given by $\omega_{3dB}^{thermal}$=11 GHz. Clearly, in this laser design, the thermal contribution presents the major limitation to the maximum achievable bandwidth.

 Secondly, using the self-homodyne method, also explained in Appendix C.2, the laser's full width at half maximum was measured to be in the range of 7 to 8 MHz which represents a typical value for a single mode semiconductor laser (Figure 4.9(a)). The linewidth was furthermore measured for a series of different bias conditions as above, corresponding to different optical output powers. Figure 4.9(b) shows the measured linewidth as a function of the inverse optical output power. The linewidth is inversely proportional to the photon density which can be understood considering the fact that the contribution of spontaneous emission events to the total output power is reducing linearly above threshold[3].

---

[3]Spontaneous emission events are producing fluctuations in both amplitude and phase of the emitted electromagnetic radiation. The phase noise translates into the finite laser linewidth. Since above threshold, the spontaneous emission rate remains constant whereas the rate of stim-
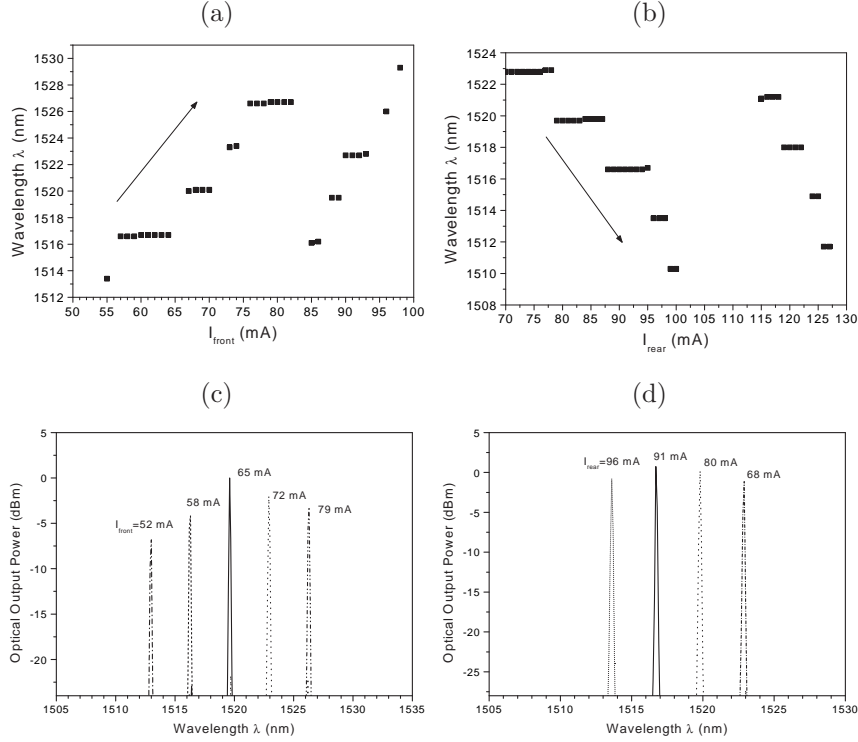
Figure 4.10: (a) A red shift of the lasing wavelength can be observed as the current into the front resonator is increased. The current into the rear resonator is kept constant at 40 mA. (b) A blue shift of the lasing wavelength can be observed as the current into the rear resonator is increased. The current into the front resonator is kept constant at 40 mA. (c) 5 superimposed spectra displaying a 3.3 nm mode gap of the rear resonator BSG lattice. The current into the rear resonator is kept constant at 40 mA. (d) 4 superimposed spectra displaying a 3.1 nm mode gap as defined by the front resonator BSG lattice. The current into the front resonator is kept constant at 40 mA.

This value could be reduced using frequency-dependent optical feedback [Mah1998], for example from an external resonator with high finesse [Shevy1999]. Another approach of reducing the phase noise is to use electronic feedback from circuitry calculating the frequency deviation error signal which is then fed back into the drive current of the laser diode to stabilize the feedback phase. Some proposals employ a combination of optical and electronic feedback control schemes [Shevy1993]. Many of these approaches can also be used to reduce the amplitude

---

ulated emission increases linearly, both the amplitude and phase noise decrease with increased optical output power A_0.
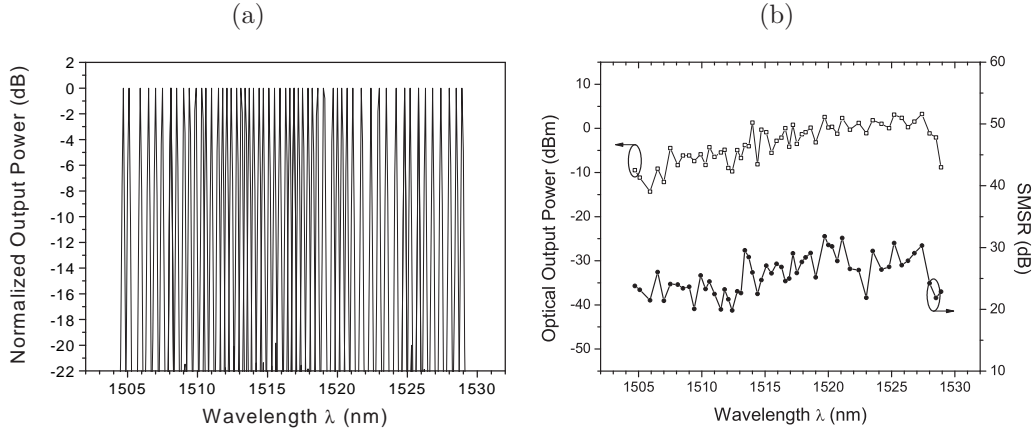
Figure 4.11: (a) Superimposed spectra displaying a tuning range of 24.5 nm with 56 channels (b) Optical output power and side mode suppression ratio (SMSR) over tuning range.

noise leading to a flattened RIN curve with a less prominent relaxation resonance peak [Hun1998, Mor1999, Ber2002].

Switching behavior

If the current into one of the two resonators is kept constant and the current into the second resonator is changed, a course tuning behavior can be observed due to the Vernier effect. Changing the current in the front resonator and leaving the current in the rear resonator constant at 40 mA for example changes the lasing wavelength towards higher wavelengths in steps of 3.3 nm as defined by the BSG grating in the rear resonator (Fig. 4.10(a)). As the current is further increased, the wavelength switches back to smaller wavelengths and upon a further increase the red shift can be observed again, leading to a cyclical switching behavior. Changing the current in the rear resonator and keeping the current into the front resonator at 40 mA similarly changes the lasing wavelength cyclically towards smaller wavelengths in steps of 3.1 nm as defined by the BSG grating in the front resonator (Fig. 4.10(b)).

 Fig. 4.10(c) and Fig. 4.10(d) show the measured emission spectra for the various tuning currents shown in Fig. 4.10(a) and Fig. 4.10(b).
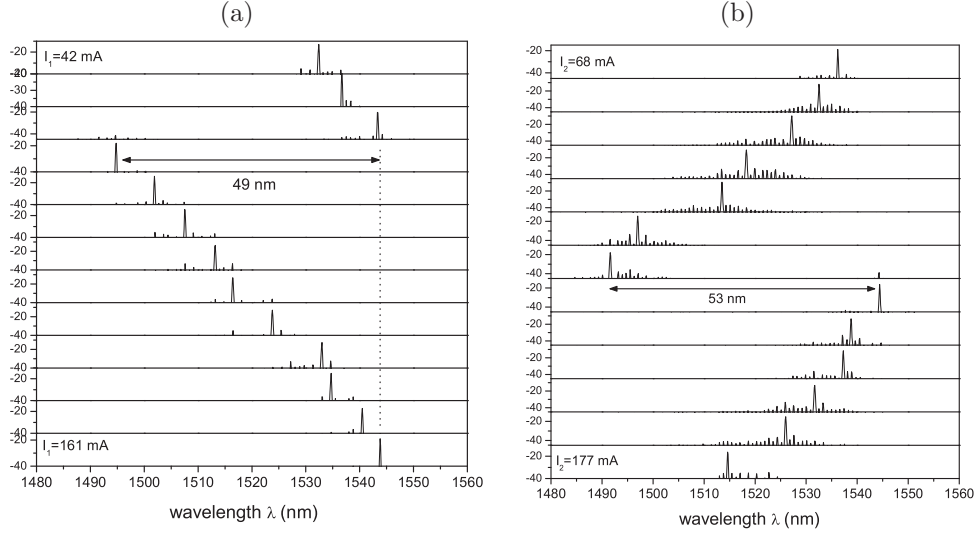
Figure 4.12: Measured emission spectra (a) for a series of segment-1 biases with segment-2 bias
fixed at 90 mA. A red shift of the emission wavelength can be observed over a tuning range of
49 nm. (b) for a series of segment-2 biases with segment-1 bias fixed at 90 mA. Laser emission
exhibits discontinuous wavelength shifts towards smaller wavelengths over a spectral range of
53 nm.

Tuning range

Through a combination of the above described switching behavior and a temper-
ature controlled continuous tuning, one can tune this device quasi-continuously
over a spectral range of 24.5 nm, corresponding to a channel spacing as typically
required for 56 channels in WDM applications as displayed in Fig. 4.11(a). Fig.
4.11(b) shows the output power and side mode suppression ratio over the tuning
range of the laser. The optical output power varies by about 10-15 dB while the
side mode suppression ratio is in the range of 20 to 32 dB. The decrease of output
power at small wavelengths follows the gain profile, the side mode suppression is
changing accordingly. The sudden drop of output power at large wavelengths is
believed to be due to a poor definition of these longitudinal modes as a result of
deficiencies during the grating fabrication.

Discontinuous tuning ranges of up to 50 nm have been realized with similar
designs as displayed in Figures 4.12(a) and 4.12(b). The side mode suppres-
sion ratios for these devices however dropped significantly upon fine tuning the
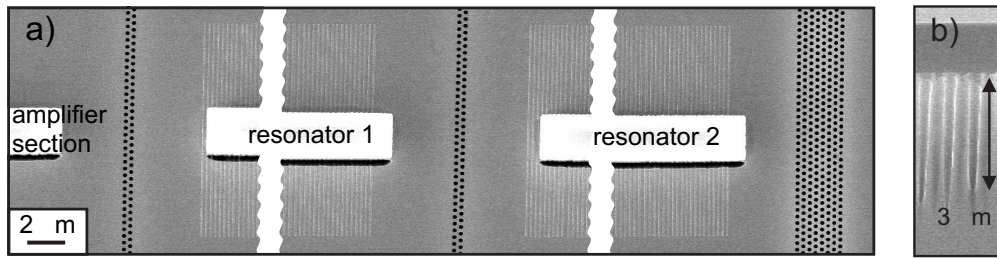
Figure 4.13: (a) Scanning electron microscopy graphs of the device with (from left to right): amplifier section, intracavity coupling section, gain segment 1 with lateral binary superimposed grating, intracavity coupling section, gain segment 2 and rear photonic crystal mirror section. (b) cross sectional view of photonic crystal section.

emission wavelength.

Post-amplification

Another very important requirement for tunable laser sources is the stability of their output power over their full tuning range, a demand that is often not met. In an ideal situation, the output power is stabilized such that one set of currents controls the emission wavelength and a second set of currents controls the output power without any significant spectral impact.

Therefore, as a more refined design, a coupled-cavity tunable laser design with photonic crystal coupling sections and rear reflectors is investigated that monolithically integrates an amplifier section.

Figs. 4.13(a) and (b) show scanning electron microscopy graphs of the laser structure. The design is based on the tunable laser design discussed in the previous section. Its single mode output is subsequently amplified by a third ridge waveguide amplifier section. Two amplifier designs have been investigated: one having a length of 25 μm and being untilted, the second having a length of 150 μm and being bent by 10 degrees against the normal of the output facet in order to reduce reflections back into the laser cavity.

Variation of the intracavity PhC lattice parameters allows one to engineer the intracavity coupling properties which can be used to further reduce the feedback from the amplifier section back into the laser cavity.

The devices were measured in continuous wave (cw) operation throughout the measurements. Fig. 4.14(a) shows the measured emission wavelengths and side
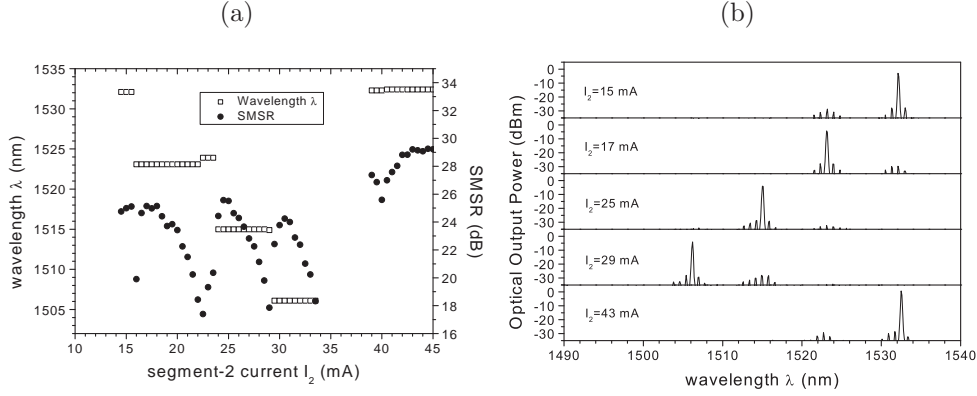
Figure 4.14: (a) Side mode suppression ratio (SMSR) and emission wavelengths (for SMSR
> 2 dB) as a function of resonator-2 current. A blueshift of the lasing wavelength can be
observed as the current into resonator 2 is increased. The gain segment 1 and amplifier section
currents are kept constant at 90 mA and 5 mA, respectively. (b) Emission spectra displaying
discontinuous mode jumps of 9 nm as defined by the BSG lattice of resonator 1. Resonator
currents as in subfigure (a).

mode suppression ratios against the resonator-2 drive current for the design with
untilted amplifier section and mode spacings of 9 nm and 10 nm for the two
resonators, respectively. As the current is increased from 0 mA to 40 mA, the
emission wavelength exhibits discontinuous jumps towards smaller wavelengths
in steps defined by the spectral positions of the longitudinal modes of resonator
1. A further increase of the resonator-2 current switches the wavelength back to
large values. Upon a further increase the blue shift can be observed again, lead-
ing to a cyclical switching behavior. The side mode suppression ratio exhibits
a periodic variation with its highest values of 26 to 30 dB being reached upon
optimum overlap between two cavity modes (Fig. 4.14(a)).

Figure 4.14(b) shows the emission spectra for the various tuning currents shown
in Figure 4.14(a). The emission wavelengths of the device can be switched over a
range of 26 nm. Similarly to the design without an amplifier section, a simultane-
ous increase of the resonator currents bridges the gaps between the discontinuous
mode spacings.

Fig. 4.2 shows the output power at four different operating points of the laser.
For this design, the amplifier section is bent by ten degrees against the normal
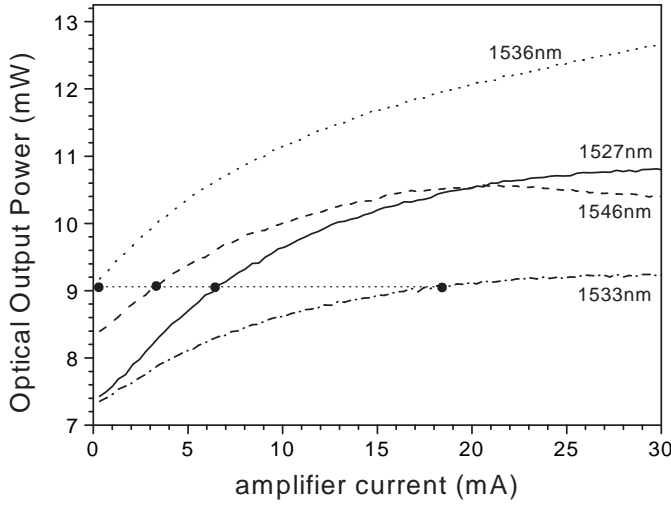
Figure 4.15: Signal amplification for four different operating points at 1536 nm (I_1=66 mA), 1527 nm (I_1=40 mA), 1546 nm (I_1=154 mA), and 1533 nm (I_1=24 mA). The current into resonator 2 is kept constant at 76 mA.

of the output facet. Keeping the resonator-2 current constant at 76 mA and setting the resonator-1 currents at 24 mA, 40 mA, 66 mA, and 154 mA yields laser emission at the wavelengths depicted in Fig. 4.2. Keeping the resonator-1 and 2 currents constant and increasing the amplifier current from 0 to 30 mA increases the signal output power while keeping the mode unchanged. Through adjustment of the amplifier current, here 0 mA, 3.1 mA, 6.5 mA, and 18.1 mA respectively, the output power can be stabilized to be 9 mW throughout the laser tuning range. The four marks indicate possible operation points for the selected modes. Due to the reduced feedback from the amplifier section into the laser cavity, the wavelength experiences only a moderate, thermally induced red shift of 0.1 nm with no changes in mode order or mode jumps being present.

Chapter 5

Operation of 2D PhC in the bandgap: Waveguides

5.1 Line Defects in a photonic crystal block

A point defect in an otherwise regular 2D PhC lattice is generated by either adding or removing dielectric material at one of the lattice locations. Adding dielectric media to an otherwise regular two-dimensional crystal block made of rods of air in the dielectric is called a 'donor'-type defect whereas removing dielectric media by increasing the rod radius is referred to as an 'acceptor'-type defect. This nomenclature is chosen considering the analogy to defects in an electronic band structure as discussed in chapter 3.2.3 where the electric potential at the location of the defect is either locally decreased or increased.

The additional medium allows the existence of a doubly degenerate defect mode that is spatially confined to the position of the defect. In the dispersion diagram, the mode will live inside the photonic bandgap as shown in Figure 5.1(a). As the mode is spatially confined in the defect, it keeps its energy value for all wave numbers. The mode's field distribution resembles that of a dipole.

If adding a second such defect at some distance ξ, which is a multiple of lattice constants, a second set of modes can exist inside the photonic bandgap. If ξ is sufficiently small, the two sets of modes can couple as described in chapter 3.2.3 and the degeneracy of the single defect is lifted. The configuration can in many ways be related to the description of a diatomic molecule or coupled quantum dots. The smaller the distance ξ between the two defects, the more their four energy levels will repel.

Extending the defects to a chain of regularly spaced defects allows a coupling of modes of the same symmetry from one defect cavity to its neighbor and so on. As
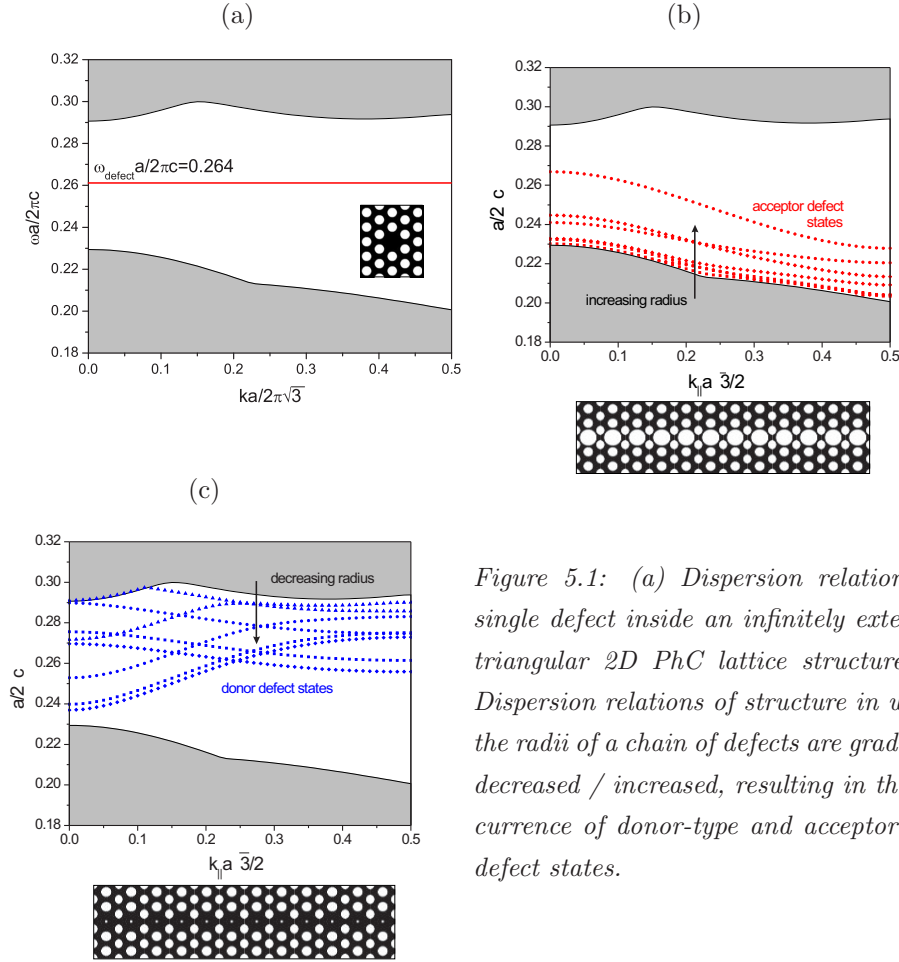
(a)

(b)

(c)

Figure 5.1: (a) Dispersion relations of single defect inside an infinitely extended triangular 2D PhC lattice structure (b) Dispersion relations of structure in which the radii of a chain of defects are gradually decreased / increased, resulting in the occurrence of donor-type and acceptor-type defect states.

a result a waveguide of coupled resonators is formed, hence referred to as coupled resonator optical waveguide (CROW) [Yariv1999] or coupled-cavity waveguide (CCW) [Bay2000]. It very clearly illustrates the nature of the waveguide: the defect states introduced through the defects in the PhC lattice can couple to one another, thus facilitating a guiding of the light from one end of the chain to the other.

The physical nature of the coupled resonator optical waveguide can be appreciated, when slowly 'turning on' the chain of defects as illustrated in Figure 5.1(b) and (c). As the radii of a series of lattice positions is slowly decreased from the initial radius of the regular lattice to infinitely small radii, modes from the air band can reduce their energy by redistributing their fields into the positions of the defects. Similar to the situation of the single defect where a single donor defect state is generated, now a chain of donor defect states is generated that

can serve as a waveguide along which light is allowed to propagate (blue lines). Similarly, increasing the radii along a series of lattice positions forces modes of the dielectric band to have field components in the air rods. As a consequence, their eigenenergies increase to generate a chain of acceptor-type defect modes in the photonic bandgap (red lines). Since the acceptor modes have a larger field component in the air rods compared to the donor defects modes whose fields are located predominantly in the locations of the added dielectric, throughout this work, exclusively donor-type waveguide structures will be investigated since the acceptor modes are inherently lossy due to the weak vertical photon confinement in the planar waveguide structure in combination with the finiteness of the vertically defined structures.

Figure 5.2(a) shows the dispersion relations of a donor-type defect waveguide whose defect radii have been reduced to zero and which is embedded in a photonic crystal block in Γ-M orientation. The bandgap is bridged by two allowed modes representing the symmetric and antisymmetric states existing in the defects. This type of waveguide is referred to as W1 waveguide. Light propagation can occur on either mode. One set of modes is predominantly located in the air cylinders whereas the other is predominantly located in the dielectric material: at the sides of Figure 5.2(a) the spatial field distributions of the z-component of the magnetic field are displayed as color surface plots.

Depending on the distance ξ between two defects within the chain, the modes will couple more or less fast from one defect to its neighbor. It is therefore possible to control the group velocity of light propagating in such a waveguide through the spacing of the defects. A reduction of group velocity by a factor of 100 has already been demonstrated for a 2D PhC [Not2001]. Further reductions based on 2D PhC's will be difficult to implement since the wider the spacing of defects, the more light will leak into air modes so that an effective waveguiding is prohibited. If integrating such a line of distant defects in a 3D PhC however, the light is prohibited from propagating into the vertical direction so that CROW's of even further reduced group velocity can be engineered.

 Adding a line of defects adjacent to the original line of defects will allow modes that previously existed in the airband to reduce their energy and shift into the bandgap region. The additional high index material effectively 'pulls' more modes
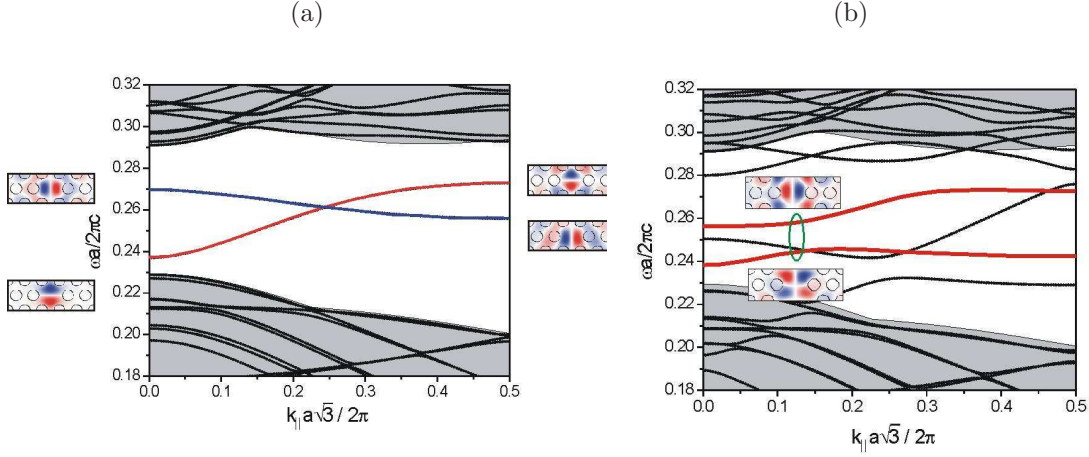
Figure 5.2: (a)Dispersion relations of first eight modes of a W1 line defect in a photonic crystal block in Γ-K orientation. The maps on each side show the distribution of the z-component of the magnetic field at selected k-vectors. The gray shaded areas display the dielectric and air band of the monolithic photonic crystal block without defects. (b)Dispersion relations of W3 channel waveguide in Γ-K orientation for TE-polarized light. The maps on each side show the distribution of the z-component of the magnetic field at selected k-vectors. The gray shaded areas display the dielectric and air band of the monolithic photonic crystal block without defects.

from the airband into the initial band gap in accordance to the variational principle. Adding an odd number of defect lines will result in symmetric waveguides whereas adding an even number of lines will result in asymmetric waveguides. Extending the defect line to 5, 7, or 9 rows increases the number of allowed light paths exponentially. Figure 5.2(b) shows the dispersion relations for the example of a W3 PhC channel waveguide in Γ-M orientation.

Extensive research has been undertaken to reduce the losses in these Wn photonic crystal waveguides typically realized in Γ-K orientation of the photonic crystal to facilitate the use of these waveguides as interconnects between other photonic crystal building blocks to ultimately form an integrated photonic circuit. Despite significant improvements in the reduction of losses, the question recently becomes increasingly obvious whether this type of waveguide would be in any case suitable for the use as an interconnect. The fundamental problem of this type of waveguide is the interaction of the lightwave with the periodically modulated waveguide boundary that results in a reduction of the group velocity, and there-

fore a significant reduction in the bandwidth of the interconnect (particularly for membrane-like structures due to coupling onto modes above the light cone). An ideal interconnect is one with no dispersion, a wide bandwidth, and sufficiently low losses. Very recently, it has been suggested therefore to embed a classical high index contrast waveguide whose dispersion has been matched with that of the surrounding photonic crystal bulk material and fine tuned with respect to the air gap between the ridge and the photonic crystal surrounding [Fan2002]. Despite its possible disadvantages for the use as interconnects, the inherent dispersive nature of this type of waveguide can be used for a waveguide with in-situ chromatic dispersion compensation (signal regeneration), or for an optical delay line. In combination with other structures such as ring resonators and adjacent waveguides, the photonic crystal waveguides can help to build very compact add-drop filter structures and therefore contribute to a dramatic miniaturization of many optical components.

Although single mode photonic crystal waveguides can be expected to exhibit the lowest losses when forming sharp bends and reduce modal dispersion, until today the limitations faced by fabricational tolerances result in two major drawbacks that are interrelated:

- The surface roughness of the etched air cylinders results in very significant out-of-plane scattering losses, the most important loss mechanism in PhC channel waveguides. Compared to multimode photonic crystal channel waveguides, this effect becomes particularly disadvantageous in straight waveguide sections.

- A second problem arises when investigating active devices: the efficiency of injecting carriers into a W1 photonic crystal waveguide due to surface recombinations is too low to consider this narrow waveguide as an effective resonator. The surface roughness that initially gave rise to increased out-of-plane scattering losses also results in an increase in the number of surface states, therefore additionally decreasing the injection efficiency.

As a result, with today's fabricational limitations it is not possible to design a W1 laser resonator that can be brought above threshold when pumped electrically. The approach that is taken for the designs investigated here is to use multimode
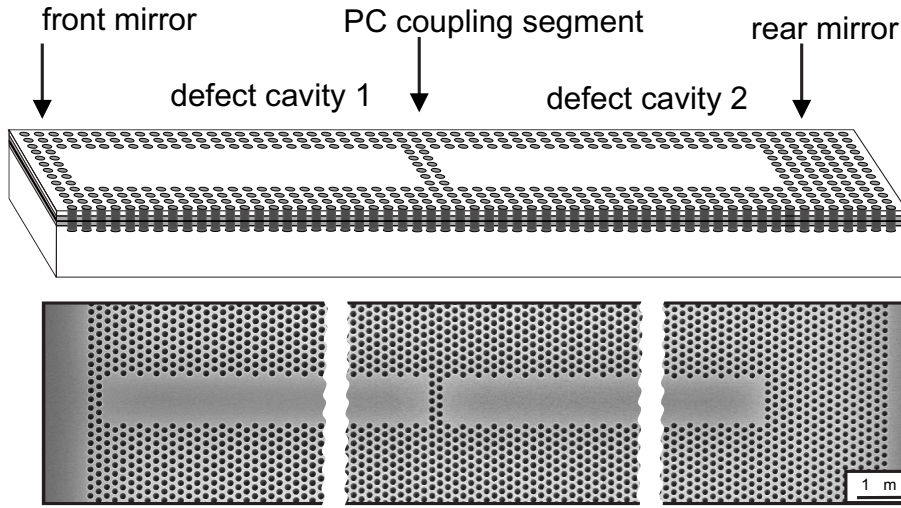
Figure 5.3: Top: Schematic of the photonic crystal coupled-cavity laser structure. Bottom: Scanning electron microscopy pictures of top view of the laser structure with (from right to left): rear photonic crystal mirror, rear photonic crystal waveguide, intra-cavity coupling section, front waveguide, and photonic crystal front reflector. The two cavities are 70 μm and 76 μm long, respectively.

waveguides Wn (n=7, 9, 11), thus facilitating reasonable current injection efficiencies and waveguide losses. The increased problems when forming sharp bends using multimode waveguides will be addressed in chapter 5.3.

5.2 Application to tunable photonic crystal coupled-cavity laser

The design is based on the contra-directional coupling of two photonic crystal channel waveguides which are contacted independently. The waveguides are based on n (n=7, 9, or 11) missing rows of air holes oriented along the Γ-M direction of the photonic crystal. They are referred to as Wn waveguides throughout this work. It is worth noting that with n being chosen as odd numbers, the channel waveguide becomes symmetric along the mirror plane in the center of the waveguide which would not be the case if n were chosen to be even.

The device is based on the epitaxial layer system A52406 described in Appendix D. The waveguides are coupled through a photonic crystal section of one lattice

period in Γ-M direction. The lattice period of 380 nm and air fill factor of 30% are chosen such that the laser emission lies in the center of the photonic bandgap. The length of the front cavity extends over 107 periods or L_{front}=107a$\sqrt{3}$ =70 μm whereas the rear cavity extends over a length of 115 periods or L_{rear}=115a$\sqrt{3}$ =76 μm. The rear facet consists of a highly reflective photonic crystal mirror section that extends over 8 lattice periods and has a reflectivity near unity. The front facet has been cleaved. Fig. 5.3 shows a schematic as well as scanning electron microscopy graphs of the design. For comparison, designs with photonic crystal lattice periods of a=400 nm and resonator lengths of 114 μm/ 124 μm have been realized.

Device processing

The fabrication is schematically illustrated in Figure 5.4(a) through (h). In a first step, an area of about 1 cm^2 is cleaved from the 4 inch diameter wafer. The sample surface is organically cleaned and a 200 nm thick SiO$_2$ mask is sputtered onto the sample followed by a 500 nm thick polymethylmethacrylate (PMMA) resist layer. A photonic crystal pattern is defined in the resist using electron beam lithography (600 pA, dose 600 μC/cm^2) as illustrated in Figure 5.4(a). The sample is developed for about one minute. The pattern is subsequently transferred into the SiO$_2$ mask using a CHF$_3$ /Ar based dry etch process [Figure 5.4(b)] and finally etched around 3 μm into the semiconductor using a highly anisotropic Cl$_2$ /Ar based electron cyclotron resonance reactive ion etching process as illustrated in Fig. 5.4(c). Lattice periods of 360 nm and air fill factors of 33% lead again to the desired reflectivities of about 65%. The dimensions have been chosen such that the lasing wavelength of about 1550 nm lies in the center of the photonic bandgap. The rear facet consists of a highly reflective photonic crystal mirror segment with 4 lattice periods of the same dimensions resulting in reflectivities near unity.

In order to improve the current injection efficiency, apertures are defined above the photonic crystal waveguides. The apertures are defined in 500 nm PMMA using electron beam lithography (current 2 nA, dose 650 μC/cm^2) and the sample is developed for one minute. An etch mask of 40 nm thick BaF$_2$ is evaporated onto the sample by electron beam evaporation with the unexposed mask areas
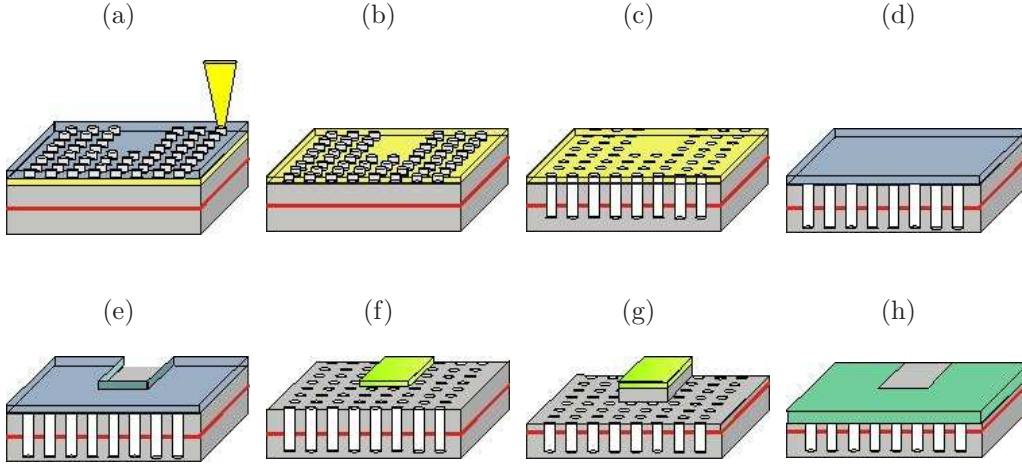
Figure 5.4: Process steps for the fabrication of the tunable photonic crystal coupled-cavity laser design.

being removed by lift-off. Dry etching of the areas surrounding the waveguides selectively removes the highly conductive top layer of the structure to improve current injection. Finally the devices are planarized and contacted.

Switching principle

The number of longitudinal modes propagating in each of the two photonic crystal waveguides, henceforth denoted as s={front,rear}, is determined by the length L_s of the respective resonator. For constructive interference between the two confining resonator ends, $4\pi n'_s L_s/\lambda = m_s\, 2\pi$ relates the mode frequencies to the resonator length L_s with m_s denoting the mode number. Considering material dispersion, the resulting mode comb in resonator s features mode spacings of

$$\Delta\Lambda_s = \frac{\lambda/2L_s}{(dn'_s/d\lambda) - (n'_s/\lambda)} \ . \tag{5.1}$$

Considering both carrier transport and heating effects, the wavelength shift of the resonator's longitudinal mode spacings is again obtained from (4.3). Fig. 5.2 displays the calculated wavelength shift as a function of segment bias along with its carrier and thermal contributions. The wavelength initially experiences
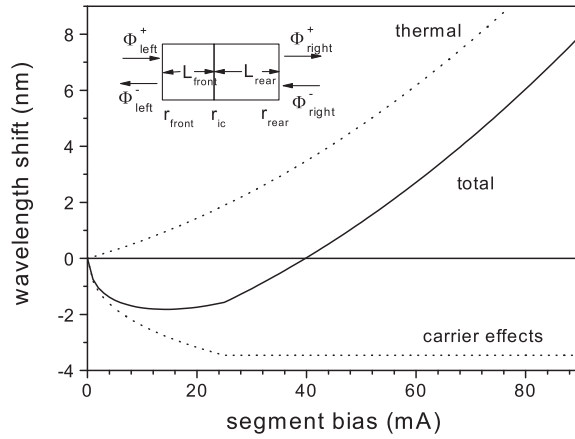
Figure 5.5: (a) Model of wavelength change with injected resonator current: carrier transport effect, temperature effect, and net wavelength change. Inset: Definition of the mirror reflectivities confining the two coupled resonators.

a blue shift of about 2 nm due to the above mentioned carrier effects. Due to the clamping above threshold, the thermally induced red shift begins to dominate the carrier induced blue shift so that the mode comb experiences an overall red shift. The discontinuity in the derivative of the wavelength shift for the carrier contribution occurs due to the assumption of carrier density clamping for resonator currents above threshold. Table 5.1 displays the parameters used for this calculation. The large thermal resistance can be understood considering the poor thermal conductivity between the device and the heat sink and the fact that the device is not thinned and mounted.

The switching principle is again based on the Vernier effect. In this design, however, the limited spectral width of the gain spectrum (rather than the finite number of longitudinal modes from the grating) means that only one of the periodic overlaps is supported by the material gain resulting in single mode emission. A continuous shift of one mode spectrum relative the other leads to a cyclical overlap between the two mode combs, resulting in a cyclical wavelength switching. The carrier-induced initial blue shift of the longitudinal mode spectrum is reflected in an initial reverse shift of the emission wavelength (red upon varying front segment bias, blue upon varying rear segment bias). This effect could not be observed for the design with gain-coupled distributed feedback due to the higher cavity losses introduced by the lateral metal grating structure: while the longitudinal modes shift blue at small pump rates, the laser has not yet reached threshold so that the carrier induced blue shift cannot be observed.

Symbol	Parameter	Value
A	non-radiative recombination coefficient	1×10^8 1/s
B	radiative recombination coefficient	8×10^{-17} m^3/s
C	Auger recombination coefficient	5×10^{-41} m^6/s
V	volume of active region	2×10^{-17} m^3
η_i	injection efficiency	0.7
η_{tot}	total quantum efficiency $(I \geq I_s^{th})$	0.025
R_T	thermal resistance	650 K/W
R_d	differential resistance	13 Ω
V_j	junction voltage	0.9 V
$\frac{\partial \lambda}{\partial n'} \frac{\partial n'}{\partial N}$	ratio of wavelength change due to carrier effects	8.3×10^{-25} nm m^3
$\frac{\partial \lambda}{\partial n'} \frac{\partial n'}{\partial T}$	ratio of wavelength change due to thermal effect	0.095 nm/K
L_1	length of resonator 1	70 (114) μm
L_2	length of resonator 2	76 (124) μm
r_1	front facet reflectivity	0.67
r_2	rear facet reflectivity	0.99
r_{12}	intra-cavity coupling section reflectivity	0.67

Table 5.1: Material and device parameters used for calculation.

P-I and U-I characteristics

Figure 5.6(a) shows the output power characteristics of three 114μm/ 124μm long devices with 7, 9, and 11 missing rows, respectively. Upon increasing the channel waveguide width, the threshold is decreasing from 19 mA (W7) to 13 mA (W11) and the external quantum efficiency is increasing from 25 mW/A (W7) to 48 mW/A (W11). The differential resistance at threshold is approximately 13 Ω and the junction voltage is around 0.9 V for all three coupled waveguide structures. Maximum output powers range between 1.5 mW (W7) and 3 mW (W11). For comparison, a tunable photonic crystal coupled-cavity laser based on W5 waveguides exhibits thresholds > 70 mA, thermal rollover at about 120 mA, and output powers in the range of 0.02 mW.

The depreciation in output power and external quantum efficiency, accompanied by the increase in threshold currents can be explained by increasing waveguide losses as a result of the increased overlap between the fundamental mode and the waveguide boundary. Secondly, the injection efficiency decreases significantly as the waveguide width is reduced.
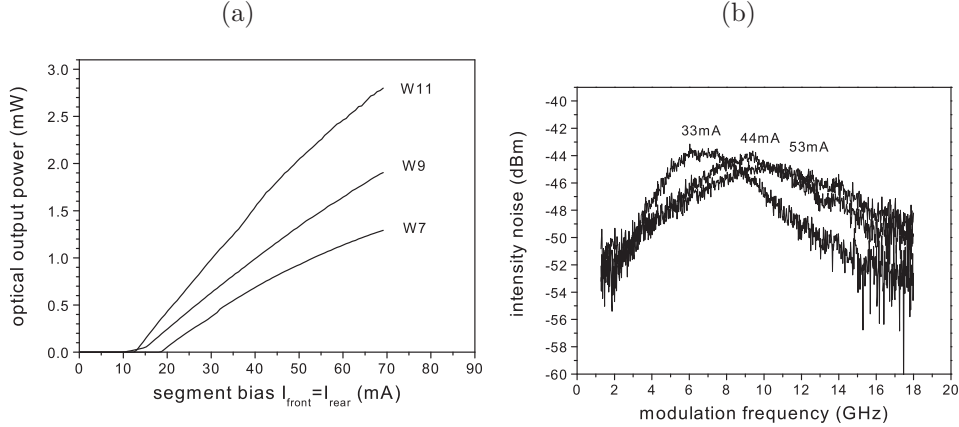
Figure 5.6: (a) Measured output power characteristics of 114/124 µm long device. Widths are W7, W9, and W11 respectively (b) Measurement of intensity noise

Dynamic device properties

Figure 5.6(b) displays the intensity noise spectra under different bias conditions for a design with a 114 µm long rear and a 124 µm long front resonator. The drive current into the rear resonator is kept unchanged at 20 mA, whereas the front current is selected to be 33 mA, 44 mA, and 53 mA. Fitting the data with the non-linear curve fit of (4.7), one obtains a maximum resonance frequency of 11.1 GHz for a front resonator drive current of 53 mA. In an analysis equivalent to the one described in chapter 4.2, the K-factor is found to be 0.23 ns, the D-factor is found to be 5.8 GHz mW$^{-1/2}$, leading to a damping limited modulation bandwidth of $\omega_{3dB}^{damping} = 2\pi\sqrt{2}/K$=39 GHz and a thermally limited modulation bandwidth of $\omega_{3dB}^{thermal} = \omega_R\sqrt{1+\sqrt{2}}$=17 GHz. Compared to the lasers with complex-coupled distributed feedback, the damping contribution is increased which can be understood considering the stronger confinement of the fundamental mode by the periodically corrugated waveguide boundary.

Injecting a current of 8 mA in the front resonator and 49 mA in the rear resonator which results in laser emission at 1485 nm at a power of -21 dBm (collected by the single mode fiber), the linewidth was measured to be 15.3 MHz. The value is about twice that of the laser design with gain-coupled distributed feedback which can be easily understood considering the fact that the design with gain-coupled distributed feedback has significantly larger resonator lengths and therefore larger
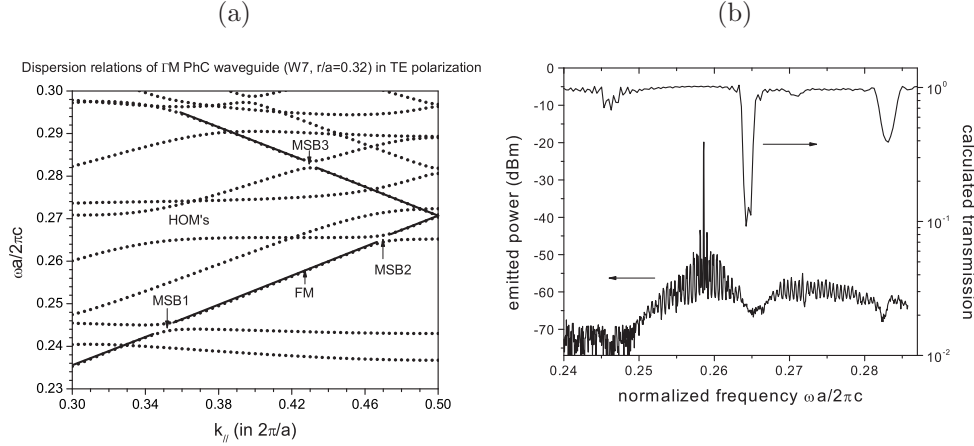
Figure 5.7: Mini-stopbands (MSB) of a photonic crystal channel waveguide in Γ-M orientation (W7). (a) Dispersion relations of PhC channel waveguide (W7) in TE polarization exhibiting three anti-crossings in the relevant normalized frequency window. (b) Measured spectrum of coupled-cavity laser design (W7) and finite difference time domain calculation of W7 waveguide structure.

gain leading to higher output powers. Comparing this linewidth with that of the gain-coupled distributed feedback laser operated at bias conditions that result in a comparable output power (as given in Figure 4.9(b)), one can see that the power-corrected linewidths of the two designs are equivalent.

Mini-stopbands and coupled-mode analysis

One characteristic specific to the propagation of light in a photonic crystal channel waveguide is that their transmission spectra exhibit regions of prohibited propagation, the so called mini-stopbands. They are the result of off-diagonal couplings between the dispersion curves of higher order modes (HOM) and the fundamental mode (FM) propagating in the waveguide. The energy separation is proportional to the coupling strength between the two states and can be motivated by an electromagnetic equivalent to the quantum mechanical non-crossing theorem. One can also explain the formation of the avoided crossing points employing the electromagnetic equivalent to the quantum mechanical variational theorem. Any mode will seek to minimize its energy while remaining orthogonal to its lower modes. Since the lowest energy eigenmode tends to concentrate

in regions with low dielectric constant to minimize its energy, the next higher eigenmode will be forced to be orthogonal across the same region, leading to an energy separation.

Fig. 5.7(a) displays the dispersion relations for the case of a Γ-M photonic crystal channel waveguide (W7) in TE-polarization obtained from calculations based on a plane-wave expansion model. The symmetric fundamental mode (FM) is coupling with the symmetric HOM resulting in an anti-crossing of their respective dispersion curves. This anti-crossing results in spectral regions of reduced transmission which are also visible in the measured emission spectra. Fig. 5.7(b) displays a measured emission spectrum of a W7 tunable laser diode at front and rear currents set at 15 mA, i.e. just above threshold. The emission spectrum has been rescaled to a normalized frequency window from 0.240 to 0.287. Comparison between the spectral location of the avoided crossing points in the dispersion diagram and the locations of reduced transmission in the measured emission spectrum shows excellent agreement.

The position of the mini-stopbands as well as their spectral width can furthermore be well confirmed by means of a two-dimensional finite difference time domain calculation also displayed in Fig. 5.7(b). The limitation to a 2D analysis of this otherwise 3D structure is justified as the above described planar waveguide structure provides transverse photon confinement through weak index guiding. Although the lack of complete confinement in three dimensions results in necessary alterations to the model, it has been shown [Ben1999, Ben2000, Ol2001] that the corrections to the 2D model are moderate provided that the holes extend deeply into the cladding (see discussion of chapter 3.2.2) and the index contrast between the core and the cladding is ≤ 0.5[1]. It is found that deeply etched cylinders that satisfy these conditions can exhibit lower losses compared to high-index contrast configurations such as the membrane configuration. By appropriate choice of the photonic crystal lattice dimensions surrounding the waveguide, the spectral location of the mini-stopbands can be engineered to either prevent any potential competition between longitudinal modes or can be located such that its spectral positions do not overlap with the tuning range of the laser. This fact

---

[1]The 2D model is corrected through the introduction of an imaginary effective index inside the holes.

will be used later since consequently a discussion of the off-diagonal couplings of
the FM with HOM's within each waveguide can be separated from a discussion
of the coupling between the longitudinal modes in the coupled waveguides.

Apart from being folded multiple times at the boundary of the first Brillouin
zone, and its anti-crossing with the symmetric HOM's, the FM has the disper-
sion relation of light in bulk dielectric $\omega a/2\pi c = ka/2\pi n$ indicating that it is
mainly guided by the index contrast between the waveguide core and the average
index of the surrounding photonic crystal boundaries.

From the knowledge of the spectral width of a MSB, it is possible to extract in-
formation about the waveguide losses of the modes involved in the coupling that
led to the formation of the MSB provided the length of the waveguide is known.
Assuming harmonic time dependence, $E_{\mu,\nu}(x,\omega,t) = E_{\mu,\nu}(x,\omega)e^{-i\delta_{\mu,\nu}ct/n}$, one can
express the coupling of two modes μ and ν propagating along the x-direction of
a waveguide using the following coupled mode formulation:

$$
\frac{d}{dx}\begin{pmatrix} E_\mu(x,\omega) \\ E_\nu(x,\omega) \end{pmatrix} = \hat{T}\cdot\begin{pmatrix} E_\mu(x,\omega) \\ E_\nu(x,\omega) \end{pmatrix}
$$

$$
= \begin{pmatrix} \alpha_\mu - j\delta_\mu(\omega) & -j\kappa_{\mu\nu} \\ j\kappa_{\mu\nu} & -[\alpha_\nu - j\delta_\nu(\omega)] \end{pmatrix}\begin{pmatrix} E_\mu(x,\omega) \\ E_\nu(x,\omega) \end{pmatrix} \tag{5.2}
$$

in which $E_\mu(x,\omega)$ and $E_\nu(x,\omega)$ denote the field amplitudes of the forward propa-
gating mode μ (assumed to be the FM) and the counter-propagating HOM ν, and
$\delta_\mu(\omega)$ and $\delta_\nu(\omega)$ denote the detuning of the respective uncoupled modes from the
Bragg resonance which is assumed to run linearly with ω proximal to the avoided
crossing point centered at ω_0:

$$
\delta_\mu(\omega) = \frac{n_\mu}{c}(\omega_0 - \omega) \tag{5.3a}
$$

$$
\delta_\nu(\omega) = \frac{n_\nu}{c}(\omega_0 - \omega) \qquad . \tag{5.3b}
$$

$n_\mu = c/u_\mu$ and $n_\nu = c/u_\nu$ denote the group indices of modes μ and ν, respectively,
which are given by the group velocities u_μ and u_ν of the uncoupled modes, i.e. the
slopes of the dispersion relations of the uncoupled modes. The energy gap $\Delta\omega_{\mu\nu}$
of the avoided crossing is obtained after determining the eigenvalues of $\hat{T}$ and is
given by $\Delta\omega_{\mu\nu} = 4a\kappa_{\mu\nu}/[2\pi(n_\mu + n_\nu)]$. Both the group indices of the FM and
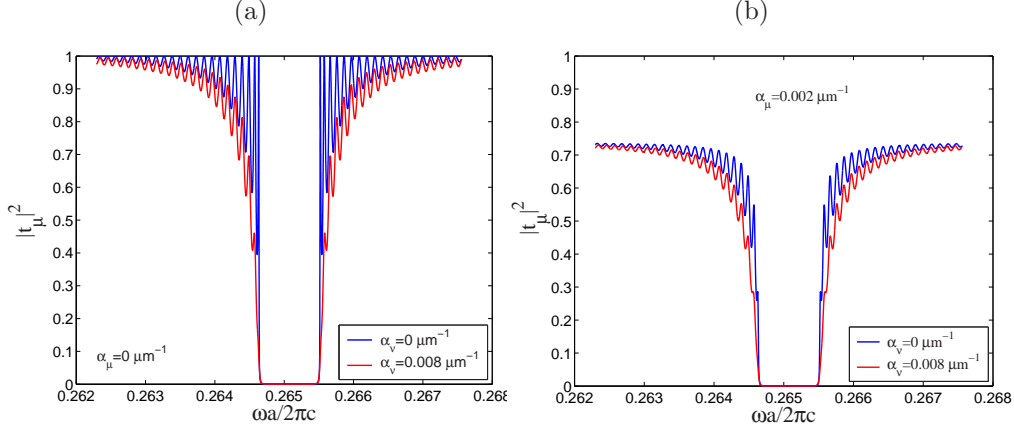the counter-propagating HOM can be determined from the dispersion relation.

Figure 5.8: Transmission spectra of fundamental mode μ for different mode losses. (a) blue line: $\alpha_\mu = \alpha_\nu = 0$, red line: $\alpha_\mu = 0$ and $\alpha_\nu = 0.008\ \mu m^{-1}$ (b) blue line: $\alpha_\mu = 0.002\ \mu m^{-1}$ and $\alpha_\nu = 0$, red line: $\alpha_\mu = 0.002\ \mu m^{-1}$ and $\alpha_\nu = 0.008\ \mu m^{-1}$

For the example of MSB2 from Fig. 5.7(a), the group indices and the energy gap are found to be $n_\mu = 3.3$, $n_\nu = 22$, and $\Delta\omega a/2\pi c = 1.57\cdot 10^{-3}$ so that the expected coupling constant from plane wave calculations is $\kappa_{\mu\nu} = 0.063\, a^{-1}$.

The solution of (5.2) is of the form

$$E_\mu = m_1 e^{\gamma x} + m_2 e^{-\gamma x} \tag{5.4a}$$

$$E_\nu = n_1 e^{\gamma x} + n_2 e^{-\gamma x} \quad . \tag{5.4b}$$

Plugging (5.4a and b) into (5.2) and imposing that light shall be incident from the left such that $E_\nu(L) = 0$, one finds the solutions of (5.2) to be

$$E_\mu = E_\mu(0)\frac{\gamma \cosh\gamma(x-L) + (\alpha_\mu - i\delta_\mu)\sinh\gamma(x-L)}{\gamma\cosh\gamma L - (\alpha_\mu - i\delta_\mu)\sinh\gamma L} \tag{5.5a}$$

$$E_\nu = iE_\mu(0)\frac{\kappa_{\mu\nu}\sinh\gamma(x-L)}{\gamma\cosh\gamma L - (\alpha_\nu - i\delta_\nu)\sinh\gamma L} \tag{5.5b}$$

with

$$\kappa_{\mu\nu}^2 = (\gamma - \alpha_a + i\delta_a)(\gamma + \alpha_b - i\delta_b). \tag{5.6}$$

The amplitude reflectivities and transmissivities of modes μ and ν are then immediately given by

$$r_{\mu,\nu} = \frac{E_{\nu,\mu}(0)}{E_{\mu,\nu}(0)} = \frac{-i\kappa_{\mu\nu}\sinh\gamma L}{\gamma\cosh\gamma L - (\alpha_{\mu,\nu} - i\delta_{\mu,\nu})\sinh\gamma L} \tag{5.7}$$

$$t_{\mu,\nu} = \frac{E_{\mu,\nu}(L)}{E_{\mu,\nu}(0)} = \frac{\gamma}{\gamma\cosh\gamma L - (\alpha_{\mu,\nu} - i\delta_{\mu,\nu})\sinh\gamma L} \tag{5.8}$$
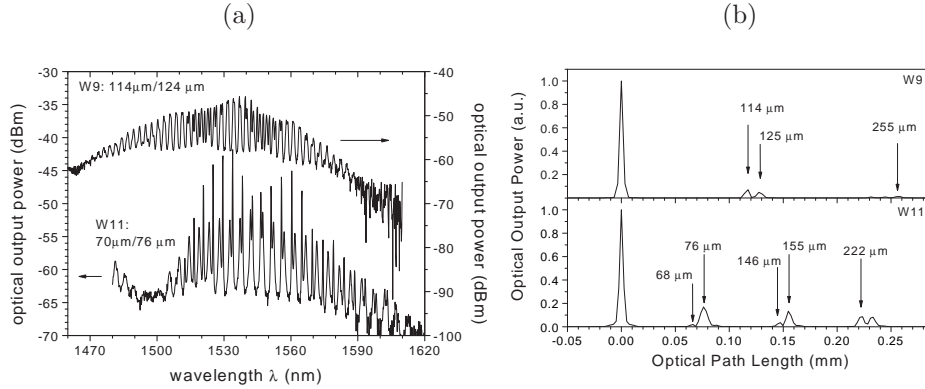
Figure 5.9: Subthreshold analysis of the two designs investigated. (a) Measured subthreshold spectra of 70/76 µm long coupled W11 channel waveguides with lattice periods of 400 nm and 114/124 µm long coupled W9 channel waveguides with lattice periods of 380nm. (b) Fourier transform of re-sampled power spectrum as a function of optical path length.

The transmissivity and reflectivity spectra of the FM and the counter-propagating HOM are then obtained by multiplication with the respective complex conjugates. Fig. 5.8(a) and (b) illustrate the different effect of the mode losses α_μ and α_ν on the transmission spectra $|t_{\mu,\nu}|^2$, here for the example of transmissivity of the FM μ. While an increase in α_ν results in a smoothening of the side lobes as shown in Fig. 5.8(a), an increase in the losses of the FM, results in an overall transmissivity reduction as illustrated in Fig. 5.8(b).

By adjusting the losses for the two modes to yield the best fit to the measured transmission spectrum (Fig. 5.7(b)), it is possible to reproduce the precise width of the observed MSB and therefore to reconstruct the propagation losses of both the FM and the respective HOM. For the example of MSB2 of Fig. 5.7(b), the best fit is obtained for α_μ=0.12 μm^{-1}, α_ν=0.4 μm^{-1}, and $\kappa_{\mu\nu}$=0.035a^{-1}. The coupling constant is lower than the value of 0.063a^{-1} from the plane wave expansion calculation, possibly due to a small width variation along the fabricated waveguide [Ol2003].

Subthreshold analysis

Fig. 5.9(a) shows subthreshold spectra of a 70 μm/ 76 μm long and 114 μm/ 124 μm long photonic crystal channel waveguide. Air fill factors in both cases are approximately 33%. As can be seen, the 114/ 124 μm long W9 photonic crystal waveguide exhibits no mini-stopbands in the relevant frequency window whereas the 70/ 76 μm long W11 photonic crystal waveguide exhibits a mini-stopbands centered around 1495 nm.

From the measured subthreshold spectrum we wish to derive information about the intracavity reflectivities. By translating the measured subthreshold spectrum $P(\lambda_j)$ into $k_j = 2\pi/\lambda_j$-space and re-sampling to $n(k_j)k_j$ spacing by linear interpolation, we obtain a new power spectrum with the same number of points in the spectrum as the originally measured spectrum $P(\lambda_j)$, now exhibiting equidistant peak spacing. $j = 1 \ldots N$ counts the number of points in the measured spectrum. After a standard Fourier transform of this re-sampled spectrum $P(n(k_j)k_j)$

$$P(m) = \frac{1}{N} \sum_{j=0}^{N} P(n(k_j)k_j) \exp{-2\pi i j m/(N-1)} \tag{5.9}$$

one obtains Fourier components $P(m)$ corresponding to a round trip time in the resonator of length $l(m)$ [Acker1998, Hofst1998]:

$$l(m) = \frac{m\pi}{n_0(k_N - k_1)} \tag{5.10}$$

with m being an integer counting the number of peaks across the spectrum.

Fig. 5.9(b) shows the result of this effort starting from the measured subthreshold spectra of Fig. 5.9(a). It displays the cavity reflectivities as a function of the optical path length $l(m)$. As one can see, the laser resonator exhibits reflectivities at 68 μm and 76 μm for the laser design with the shorter cavity lengths, and at 114 μm and 125 μm for the laser design with the longer cavity lengths, which corresponds well with the physical resonator lengths of the two designs. For the laser design with the shorter cavity lengths one can observe higher harmonics which correspond to multiple cavity roundtrips, whereas for the design with the longer cavity lengths, the contribution from the second roundtrip is very minute. This is due to the fact that the spectrum for the first design is measured just below threshold whereas for the second case the spectrum is taken well below
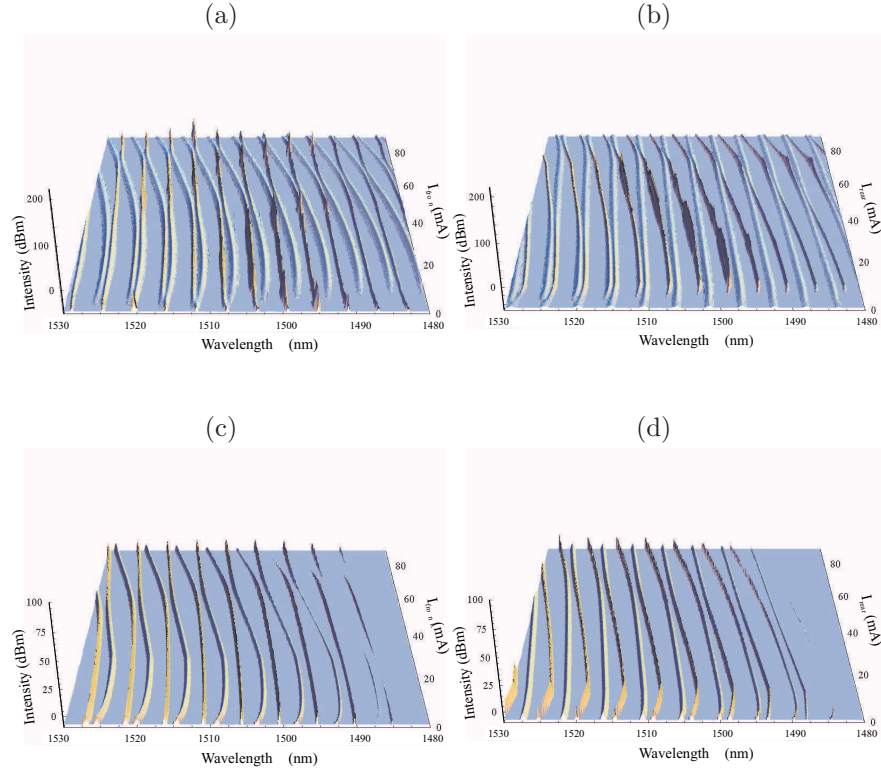
Figure 5.10: Intensity as a function of emission wavelength and segment bias. (a) measured intensity as a function of front segment bias (b) measured intensity as a function of rear segment bias (c) calculated switching behavior corresponding to (a) using transfer matrix model (d) calculated switching behavior corresponding to (b) using transfer matrix model.

threshold which can also be seen in the measured spectra. Although this model does not allow a quantitative analysis of the intra-cavity feedback properties it serves well to understand the strong intensity modulation due to mode interference between the two channel waveguides.

Switching behavior

Fig. 5.10(a) shows contours of the recorded optical output power versus the emission wavelength and the current into the front resonator. The current into the rear resonator is kept constant at 30 mA for this graph. One can identify two sets of longitudinal modes. One set of modes runs linearly as the current into the

front resonator is increased and belongs to the unperturbed resonator. A second set of longitudinal modes experiences the wavelength shift illustrated in Fig. 5.2 and belongs to the perturbed front resonator.

The modulated mode comb initially experiences a blue shift as a result of the increased carrier density. As a result, considering the interference with the rear resonator modes, the emission wavelength is experiencing a red shift. At higher injection currents however, the thermal contribution starts to override the carrier contribution leading to a red shift of the front mode comb so that the lasing wavelength shifts blue. The unperturbed mode comb is experiencing only a slight red shift which is a result of the overall heating of the sample as the current into the front resonator is increased.

Operating the device in the orthogonal configuration by varying the current in the rear resonator while keeping the front segment bias constant at 30 mA result in a mode switching behavior as displayed in Fig. 5.10(b). Here, laser emission occurs on the modulated mode comb that is shifting red until emission switches discontinuously towards higher wavelengths on the wavelength grid defined by the front resonator longitudinal cavity mode spacing. Although the initial blue shift of the rear waveguide mode spectrum can also be observed, it does not result in an actual blue shift of the laser emission.

Mode anti-crossings and transfer matrix model

Looking at Fig. 5.10(a) and (b), it is interesting to note that lasing does not occur at the mode crossings of the two combs. Instead, one observes a mode anti-crossing behavior and lasing occurs just before the mode combs would intersect. In order to explain this anti-crossing behavior, one has to consider the interaction between forward and backward travelling waves at the intracavity coupling section, fundamentally the same reason that led to the occurrence of the mini-stopbands. Instead of symmetrical higher order modes coupling to the fundamental mode within the individual waveguide as was the case for the emergence of the MSB's, now the two fundamental modes of the two contra-directionally coupled resonant cavities (which are symmetrical along the symmetry axis of each waveguide) couple at the photonic crystal intra-cavity coupling section. As

a consequence, the energies again repel such that the supermodes form an avoided crossing (or anti-crossing). This time, the anti-crossing effect has however important implications for the switching behavior of the device, so that we are applying a numerical model to predict the location of the avoided crossing points.

The interaction is expressed by a transfer matrix formalism for contradirectional devices [März2000]. From the transfer matrix of the integrated structure, the subthreshold continuous wave spectrum will be calculated.

Changes in the resonator's refractive index $n_0(1 + \Delta\lambda_s/\lambda)$ and gain profile $g_s(\lambda)$ due to carrier injection translate into changes of the complex propagation constant

$$\beta_s = \frac{2\pi}{\lambda}(n'_s + in''_s) = \frac{2\pi n_0}{\lambda}\left(1 + \frac{\Delta\lambda_s}{\lambda}\right) + \frac{i}{2}(g_s - \alpha_s) \qquad (5.11)$$

with α_s accounting for the cavity losses. n'_s, n''_s, and n_0 denote the real and imaginary parts of the refractive index in resonator s, and the real part of the refractive index with no bias present, respectively. $\Delta\lambda_s$ denotes the wavelength shift in resonator s due to carrier injection and is obtained from (4.3). The wavelength dependence of the segment gain $g_s(\lambda)$ is approximated by a parabola that experiences a red shift with increased temperature.

The waveguide segments and dielectric interfaces of our integrated tunable laser structure can be described by transfer matrices $\mathcal{U}^{xy}$. The dimensions of the matrices is determined by the number of modes propagating in the waveguide. As the field of the fundamental mode is predominantly localized in the core of the waveguide, its losses are lowest compared to the losses of higher order modes whose field distributions exhibit larger overlaps with the photonic crystal waveguide boundaries. Therefore, most of the energy in the waveguide is carried by the fundamental mode so that the discussion can be reduced to the discussion of single mode transmission in which case the matrices reduce to 2x2 matrices. Since the transfer matrices form a group, the product of two transfer matrices of this type results in a transfer matrix of the same type. The transfer matrix of our integrated coupled-cavity design is simply obtained by multiplication of the individual cavity transfer matrices [März2000]:

$$M^{total} = M^{(\text{FF})}M_1^{(\text{WG})}M^{(\text{IC})}M_2^{(\text{WG})}M^{(\text{RF})} \qquad (5.12)$$

where

$$M(r, \phi) = \frac{1}{t} \begin{pmatrix} \exp i\phi & r \exp -i\phi \\ r \exp i\phi & \exp -i\phi \end{pmatrix} \tag{5.13}$$

$$
\begin{aligned}
M_s^{(\text{WG})} &= M(0, \beta_s L_s) & M^{(\text{IC})} &= M(r_{12}, \theta_{12}) \\
M^{(\text{FF})} &= M(r_1, \theta_1) & M^{(\text{RF})} &= M(r_2, \theta_2)
\end{aligned} \tag{5.14}
$$

are the transfer matrices of the waveguides (WG), the intra-cavity (IC) coupling section, the front facet (FF) and rear facet (RF), respectively. θ_{ij} account for possible phase shifts at the mirror boundaries. These phase shifts are small considering the bandwidth-to-bandgap ratio of the system (30 nm compared to a bandgap of about 500 nm) and can be interpreted as Goos-Hänchen shifts representing modifications to the effective resonator lengths which only have a minor influence on the longitudinal mode spacings of the respective resonators and hence are assumed negligible. The reflectivities account for the reflectivities indicated in the inset of Fig. 5.2 and we assume $t_{ij}^2 = 1 - r_{ij}^2$. Then from the scattering matrix elements of the integrated system

$$
\begin{aligned}
S_{11} &= M^{total}[2,1]/M^{total}[1,1] \\
S_{12} &= (\det M^{total})/M^{total}[1,1]
\end{aligned} \tag{5.15}
$$

we obtain the spectral density of the amplified spontaneous emission R_{ASE} from the left facet by [Schatz1994]

$$R_{ASE} = \frac{hc}{\lambda} \frac{n_{sp}}{\eta_i} \left(|S_{11}|^2 + |S_{12}|^2 - 1 \right) \tag{5.16}$$

where n_{sp} is the population inversion factor, h is Planck's constant, and c is the speed of light.

A blue shift of the mode comb with smaller mode spacings results in an overall red shift of the emission wavelengths, whereas the red shift of the mode comb for higher bias currents results in an overall blue shift of the emission wavelengths. Figs. 5.10(c) and (d) display the calculated emission spectra for front and rear segment biases varying from 0 to 90 mA. All important features of the measured emission spectra are reflected in the calculated spectra.

For the case of current modulation in the front resonator while keeping the rear segment bias unchanged, the emission wavelength exhibits periodic shifts
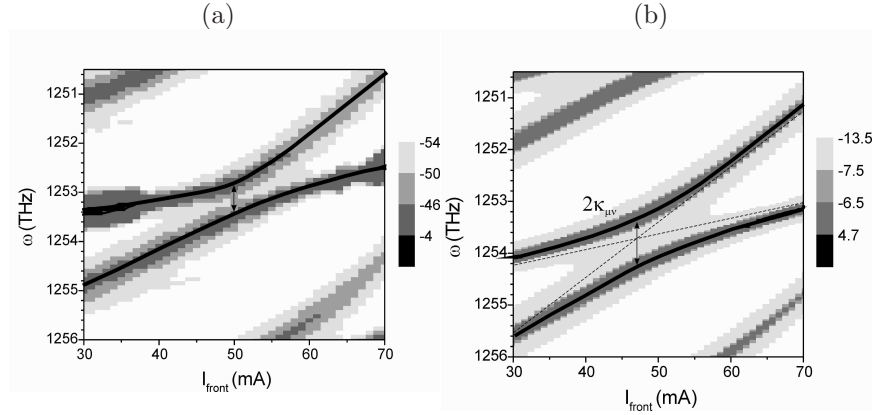
Figure 5.11: Determination of the coupling constant $\kappa_{\mu\nu}$ (a) measured intensity as a function of front segment bias (b) calculated switching behavior corresponding to (a) using transfer matrix model.

towards smaller wavelengths after an initial carrier induced red shift as explained and measured above. The lasing wavelength is located on the mode comb of the unperturbed cavity.

The thermal resistance of the rear segment is slightly lower compared to the front resonator as the heat flow is not perfectly one-dimensional and heat can dissipate in all directions away from the resonator whereas in the case of modulating the front resonator, the limited heat dissipation at the semiconductor-air interface results in an overall higher thermal impedance. The threshold is reduced due to the higher mirror reflectivities in the rear channel waveguide. These effects are considered in the simulation for the case of modulating the current in the rear resonator. The calculated emission spectra show that laser emission occurs on the mode comb of the perturbed cavity, resulting in a continuous red shift until the wavelength switches towards higher wavelengths on the wavelength grid defined by the longitudinal cavity mode spacing of the front resonator.

The change of wavelength caused by the increased segment bias is increasing due to the parabolic temperature increase and the anti-crossings occur at those points where the two mode combs of the partial resonators would overlap assuming a simple convolution of their mode spectra.

Mode anti-crossings and coupled-mode analysis

Figure 5.11(a) and 5.11(b) show contour plots of selected regions from Figs. 5.10(a) and 5.10(b) rescaled to angular frequencies. It becomes apparent that the modelled energy gap $2\kappa_{\mu\nu}$ is larger compared to the measured gap which can be explained by the out-of-plane diffraction losses that reduce the effective transmission rate $\tau_{\mu\nu}$ through the photonic crystal coupling section. It is possible to quantify the reduction in $\tau_{\mu\nu}$ by analyzing the energy gap of the avoided crossing points. The intracavity coupling constant $\kappa_{\mu\nu}$ between two modes μ and ν is proportional to the transmission $\tau_{\mu\nu}$ through the photonic crystal intra-cavity coupling section $\kappa_{\mu\nu} \propto \tau_{\mu\nu}$. The coupling of the two fundamental modes μ and ν propagating in each of the partial resonators can be expressed by the following coupled mode formulation:

$$\frac{d}{dt}\begin{pmatrix} E_\mu \\ E_\nu \end{pmatrix} = \hat{T} \cdot \begin{pmatrix} E_\mu \\ E_\nu \end{pmatrix} = \begin{pmatrix} j\omega_\mu(I) & -j\kappa_{\mu\nu} \\ j\kappa_{\mu\nu} & j\omega_\nu(I) \end{pmatrix} \begin{pmatrix} E_\mu \\ E_\nu \end{pmatrix} \qquad (5.17)$$

in which E_μ and E_ν denote the respective field amplitudes and $\omega_\mu(I)$ and ω_ν are the energies of the non-interacting cavity modes which are assumed behave linearly proximal to the avoided crossing points. The eigenvalues of $\hat{T}$ are given by

$$\omega_\alpha = \frac{1}{2}\left\{\omega_\mu(I) + \omega_\nu(I) + \sqrt{[\omega_\mu(I) - \omega_\nu(I)]^2 + [2\kappa_{\mu\nu}]^2}\right\} \qquad (5.18a)$$

$$\omega_\beta = \frac{1}{2}\left\{\omega_\mu(I) + \omega_\nu(I) - \sqrt{[\omega_\mu(I) - \omega_\nu(I)]^2 + [2\kappa_{\mu\nu}]^2}\right\} \qquad (5.18b)$$

which describe the hyperbolic behavior of the coupled cavity modes. The transmission coefficient $\tau_{\mu\nu}$=33% that has been used in the TMM calculation above was obtained from two-dimensional finite difference time domain (FDTD) calculations, therefore not considering losses. The size of the energy gap $2\kappa_{\mu\nu}$ obtained from this calculation is approximately 960 GHz. The experimentally observed energy gap is in the range of 780 GHz which corresponds to a transmission coefficient of 27%. It can be concluded that the remaining 6% are lost as a result of out-of-plane diffraction events.
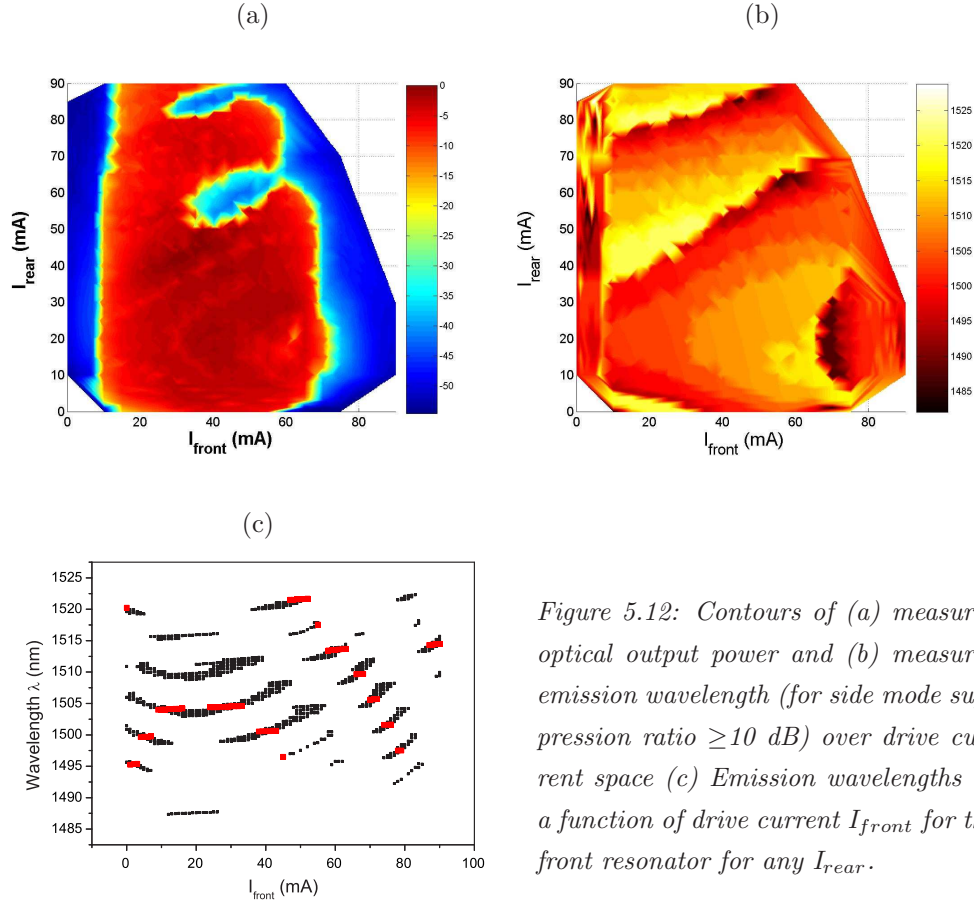
Figure 5.12: Contours of (a) measured optical output power and (b) measured emission wavelength (for side mode suppression ratio $\geq$10 dB) over drive current space (c) Emission wavelengths as a function of drive current I_{front} for the front resonator for any I_{rear}.

Tuning range

Through a systematic screening of the bias space by varying the current in one resonator for a discrete number of currents in the alternate resonator and observation of the emission wavelength, one obtains a wavelength map over an orthogonal current grid with 1 mA spacing on both axes. Fig. 5.12(a) and (b) display the recorded optical output power and emission wavelength (side mode suppression ratio $\geq$ 10 dB) over the drive current space. The wavelength forms certain plateaus over the bias current space. As one can see from the two graphs, an advantageous operating point of the device is to select a drive current for the rear resonator in the range of 10 to 20 mA since the output power at this plane, is sufficiently high while the wavelength can be readily selected by adjusting the drive current in the front resonator.
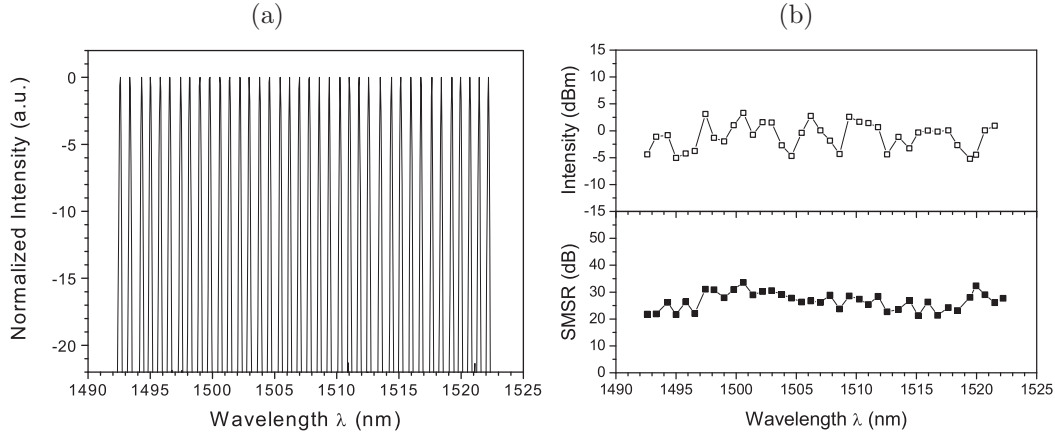
Figure 5.13: (a) Superimposed spectra displaying a tuning range of 29.6 nm with 36 channels (b) Optical output power and side mode suppression ratio over the tuning range.

Projecting the wavelength map of subfigure (b) onto the λ/I_{front}-plane (Fig. 5.12(c) with I_{rear} bias being a parameter, one can see that by appropriate selection of the two bias currents, one can access any wavelength in a window from 1495 to 1525 nm. Furthermore, it becomes obvious that a simultaneous modulation of the front and rear bias currents results in a continuous shift that can overcome the discontinuous mode jumps from the course tuning defined by the cavity mode spacings. This continuous wavelength shift can therefore serve as a fine tuning mechanism that allows access to all wavelengths in the relevant window. The measurement points indicated by red boxes display the accessible emission wavelengths for a constant rear segment bias of 30 mA, corresponding to the measurement displayed in Fig. 5.10(a). Fig. 5.13(a) shows the superposition of 36 wavelength channels spaced 0.8 nm apart corresponding to a 100 GHz channel spacing as typically required by WDM applications. All wavelengths within a tuning range of 29.6 nm can be accessed. 5.13(b) shows the optical output powers and side mode suppression ratios for each wavelength channel. Throughout the tuning range, output powers are in the range of 1 mW while side mode suppression ratios are in the range of 20 to 35 dB.

5.3   Design of photonic crystal waveguide bends

One of the major benefits expected from photonic crystal based optical components is their high integration density. Classical optoelectronic circuits such as ridge waveguide based combiner designs [Tal1999, Bach2001] have design dimensions of several millimeters. Various topologies have been suggested to guide light through ultra-sharp bends. Here, one has to distinguish between structures based on W1 and Wn (n=3, 5, 7,...) photonic crystal waveguides. In W1 waveguides, the mechanism to transport optical energy is based on the coupling of confined modes at typically very low group velocities. The electromagnetic field will always propagate into the region of increased dielectric material represented by the chain of defects of the W1 waveguide regardless of its direction. Being conceptionally the easiest to understand, its realization is very challenging however. Although the losses of straight W1 waveguide sections are reduced in a constant effort, bends and double bends based on W1 waveguides still exhibit strong losses. An extension of the width of the donator-type line defect to an odd number of missing rows has been shown to result in significantly reduced losses on straight waveguide sections. Here, the mechanism to transport energy is based on the effective index contrast between the waveguide core and the surrounding PhC region. The dispersion of the fundamental mode is comparable to the dispersion of light in bulk dielectric. The increase in the width of the waveguides however makes them inherently multimode, therefore increasing the complexity of guiding light through bend regions. Mode conversions at the boundary of the waveguide bend and couplings onto the lossier higher order modes (HOM) propagating in the waveguide can lead to significant reductions in transmission. The multimode nature of the Wn photonic crystal waveguides therefore demands a thorough design of the bend region in order to reduce these adverse effects [Sig2004, Tal2002, Agio2002, Ben2002].

5.4   Application to Y-coupler structures

In order to combine two light sources into a common output port, one can integrate two such double bends to form a Y-coupler structure. In this chapter, four different Y-coupler topologies are investigated with respect to their transmission characteristics. Fig. 5.14 gives an overview of the Y-coupler topologies that have been investigated. All Y-coupler structures have been realized in Γ-K orientation of the photonic crystal in order to facilitate low-loss 60 degrees bends.

   The primary goal for the design of Y-coupler structures is to minimize their transmission losses over a wide frequency bandwidth, the latter criterion being of particular importance when integrating tunable light sources. It is anticipated that most of the losses will be incurred in the bend region. The minimization of losses in straight photonic crystal waveguides embedded in weak transverse photon confinement topologies is straightforward and typically achieved by increasing the etch depth while attempting to maintain the shape of the cylindrical air holes. Fabrication is steadily improved and to date led to transmission losses in the range of 30 dB/mm for W1 waveguides in Γ-K orientation. The reduction of losses in waveguide bends, however, requires careful engineering of the bend region, particularly for waveguides supporting multiple modes.

In a first intuitive attempt to reduce the losses in the waveguide bends, in Design A the bend region is smoothened by moving three holes from one side to the other [Ben2002]. Fig. 5.14 (a.1) shows a scanning electron microscopy graph (SEM) of combiner Design A. Fig. 5.14 (a.2) shows the transmission from one of the symmetric input ports of the Y-coupler structure to the combined output port obtained from 2D finite difference time domain calculations in a normalized frequency window from 0.237 to 0.253 which is equivalent to a wavelength range from 1500 nm to 1600 nm considering the underlying lattice pitch of 380 nm. The shaded areas indicate the tuning range of 30 nm of the integrated laser sources. The reduced transmission translates into losses from the Y-coupler structure which are given by the second ordinate. As can be seen, the transmission varies between 3.6% and 28% in the relevant normalized frequency window which corresponds to losses between 5.5 and 14.4 dB.

In a second approach (Design B), the light is guided through the bends by to-
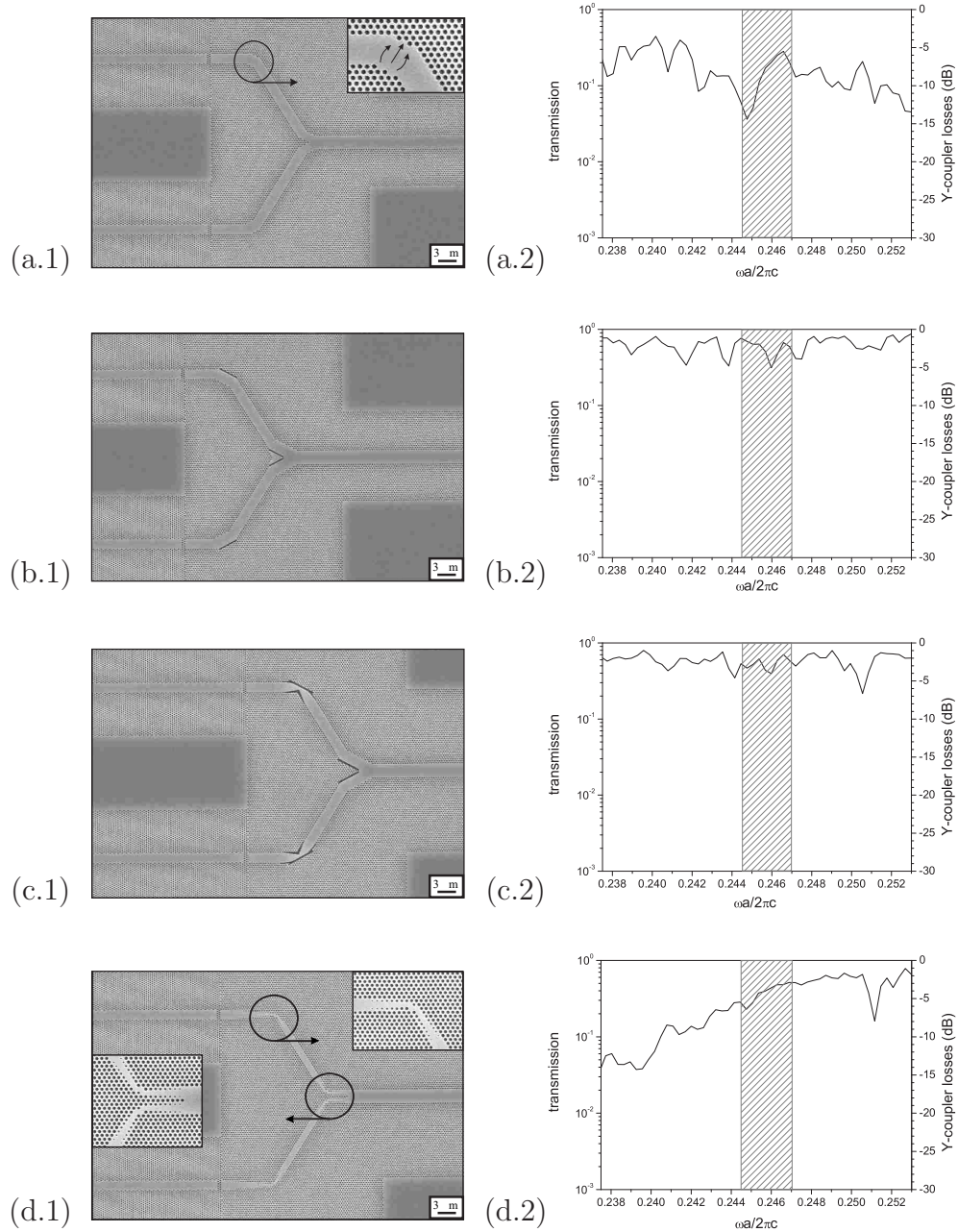
Figure 5.14: Scanning electron microscopy (SEM) graphs of various Y-coupler topologies (left) and transmission rates of various Y-coupler topologies in relevant normalized frequency window from 0.275 to 0.253 as obtained from 2D finite difference time domain (FDTD) calculations. From top to bottom: topology with moved holes in bend region, design with slit-like structures, design with tapered slits, and design with adiabatic taper structure.

tal internal reflection at high-index contrast slit-like structures introduced in the bends. The slits have a width of about 140 nm and are arranged in a 45 degrees angle with respect to the symmetry axis of the waveguide such that all modes including the HOM's are reflected at the facet into the waveguide whose lines of defects are rotated by 60 degrees towards the first section. Fig. 5.14 (b.1) shows a SEM graph of combiner Design B. Fig. 5.14 (b.2) shows the calculated transmission through coupler Design B. The transmission is significantly increased varying between 31% and 76% which translates into losses between 1.2 and 5.1 dB. The periodic dips are a result of Fabry-Perot resonances between the two 60° bends which form a low-Q resonator.

Besides the two solutions discussed above, an alternative design concept is to prohibit the existence of HOM's in the first place so that the light cannot couple onto the HOM's and is forced to propagate through the bend structure. This can be accomplished by adiabatic reduction of the waveguide width. One possibility (Design C) is to suppress the propagation of HOM's by narrowing the high-index contrast slits introduced in Design B [Agio2002]. The slits again have a width of about 140 nm and are tilted by about 20 degrees over a length of 1 μm to form a taper whose width reduces from the initial waveguide width to a width of about 700 nm. Additional slits ensure that the light is collected and guided through the bend. The region that leads into the combined output waveguide is equivalent to the topology of Design B. Fig. 5.14 (c.1) shows a SEM micrograph of Design C. Fig. 5.14 (c.2) shows the calculated transmission through coupler Design C. The transmission varies between 40% and 70% which translates into losses between 1.5 and 4.0 dB.

Alternatively, one can reduce the photonic crystal waveguide width from W5 to W1 in the bend region through the introduction of a photonic crystal taper design (Design D) [Tal2002]. The topology introduces a cascaded photonic crystal taper structure that narrows the width of the waveguide from W5 to W3 and subsequently to a W1 waveguide in the bends. The taper has been realized by adiabatically increasing of the hole diameter at the triangular lattice locations adjacent to the previous waveguide boundary. The pore diameter is increased in steps of about 15 nm from 30 nm to the target diameter of the surrounding photonic crystal lattice, therefore slowly 'turning on' a new photonic crystal
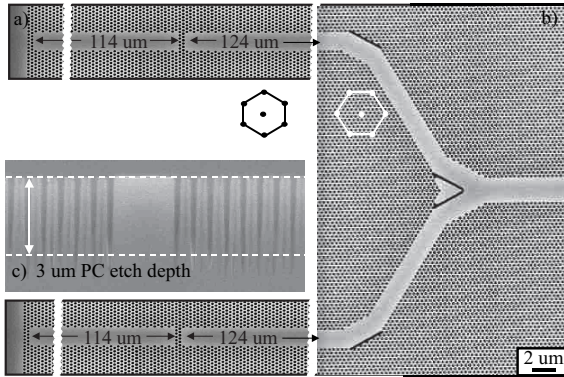
Figure 5.15: Scanning electron microscopy (SEM) graph of the integrated device (a) photonic crystal coupled-cavity laser source with waveguides along Γ-M orientation. (b) photonic crystal based Y-coupler in Γ-K orientation. (c) cross-sectional view of output waveguide, total etch depth is approximately 3 μm.

row confining the waveguide. The topology is shown in Fig. 5.14 (d.1). Fig. 5.14 (d.2) shows the calculated transmission through Design D. The transmission varies between 23% and 51% which translates into losses between 2.9 and 6.4 dB. Comparing the calculated transmissions of Fig. 5.14 for the various combiner topologies, one can conclude the following: while the transmission of the design with moved holes (A) could still be improved by further 'smoothening' the bend region, it still provides a good indication that the taper design (D) yields improved transmission characteristics. The slit-based topologies (B and C), however, are expected to result in the highest transmission rates.

The integrated devices are based on the active/ passive epitaxial layer structure A31136X described in Appendix D, their fabrication process is analogous to the fabrication process described in chapter 5.2. In this case, the photonic crystal structure is aligned to the active/ passive interface such that the coupled waveguides are located on the active part and the Y-coupler structure is located on the passive areas. All designs consist of two equivalent photonic crystal coupled-cavity lasers that are monolithically integrated with a photonic crystal Y-coupler structure. The tunable laser sources are based on the laser topology discussed in chapter 5.2 with lattice periods of 380 nm and air fill factors of 30%. The defect waveguides are based on 9 missing rows of air holes extending over a length of 173 periods or $173a$=114 μm for the rear resonator and 189 periods or $189a$=124 μm for the resonator adjacently defined to the Y-coupler structure, therefore resulting in longitudinal mode spacings of 2.9 nm and 2.6 nm for the rear and front resonators, respectively. The front resonators are separated from the Y-coupler input waveguides by a photonic crystal section of one lattice period. The tuning
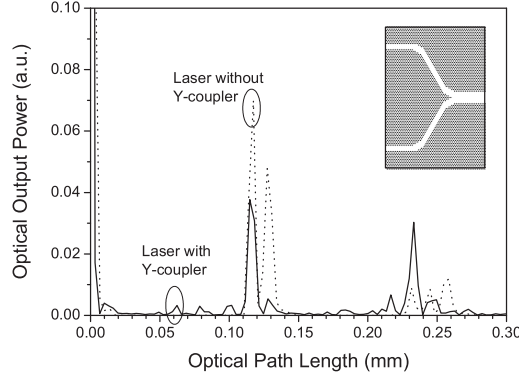
Figure 5.16: Analysis of intra-cavity scattering centers of the combiner topology with moved holes. The inset shows the corresponding FDTD computational window.

principle for the two laser sources is equivalent to the tuning of the single devices. To match the width of the waveguides in Γ-M orientation, the waveguide of the Y-coupler in Γ-K orientation leaves out 5 rows. The combined output waveguide has been cleaved. Fig. 5.4 shows an example of such an integrated design. Fig. 5.4(c) shows a cross-sectional view of the cleaved output waveguide.

For all measurements, the devices were mounted onto a temperature-controlled heat sink and the optical output power was measured at the cleaved end of the combined output facet of the integrated design. Threshold currents (for $I_1=I_2$) are in the range of 15 mA. First, the device is investigated under single port operation.

From the measured subthreshold spectra we wish to derive information about the internal scattering centers of the structures in analogy to the procedure followed in section 5.2. Fig. 5.16 shows the result of this effort starting from the measured subthreshold spectra. It displays the cavity reflectivities as a function of the optical path length $l(m)$. As one can see, the laser resonator exhibits reflectivities at 68 μm and 76 μm for the laser design with the shorter cavity lengths, and at 114 μm and 125 μm for the laser design with the longer cavity lengths which corresponds well with the physical resonator lengths of the two designs. One can observe higher harmonics which correspond to the optical feedback from multiple cavity roundtrips. Compared to the analysis without any integrated combiner design, one can see additional scattering centers. These additional scattering centers arise from the fact the cleaved output facet is forming new, unpumped resonators with the combining section, the two bends and the two front mirrors of the laser sources. The height of the respective intensity peaks provides an indi-
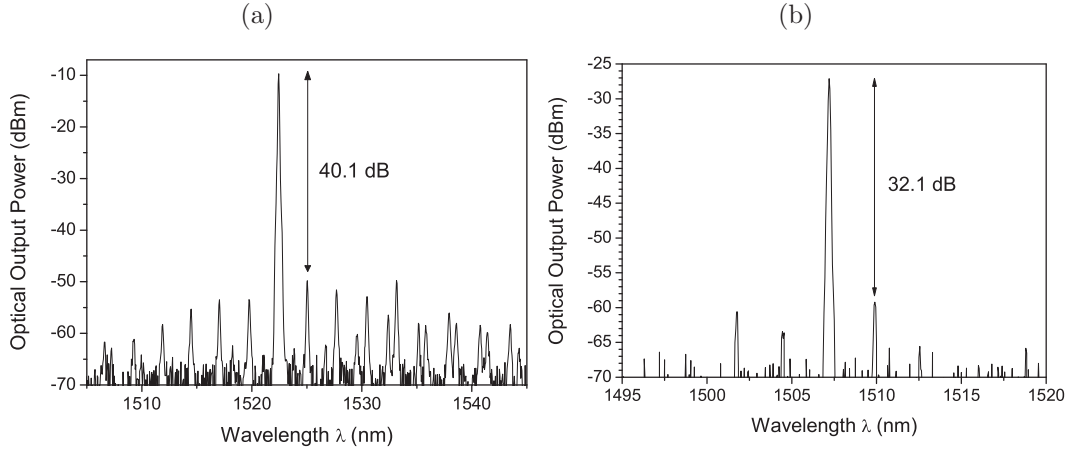
Figure 5.17: (a) Emission spectrum from Design B displaying the mode combs of the two cavities. Laser emission at this set of currents occurs at 1522 nm with a side mode suppression ratio of 40.1 dB. (b) Emission spectrum from Design A

cation for the significance of the scattering center, stronger scatterings resulting in more pronounced intensity peaks. The analysis therefore serves as a powerful tool to analyze the quality of the fabricated waveguide bends / combiner sections since the reflections from these regions are immediately transparent in the Fourier transformed subthreshold spectra. Compared to the various other combiner structures, topology A (with moved holes) exhibits the strongest scattering effects.

Fig. 5.17 shows output spectra of Designs A and B which are expected to exhibit the highest and lowest transmission of the Y-coupler structures investigated. Fig. 5.17(a) shows an output spectrum of Design B with a side mode suppression ratio of 40.1 dB. The currents into the resonators 1 and 2 are 13 mA and 69 mA, respectively. The side modes also show the different mode spacings of the two cavities. The output power under these bias conditions is -10 dBm, about 10 dB less compared to the design without any coupler structure. The 2D model predicted losses in the range of 1 to 5 dB as seen in Fig. 5.14 (b.2). The increase in loss is mainly due to scattering events at defects along the straight PhC channel waveguide sections.

For comparison, Fig. 5.17(b) shows an output spectrum of Design A. The currents into the front and rear resonator are 40 mA and 53 mA, respectively. Under
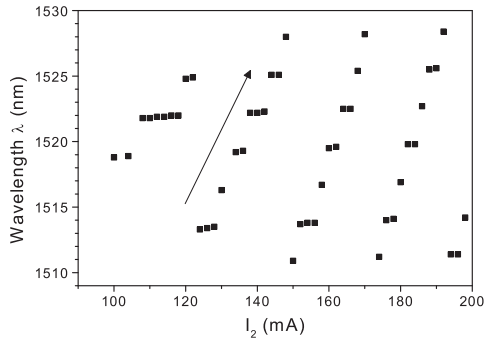
Figure 5.18: A red shift of the lasing wavelength can be observed as the current into the resonator 2 is increased. The current into resonator 1 is kept constant at 40 mA.
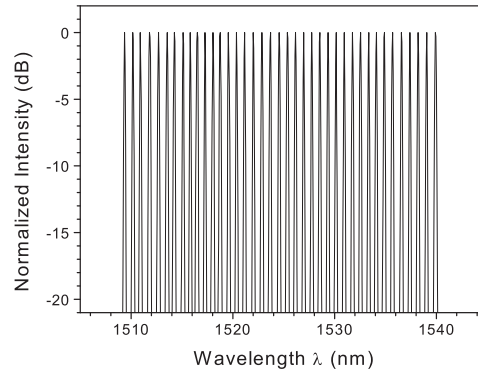

Figure 5.19: 39 superimposed spectra with 100 GHz channel spacing covering a total tuning range of 30.6 nm.

these bias conditions, the side mode suppression ratio is in the range of 32 dB, the output power in the range of -25 dBm. As can be seen, the introduction of the high index contrast slit-like structures improved the transmission by about 15 dB compared to the design with moved holes.

Fig. 5.18 shows the wavelength switching behavior of the structure integrating coupler Design B. The emission wavelength is plotted as a function of the front segment bias while the bias of the rear segment is kept constant at 40 mA. The switching characteristics is in good agreement with the expected tuning behavior: as the segment 2 bias is increased, the emission wavelength cyclically switches towards higher wavelengths on a grid defined by the cavity mode spacing of resonator 1.

As the current into both resonators is increased simultaneously, both mode combs shift towards higher wavelengths resulting in a continuous red shift of the laser wavelength and thus a fine tuning of the emission wavelength. Figure 5.19 displays the superimposed emission spectra of 39 modes that have been tuned using a combination of the course and fine tuning mechanisms. The overall tuning range is 30.6 nm with 100 GHz channel spacing as typically required by WDM applications. Side mode suppression ratios are in the range of 20 to 35 dB.

Combined operation of both ports allows simultaneous transmission of two freely selectable wavelengths. Fig. 5.20(a) displays the continuous wave spectrum of
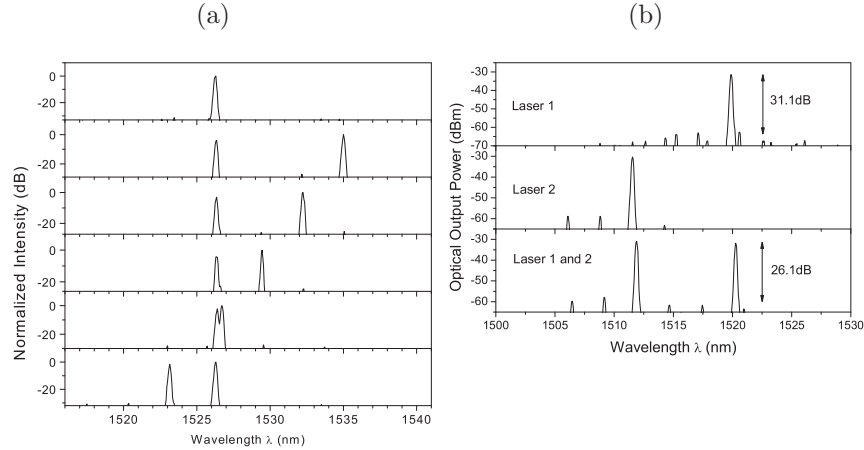
Figure 5.20: Output spectra under simultaneous operation. (a) Laser 1 is operated unperturbed while laser 2 is tuned discontinuously. (b) Output spectra of second design: single port operation of laser 1 (top) and laser 2 (center). Combined operation (bottom) leading to increased thermal crosstalk between the two laser sources.

device B when both laser sources are pumped simultaneously. The bias for one laser has been kept constant whereas the second source has been course tuned by modulating its front current while keeping the rear current unchanged as shown in Fig. 5.18. The output waveguide carries two wavelengths that can be controlled by modulation of the drive currents of the two laser sources. The wavelength of the unperturbed channel experiences a slight redshift of 0.1 nm due to thermal crosstalk between the two ports as the current into the second port is increased.

At higher drive currents, the thermal crosstalk between the two laser sources becomes more obstructive during combined operation, leading to a reduction in side mode suppression ratio. This crosstalk can eventually even lead to an earlier thermal rollover of the individual laser sources, therefore potentially limiting the tuning range of the devices. Fig. 5.20(b) shows example output spectra of a second design integrating coupler Design A. The currents into the front and rear segments of the top branch are 26 mA and 30 mA, respectively to result in laser emission at 1513 nm whereas currents of 27 mA and 26 mA result in laser emission at 1521 nm for the bottom branch. During single port operation, the side mode suppression ratios are in the range of 30 dB for the bottom (laser 1) and top branch (laser 2), respectively. Fig. 5.20(b) furthermore displays the continuous
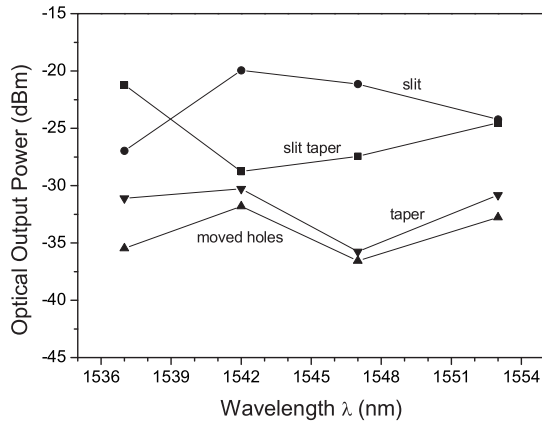
Figure 5.21: Measured trans-mitted power from the inte-grated devices.

wave spectrum of the device when both laser sources are operated simultaneously. The bias conditions are the same as for the individual laser operation displayed above in Fig. 5.20(b). As can be seen, the effect of thermal crosstalk between the two sources becomes more pronounced and shifts the emission wavelengths of both sources by 0.35 nm towards higher wavelengths. Since above threshold, the wavelength shift is proportional to the device temperature, this shift corresponds to an increase in temperature by about 3.7 K for both lasers. This tempera-ture increase is the result of the heat generated from the second laser source and therefore quantifies the thermal crosstalk. In order to reduce the thermal crosstalk between the two sources, it is either necessary to reduce the threshold by further reducing the cavity losses or to increase the spacing between the two ports. Thirdly, extending the PhC region from one laser to the second without the intermediate unpatterned region may also reduce the thermal crosstalk as the increased air filling factor leads to a reduction in heat flow across this region. In this case, the air can effectively serve as a thermal isolation between the two sources.

In order to further evaluate the transmission through the combiner structures, the optical output power is recorded at the switching wavelengths for the different bend designs. Fig. 5.21 displays the average optical output powers in the proxim-ity of the switching points of the integrated laser device for the various combiner topologies. As one can see, the tapered design results in an improved transmis-sion compared to the design with moved holes. The transmission through the slit design and the tapered slit design, however, provides the highest transmission

rates in the relevant wavelength range. This can be understood considering the underlying loss mechanism. Light propagating in the structure will experience intrinsic losses due to the limited light confinement in the transverse direction as well as out-of-plane scattering due to breaches in the periodicity of the waveguide. These breaches are formed by discontinuities of the otherwise perfectly-shaped straight photonic crystal channel waveguide which can arise from sidewall irregularities or severe irregularities introduced by the waveguide bends.

The transmission of the tapered design appears to be not as good as predicted by the calculations of Fig. 5.14 (d.2) which is due to the fact that the etch depth of the holes decreases with smaller hole diameter. As a result, light is diffracted into the lower cladding where it is ultimately absorbed introducing a significant loss mechanism for this design. The model however assumes infinitely extended cylinders regardless of the hole size, therefore leading to the greatest discrepancy between calculated and experimentally observed losses.

The electromagnetic waves propagating in coupler Designs A and D, which are entirely based on photonic crystal guiding, will experience strong reflections in the region of the waveguide bends. In the case of Design A, light is furthermore allowed to couple onto higher order modes which are more prone to out-of-plane scattering due to their larger field localization inside the holes, therefore providing a loss mechanism that leads to significant reductions in transmission for Design A.

The combination of photonic crystal waveguiding and high index contrast structures on the other hand reduces the generation of higher order modes and efficiently guides the fundamental mode through the 60 degrees bends[2]. The dominating loss mechanism for these two designs are out-of-plane scattering events at surface imperfections along the straight waveguide sections. Since the 2D photonic crystal prohibits scattering of light in the waveguide plane, in a future highly integrated optical microchip, PhC's can be utilized to efficiently isolate adjacent optical system blocks to avoid any unwanted crosstalk to adjacent regions of the highly integrated optical microchip which can hinder an effective operation of the device.

_____

[2]This finding has been confirmed very recently by several groups [Sig2004, Krau2004].

Chapter 6

Operation of 2D PhC near the bandgap: Ultra-refractive effects

Besides the formation of frequency bands in which no light is allowed to propagate, photonic crystals exhibit unusual dispersion properties in the vicinity of the photonic band edge. Instead of the common cone-shaped dispersion and associated spherical isofrequency contour lines known from bulk dielectrics or air-borne light propagation, the dispersion surfaces can exhibit very sharp or very flat regions.

Since it is a frequently recalled problem to separate light of different wavelengths in an optical network and there is a growing demand to integrate optical components into highly integrated photonic circuits, the widely used arrayed waveguide grating (AWG) filters are an inappropriate candidate for higher component integration as they are difficult to miniaturize to dimensions below 1 cm^2. The sharp changes in the photonic crystals isofrequency contour lines on the other hand can be utilized to realize compact and low cost filters that can be integrated in WDM networks that can then be deployed to the end user.

In a conventional prism as schematically depicted in Fig. 6.1, any incident (i) electromagnetic wave is in part reflected (l) and in part refracted (r) at a dielectric interface as depicted in Fig. 6.1. The three waves can be expressed as:

$$\vec{E}_i(\vec{r}, t) \;=\; \vec{E}_i^0 \; e^{i(\vec{k}_i \vec{r} - \omega t)} \tag{6.1a}$$

$$\vec{E}_l(\vec{r}, t) \;=\; \vec{E}_l^0 \; e^{i(\vec{k}_l \vec{r} - \omega t)} \tag{6.1b}$$

$$\vec{E}_r(\vec{r}, t) \;=\; \vec{E}_r^0 \; e^{i(\vec{k}_r \vec{r} - \omega t)} \tag{6.1c}$$

where $|\vec{k}_i| = |\vec{k}_l| = \frac{\omega}{c} n_0$ and $|\vec{k}_r| = \frac{\omega}{c} n$. The conditions that the electric and magnetic fields have to satisfy at the dielectric interface can simply be deduced from Maxwell's equations and must hold in both dielectric media. The three
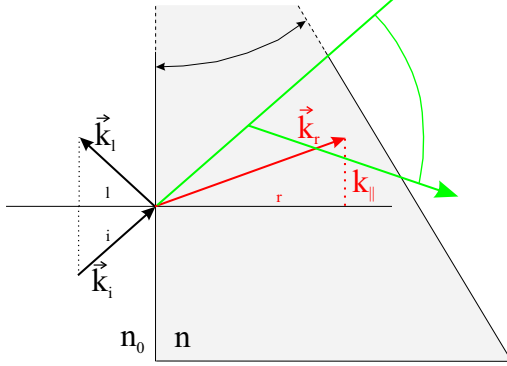
Figure 6.1: Schematic illustration of a conventional prism: Snell's Law
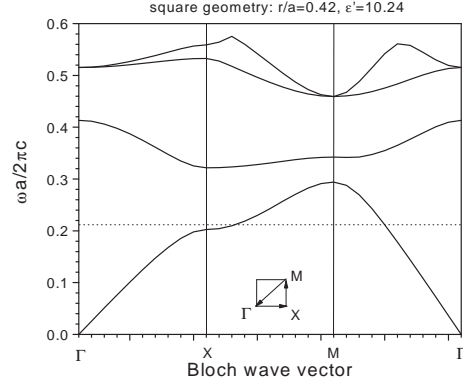
Figure 6.2: Dispersion relations of square lattice of holes in a dielectric along the main symmetry axes illustrated in the inset.

wave vectors of the incident, reflected, and refracted beams have to satisfy the following phase matching condition at the interface:

$$\vec{k}_i \, \vec{r}|_{z=0} = \vec{k}_l \, \vec{r}|_{z=0} = \vec{k}_r \, \vec{r}|_{z=0} \tag{6.2a}$$

$$|\vec{k}_i| \sin \theta_i = |\vec{k}_r| \sin \theta_r = |\vec{k}_l| \sin \theta_l \tag{6.2b}$$

$$n_0 \sin \theta_i = n_0 \sin \theta_l = n \sin \theta_r \qquad . \tag{6.2c}$$

From equation 6.2b, we can see that the above phase matching condition demands the continuity of the parallel components $k_\parallel$ of the three wave vectors across the dielectric interface. This condition, a direct consequence of momentum conservation, recalls Snell's law.

The deflection angle $\delta(\omega)$ of the incident light beam is given by the standard prism formula

$$\delta(\omega) = \theta_i - \alpha + \arcsin\left[\sin\left(\alpha\sqrt{n(\omega)^2 - \sin\theta_i{}^2}\right) - \sin\theta_i\cos\alpha\right] \tag{6.3}$$

where θ_i is the incident angle, δ is the frequency-dependent effective refracted angle after passing through both confining interfaces, and α is the prism opening angle depicted in Figure 6.1. The angular dispersion achievable for the conventional prism can be immediately derived by differentiating (6.3) and is in the range of 0.006 °/nm. On the other hand, diffraction gratings can lead to angular

dispersions in the range of 0.1 °/nm.

One of the most remarkable consequences of the anomalous dispersion properties of photonic crystals, is their high spectral dispersion at selected operating points. The reason for the high spectral dispersion of PhC's lies in the fact that the dispersion surfaces change dramatically with a change in energy. While a one-dimensional PhC, i.e. a Bragg stack, can also spectrally resolve light of different energies, the effect in a 2D PhC can be significantly stronger due to the significantly reduced group velocity of the light propagating inside the 2D PhC. This can be understood heuristically by looking at Heisenberg's uncertainty relation $\Delta E \Delta t \geq \hbar/2\pi$. In much the way as in time of flight measurements, the energy resolution can be increased by larger times of flight Δt, the longer interaction time of the slow Bloch modes with the 2D PhC lattice results in larger energy resolutions. Not surprisingly, the superprism phenomenon is best observed in regimes of low group velocity. As we will see later, the group velocity is defined as the slope of the dispersion curve so that one typically operates in the vicinity of the photonic band edge.

Figure 6.2 shows the band diagram of a 2D PhC with square lattice and r/a=0.42 for TE-polarized incident light and a dielectric backbone of $\epsilon = 10.24$ obtained from plane wave expansion calculations. The dotted horizontal line indicates a possible operating point of the device at a normalized frequency of about $\omega a/2\pi c$=0.21. This operating point will be subject of a more detailed discussion in section 6.2. As one can see, the group velocity in the vicinity of the X-high symmetry point is expected to be very low.

The dramatic change of the dispersion surfaces as a result of a small change in the incident light's parameters (incident angle or wavelength) results in large changes of the propagation direction inside the crystal. Two main regimes of the dispersion curves can be exploited. Regions of high curvature lead to a significant change in the group velocity, therefore also referred to as the group velocity dispersion effect. This effect can be used in photonic devices as a so-called S-vector superprism or a concave or convex lens. On the other hand, regions of almost vanishing curvature result in large changes of the Bloch wave vector, therefore commonly referred to as the phase velocity dispersion effect, an effect used in the so-called k-vector superprism and collimators. While the superprism effect was

(a)   (b)

(c)
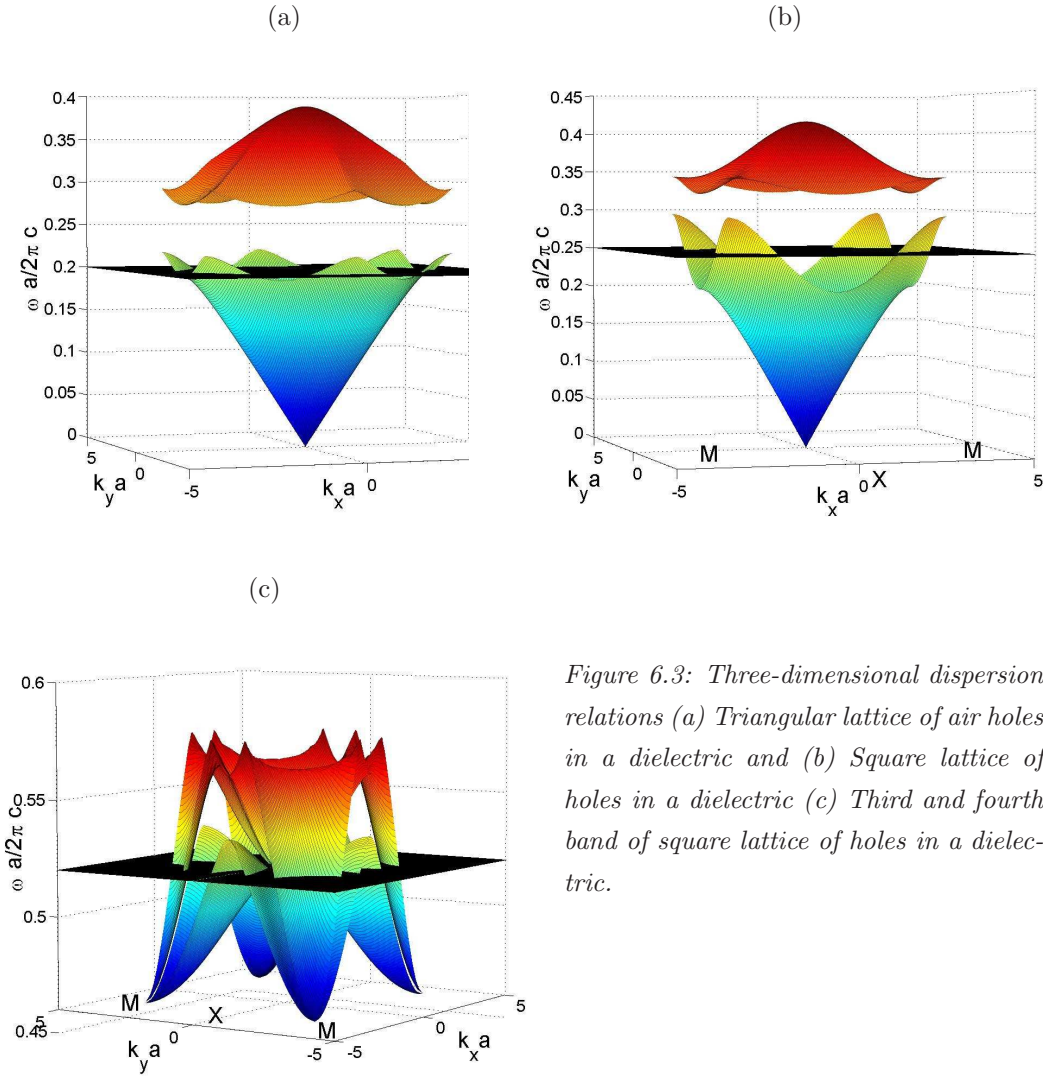
Figure 6.3: Three-dimensional dispersion relations (a) Triangular lattice of air holes in a dielectric and (b) Square lattice of holes in a dielectric (c) Third and fourth band of square lattice of holes in a dielectric.

first discussed using the phase velocity dispersion, most attention has been paid to the group velocity dispersion effect.

In the following chapter 6.1, the beam steering properties a 2D PhC's can exhibit at selected operating points will be briefly presented followed by a discussion of the superprism effects based on group and phase velocity dispersion in chapters 6.2 and 6.3, respectively. In chapters 6.4 and 6.5, the superprism effect is demonstrated for both a square lattice topology as well as for a triangular lattice topology. Finally, the chapter concludes with a discussion of the superprisms' resolution in 6.6.

6.1   Beam steering

It has been shown theoretically that the energy flux points into the direction of the group velocity, and is therefore given by the gradient of the dispersion curve [Chu1971]. The propagation direction is therefore normal to the iso-frequency contours as the group velocity $\vec{u}$ points towards the rate of greatest increase in energy. It points into the direction of the Poynting vector and is normalized by the energy density (both integrated over the volume of the unit cell):

$$\vec{u} \equiv \vec{\nabla}_k \omega(k) = \frac{\int_{cell} \frac{c}{4\pi} \vec{E} \times \vec{H} d\vec{r}}{\int_{cell} \frac{1}{8\pi} |\vec{H}(\vec{r})|^2 dr} \tag{6.4}$$

and therefore also describes the flow of energy in the system.

So far in this work, our analyses have relied on the dispersion diagrams $\omega(k)$. Now, one has to solve the inverse problem of finding the in-plane k-vector for a given frequency ω, i.e. one has to solve the Master equation for $k(\omega)$. To be able to do so, it is not sufficient anymore to look at the dispersion along the main symmetry axes of the crystal. Instead, it is required to obtain full information about the dispersion surfaces over the entire first Brillouin zone[1]. The dispersion surface of the irreducible Brillouin zone (IBZ) was obtained by scanning the k-space in a star-like fashion with the Γ-point as the center to the edges of the IBZ and computing the respective eigenenergies using the PWE method described in Appendix A.2.

Figure 6.3(a) shows the dispersion surfaces over momentum space for the first two bands of a triangular shaped 2D PhC with r/a=0.28. Figures 6.3(b) and (c) display the first two (a) and third and fourth (c) bands of a square shaped 2D PhC with r/a=0.42. As one can see, in both lattice geometries, photonic bandgaps are formed and the topologies of the dispersion surfaces reflect the hexagonal and square shape of the first BZ.

To determine the propagation direction inside the PhC for an incident light beam with a given incident angle θ_i and energy ω, one first determines $k(\omega)|_{\omega=const}$. This is equivalent to making a horizontal slice through the 3D dispersion dia-

---

[1]Given the symmetry of the crystal, it is sufficient to determine the dispersion surface over the full k-space of the irreducible Brillouin zone and to subsequently expand the information to the first Brillouin zone.

gram at frequency ω (or $\omega a/2\pi c$ on a normalized frequency scale) as illustrated
by the black horizontal planes in Figures 6.3(a) and 6.3(b). The result will be
an iso-frequency contour plot that exhibits sections with shapes similar to those
depicted in Figures 6.4(a)-(d).

As motivated in the next section, the component of $\vec{k}$ parallel to the interface
inside the crystal, $\vec{k}_\parallel$, will assumed to be (Bloch-) equivalent to that of $\vec{k}_i$ outside
the crystal after refraction. Therefore, a small variation in the incident direction
will result in small variations in $\vec{k}_\parallel$. Furthermore, changes in the incident beam's
frequency result in small changes in $\vec{k}_\parallel$ as well due to the expanded/contracted
light cone/circle.

Figure 6.4 illustrates how the curvatures of the isofrequency contours give rise to
a multitude of beam steering phenomena. For the example of a strong curvature
as illustrated in Figure 6.4(a), small variations in $k_\parallel$ lead to small variations in
$k_\perp$ but very large changes in the direction of the group velocities, here denoted
as $\vec{u}^{(1)}$ and $\vec{u}^{(2)}$. This strong dispersion of the group velocity inside the photonic
crystal can be used as a concave lens [Kos1999] or to resolve light of different en-
ergies into very different directions inside the crystal [Kos1998]. The latter effect
will be subject of discussion in section 6.2 and will be investigated experimentally
in sections 6.4 and 6.5.

A similar scenario arises for strong curvatures but inverse signature as depicted
in Figure 6.4(b). Here, small changes in $k_\parallel$ again lead to equally small changes
in $k_\perp$ and strong changes in the group velocities. This time, however, the group
velocities do not divert the energy flux, instead they point toward each other,
thus facilitating the functionality of a convex lens. This effect might become
instrumental in future integrated superprism designs as will be discussed lateron.
If a light beam is refracted to a region of the isofrequency contour that exhibits
almost vanishing curvature, i.e. is very flat in the k-plane, one can observe en-
tirely different phenomena. If the isofrequency contour is almost perpendicular to
the interface as depicted in Figure 6.4(c), small variations in $k_\parallel$ give rise to large
changes in $k_\perp$ but very small variations in the directions of the respective group
velocities. This strong dispersion of the phase velocities can be used to strongly
divert light of different energies after leaving the PhC and will be subject of a
brief discussion in section 6.3.

If, on the other hand, an isofrequency contour with small curvature is almost parallel to the PhC interface as illustrated in Figure 6.4(d), large variations in $k_\parallel$ lead to small variations in $k_\perp$ but only small changes in the direction of the group velocities. That means, incident beam that exhibit large changes in the incident angle or energy will eventually propagate in the same direction inside the PhC. Therefore, this effect can be instrumental when building a miniature beam collimator [Krau2003].

The former two effects can be grouped into effects based on the dispersion of the group velocity and work in regimes of strong curvatures of the isofrequency contours. Depending on whether the curvature (with respect to $\vec{k}_\parallel$) of the dispersion surface is positive or negative, the system will operate as an effective concave or convex lens, respectively. The latter two effects on the other hand, can be classified as effects based on the dispersion of the phase velocity and work in regimes of almost vanishing curvatures of the isofrequency contours. Depending on whether the isofrequency contour is perpendicular or parallel to the PhC interface, the system will operate as a super-diffractive device or a collimator, respectively.

6.2   Group velocity dispersion

A truly remarkable contribution to the understanding of the superprism effect was delivered by Kosaka et al. [Kos1998]. They investigated the superprism effect based on the dispersion of the group velocity inside the photonic crystal and proposed an analysis of how to determine the propagation direction inside the crystal. The analysis is based on the main assumption that the well known boundary conditions for a bulk dielectric interface (Fresnel equations) extend to the interface with a photonic crystal. Unfortunately, the phase matching condition (6.2b) only applies to the case of plane waves outside the PhC coupling with one or more plane waves inside the PhC, a condition which holds for an isotropic high index medium as given by standard prisms. In our case, however, the plane wave is coupling onto one or more Bloch modes propagating inside the PhC. To be rigorous, the phase matching condition for $\vec{k}_i$ and $\vec{k}_r$ of Figure 6.1 would have to be adapted to each of the Bloch modes independently which is
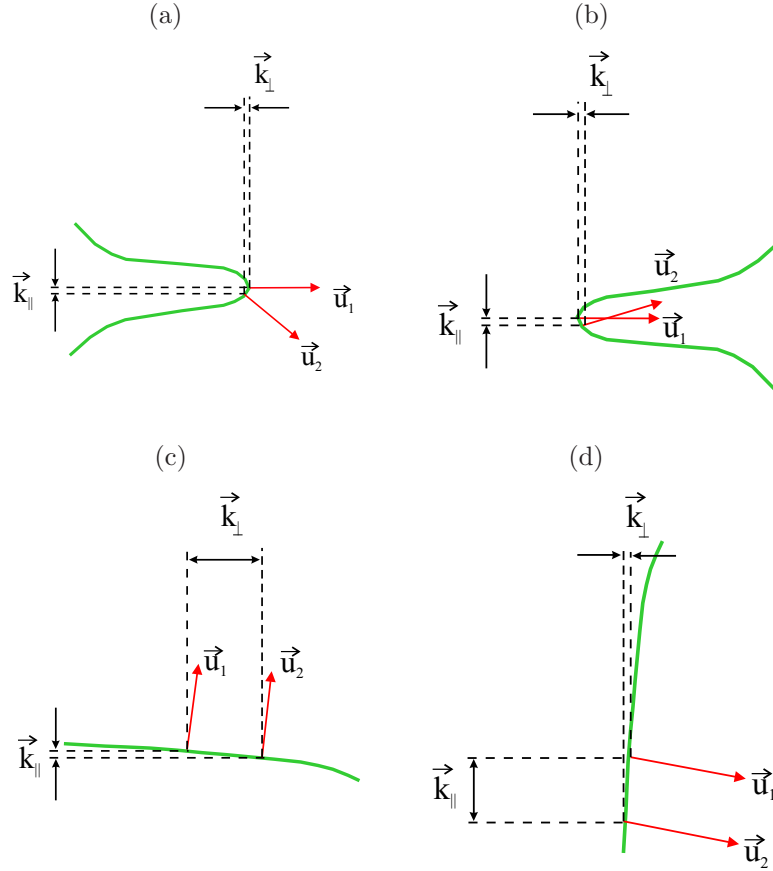
Figure 6.4: Dispersion effects. (a) Group velocity dispersion to be used as S-vector superprism or concave lens (b) group velocity dispersion to be used as convex lens (c) phase velocity dispersion to be used as k-vector superprism (inverse collimator case) (d) phase velocity dispersion to be used as collimator.

obviously an enormous task. Therefore, despite some reasonable questions about the applicability of the boundary discussion, so far it has served reasonably well to compare the experiment with predictions obtained from this model.

With that assumption, it is now possible to determine the propagation direction inside the photonic crystal. The procedure was first proposed by Kosaka et al. [Kos1998]. Figure 6.5 provides an illustration. Subfigure (a) shows the iso-frequency contours of the first band for a square lattice of air cylinders in a dielectric backbone (ϵ=12.9). The incident beam is a plane wave with wave vector $\vec{k}_i$ incident from the left that couples with one or more Bloch waves with Bloch wave vector $\vec{k}$ inside the PhC.

To determine the propagation direction, one proceeds as follows:

1. With a given frequency ω and incident angle θ_i of the incident beam, one first determines the component of $\vec{k}_i$, that is parallel to the waveguide/PhC interface, $\vec{k}_\parallel$. Since the iso-frequency contour of the access waveguide is known to be circular with a radius of $2\pi na/\lambda$, the position in k-space where the incident wave vector intersects the iso-frequency contour of the waveguide determines the perpendicular and parallel components, $\vec{k}_\perp$ and $\vec{k}_\parallel$, of the incident wave vector $\vec{k}_i$.

2. As motivated above, it is assumed that this parallel component is the same as of the beam propagating inside the crystal and one can therefore draw a help line ($k_\parallel$-construction line) to illustrate this assumption.

3. The flux of energy is perpendicular to the iso-frequency contours of the media in which it propagates. At the position where the $k_\parallel$-construction line intersects with the iso-frequency contour of the photonic crystal block one can therefore construct the normal to obtain the propagation direction of the energy flux inside the photonic crystal. The $k_\parallel$-construction line intersects at least twice with any isofrequency contour. Ambiguities can arise from the direction of the normal at the intersection and from multiple intersections of the $k_\parallel$-construction line with the isofrequency contour(s). While the former ambiguity can be easily resolved by a careful recollection of the direction of the gradient of the isofrequency contour which should point into the direction of greatest energy increase, the latter can only be resolved in the case of two intersections. This ambiguity is not surprising as it is a direct consequence of the inversion symmetry of the dispersion relation: if $\vec{k}$ is a solution of the wave equation, then $-\vec{k}$ is a solution as well [see equation (3.57)]. One solution describes the propagation into the PhC while the other the back propagation[2]. Since we are only interested in the wave propagating into the crystal, our selection criterion will be $k_\perp > 0$.

---

[2]Since the splitting into two beams will only occur after the wave has propagated some distance into the PhC, the reflected part will exit the PhC at a position that is laterally shifted from the entry position of incident beam which is nothing else but the Goos-Hänchen shift.

Multiple intersections (more than two) and possibly additional intersec-
tions with isofrequency contours of other bands on the other hand give rise
to so called *multi-branching* where the light is propagating into multiple
directions inside the PhC. This effect will increasingly occur if operating
in higher bands. Figure 6.3(c) shows the full k-space dispersion relations
of the third and fourth band of the square lattice topology in which the
isofrequency lines $k(\omega)|_{\omega=const}$ indicated by the black plane will contain the
contour lines of both bands so that for a wide range of incident angles the
multi-branching effect will occur. It is not clear, how the energy flux will
distribute into the various branches in such a case.

The situation here is essentially equivalent to the case of the concave lens. Since
the beam propagation inside the PhC is determined by the Poynting vector S
(direction of energy flux), one refers to the superprism that is based on the group
velocity dispersion as the *S-vector superprism*. The spatial separation of light of
different energies occurs inside the crystal.

 Despite the fact the superprism effect is observed by detecting the light that
is emitted perpendicular to the waveguide plane, therefore indicating a limited
in-plane optical mode confinement, the results reported by Kosaka et al. have
greatly contributed to the understanding of the superprism phenomenon.

6.3   Phase velocity dispersion

An alternative way to steer light of different energies into different spatial direc-
tions is to utilize the deflection of the k-vector. The effective index of a dielectric
material can be defined by $n = c/v_{phase}$ with v_{phase} of course being defined as
$v_{phase} = \omega/k$ so that

$$n(\omega) = \frac{c}{v_{phase}} = \frac{kc}{\omega} \tag{6.5}$$

Using the scalability of Maxwell's equations, Lin et al. investigated a photonic
crystal block for the microwave range consisting of dielectric rods in air [Lin1996].
They measured the angles of the incident and refracted light for various wave-
lengths just below the bandgap of the system and computed an effective refractive
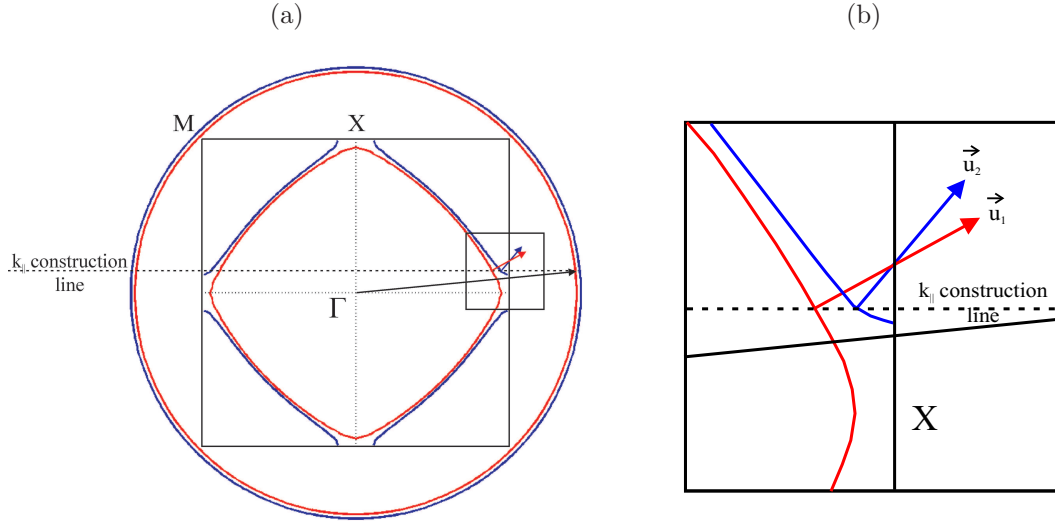
Figure 6.5: *Determination of propagation direction inside the PhC. The plot shows the iso-frequency lines over the in-plane k-space for the example of a square lattice with r/a=0.42 and TE-polarization. The blue and red lines correspond to normalized frequencies of 0.202 and 0.206, respectively. The solid lines indicate the edge of the first Brillouin zone. (a) Isofrequency contours of first Brillouin zone. The concentric circles describe the dispersion relation of the waveguide for the two normalized frequencies, the black arrow is the wave vector of the incident light, the vertical dotted line represents the waveguide/ PhC interface. (b) Relevant in-plane wave vector region to determine the propagation direction inside the photonic crystal.*

index the prism could be associated with using the standard prism formula (6.3) and by doing so, implicitly assumed that the anomalous refractive properties are caused by a dispersion in the phase velocity. Lin et al. observed a strong increase in this refractive index close to the band edge of the photonic crystal prism. While their work remained rather phenomenological, it was a first indication that the dispersion in the phase velocity can give rise to extraordinary refractive properties.

As mentioned before, in order to have the largest impact on the phase velocity, one has to operate in a regime in which the isofrequency contour exhibits a flat topology in k-space and is almost perpendicular to the PhC interface as depicted in Figure 6.4(c). The superprism effect based on phase velocities utilizes the deflection of the k-vector rather than the S-vector so that one can refer to it as a *k-vector superprism*. Inside the crystal, the propagation direction is still governed
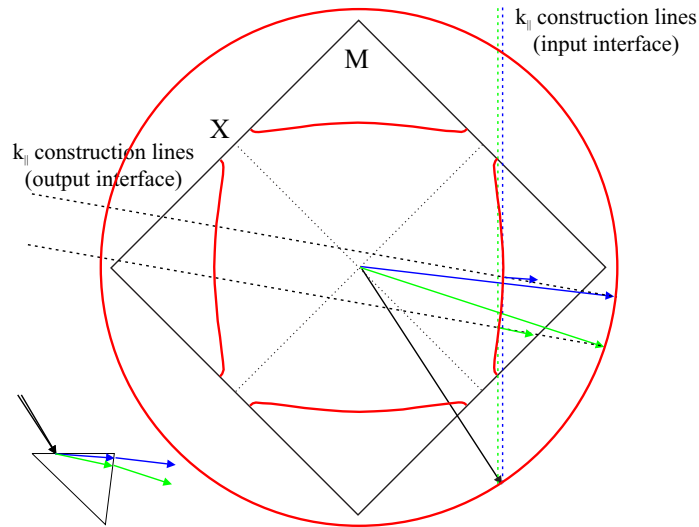
Figure 6.6: Determination of propagation direction for k-vector superprism. The plot shows the wavevector diagram for the example of a square lattice with r/a=0.42 and TE-polarization. The red line shows the isofrequency contour at a normalized frequency of 0.206. The solid lines indicate the edge of the first Brillouin zone. The green and blue dashed lines are the $k_\parallel$-construction lines for the input interface, the black dashed lines are the $k_\parallel$-construction lines for the output interface, the arrows indicate the S-vectors inside and the k-vectors outside the crystal. Bottom left: schematic of input and output interface and the different beam propagations.

by the deflection of the S-vector.

The analysis of the refraction is analogous to the analysis for the S-vector superprism [Joa2004, Baba2004]. The main difference lies in the fact that the spatial separation of light of different energies takes place after exiting the crystal so that the output interface has to be included in the analysis. Figure 6.6 shows the same wavevector diagram as before tilted by 45° and considering the isofrequency contour for a normalized frequency of 0.206 only. If $k_\parallel$ exhibits a slight shift, this time due to a marginal variation in the incident beam angle, $k_\perp$ exhibits a large shift as discussed before. As a consequence, considering conservation of $k_\parallel$ at the output interface of the crystal, the two beams have different k-vectors in the bulk semiconductor which will lead to a spatial separation of the beams.
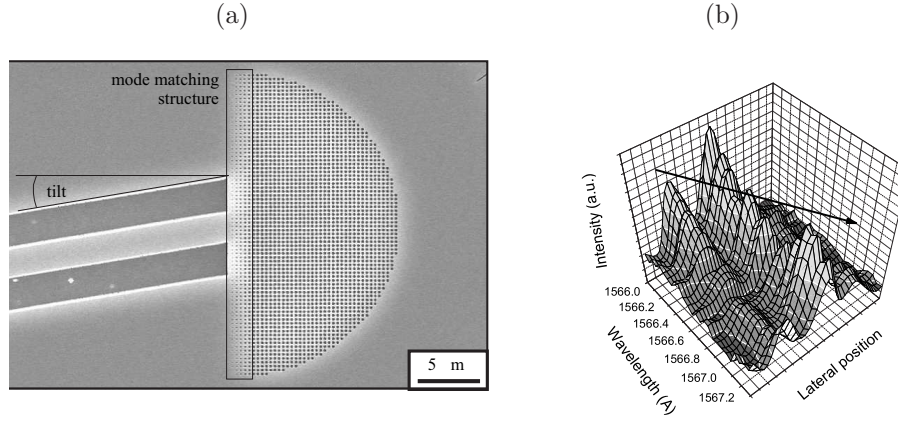
Figure 6.7: Superprism effect: as the wavelength of the incident light is increased from 1566.0 nm to 1567.3 nm, the light is refracted into the different output waveguides.

6.4 Ultra-refractive effects at square lattice of holes

In order to obtain the strongest group velocity dispersion effects, it is desirable to operate at points where the dispersion surfaces exhibit extreme curvatures. One can therefore expect that for the first band, the square lattice is the slightly more favorable candidate for this effect as its isofrequency contours exhibit strong curvatures in the vicinity of the X high symmetry point. The hexagonal shape of the first Brillouin zone of the triangular lattice on the other hand results in nearly circular isofrequency contours.

As a first example, a passive structure was investigated. The fabrication of the superprism is equivalent to the fabrication of the tunable photonic crystal coupled-cavity lasers discussed in chapter 5.2. The designs were fabricated on the passive sections of epitaxial layer structure A31136X described in Appendix D. An access waveguide with an initial width of 5 μm is gradually bent and hits a square lattice of air cylinders that are etched into the structure. The lattice pitch is chosen to be a=305 nm, the air fill factor is in the range of 42%. The access waveguide has been tilted by 7° to the normal of the bulk/PhC interface. The PhC block builds a semi-circle. The diffracted light is launched into an array of 2.4 μm wide output waveguides. The output waveguides are collecting the

diffracted light in steps of 5° and are defined by two confining air slits having
a width of 2 μm. In order to avoid optical losses in these bent output wave-
guides, the waveguides are gradually tilted from their respective starting angle
to the normal of the cleaved output facet. The output waveguides are required
to ensure that the light from each direction is hitting the dielectric/air interface
of the cleaved facet at 90° in order to ensure that they have the same reflection
properties at the facet.

A mode matching structure is defined in front of the waveguide/PhC interface
in order to reduce losses caused by the impedance mismatch between the modes
propagating in the access waveguide and the Bloch modes propagating inside
the photonic crystal. The mode matching structure consists of columns of air
cylinders arranged with the same pitch as the superprism lattice with the radius
of the pores increasing adiabatically from 0 to the target air fill factor inside the
superprism.

Figure 6.7(a) shows scanning electron microscopy graphs of the topology. Figure
6.7(b) displays the measured intensity as a function of its lateral position and
the wavelength of the incident light. Although the wavelength is only changed
by approximately 1 nm from 1566.0 to 1667.3 nm, the light is deflected by about
5°. Although at 1566.0 nm, the center peak is present already, as one increases
the wavelength of the incident light, the left peak is disappearing and instead,
a third peak is starting to emerge to the right. This light swing corresponds to
an angular dispersion of 4°/nm. However, for the underlying design, this prism
behavior could only be observed for narrow spectral ranges of a few nanometers
as illustrated in Fig. 6.7(b).

6.5   Ultra-refractive effects at triangular lattice of holes

As a second step, a design has been investigated that exhibits a triangular lattice
topology. The lattice pitch is selected as a=266 nm, the air fill factor is in the
range of 28%. The access waveguide has been tilted by 9° to the normal of the
bulk/PhC interface. As in the previous design, the PhC lattice is arranged as
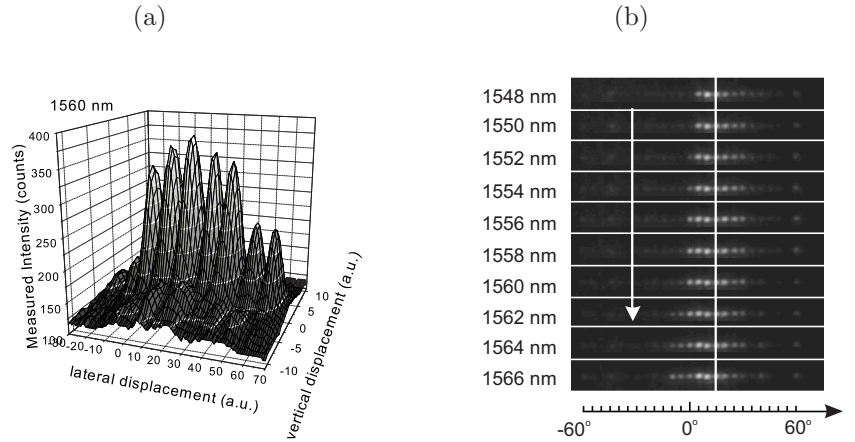
Figure 6.8: Superprism effect: as the wavelength of the incident light is increased from 1548 nm to 1566 nm, the light is refracted into the different output waveguides.

a semicircle and the light is launched into output waveguides that are designed such that the light from all output waveguides hits the cleaved output facet at normal incidence.

Figure 6.8(b) displays vidicon camera shots taken as the wavelength of the incident light is increased from 1548 nm to 1566 nm in steps of 2 nm. Each spot corresponds to the light output from the cleaved facet of one of the output waveguides. The center of the group of spots is clearly shifting from the 15° output waveguide to the 5° output waveguide which corresponds to an angular dispersion of 0.56 °/nm. This dispersion is similar to the angular dispersion observed for the design with square lattice but over a larger spectral range.

As one can see from Figure 6.8(a) and (b), despite the incident light having a defined frequency, the refracted light is launched into several of the neighboring waveguides adjacent to the target waveguide leading to a mode suppression of only about 0.2 dB. Three main reasons contribute to this limited channel suppression: beam divergence inside the semicircular photonic crystal region, beam divergence as the light leaves the photonic crystal and propagates through a short (10 μm) intermediate unpatterned region between the superprism and the output waveguides, and finally optical crosstalk between adjacent output waveguides. This lack of beam collimation has adverse effects on the superprism's resolution as will be outlined in the following section.

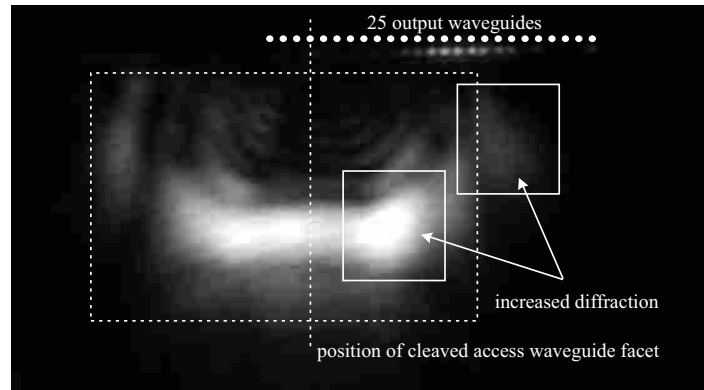*Figure 6.9: Diffraction losses from superprism: the vidicon camera shot displays the light diffracted into the lower cladding of the planar waveguide structure. The dotted box indicates light coupled into the lower cladding as it is launched into the access waveguide. The asymmetry in the intensity distribution is due to the additional contribution from light diffracted in the superprism.*

Compared to propagation through a straight ridge waveguide reference across the cleaved optical microchip, the signal is attenuated by at least 10 dB due to diffraction out of the waveguide plane into free space and into the lower cladding as the light hits the access waveguide/ photonic crystal interface and as it propagates through the superprism. Fig. 6.9 shows a vidicon camera shot over a larger area of the cleaved output facet. Clearly the light output from the output waveguides can be seen. Due to the 9° bend of the access waveguide, the superprism is located on the right and side of the cleaved facet of the access waveguide. Light is coupled into the lower cladding as it is launched from the single mode fiber into the access waveguide. Diffraction from the superprism into the lower cladding explains the asymmetry in the intensity distribution of the diffracted light in Fig. 6.9.

A comparison between the observed superprism phenomenon and the model outlined in section 6.2 is not feasible mainly due to two reasons. Firstly, since light is launched through an optical fiber, its polarization state is sensitive to the wavelength of the incident light, particularly important when tuning over larger wavelength ranges, the tension of the fiber and therefore any movements of the fiber, and the ambient temperature. A continued control of the polarization state would be necessary but was not accessible with the given setup as it would have led to subsequent misalignments in the setup. Hence, the polarization

state cannot be confirmed to be TE throughout the measurement. Secondly, the proximity effect described in Appendix B.1 produces a variation of the air filling fraction within the semicircular superprism with the center exhibiting a larger air filling fraction compared to the regions located at the edges of the semicircle. Since the shape of the dispersion surfaces are very sensitive to changes in the air filling fraction, the model would have to be continuously adapted as the light propagates through the semicircle.

Nonetheless, with a relatively simple setup and limited fabricational effort, it was possible to demonstrate the superprism effect for both a square lattice and triangular lattice of pores defined in a planar InP-waveguide structure. The angular dispersions observed for the superprisms are in the range of 0.5 °/nm.

6.6   Discussion of superprism resolution

The angular dispersion of 0.5 °/nm for the superprism is about 100 times larger than the angular resolution of about 0.006 °/nm of a conventional prism assuming a refractive index equivalent to the effective refractive index of the waveguide structure. Compared to the angular dispersion of 0.1 °/nm of a diffraction grating with grating pitch a embedded in refractive index equivalent to the effective refractive index of the waveguide structure, the angular dispersion is still about 5 times larger.

Another problem is the question of what the resolution for a given superprism is and how its dimensions have to be chosen in order to achieve a desired resolution. For the designs discussed above with a radius of the semicircular superprism of about 15 μm, one would have to extrapolate the design to a radius of about 700 μm in order to achieve a resolution of 0.4 nm with a similar output topology as described in the experiment, corresponding to a 100 GHz channel spacing at 1550 nm. Considering the losses due to out-of-plane scattering inside the PhC, this is currently an almost impossible task. An additional problem that became apparent from the experiment is the fact that the beam diverges inside the PhC. When estimating the resolution, it is however necessary to take the beam divergence inside the PhC into consideration and not only its angular dispersion
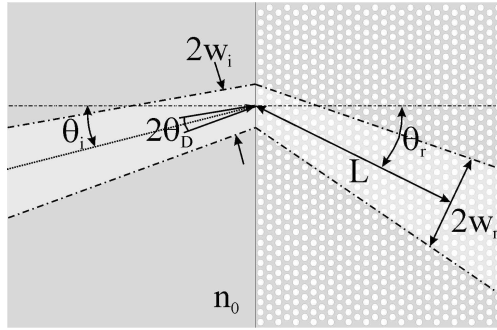
Figure 6.10: Illustration of beam propagation inside photonic crystal superprism to compute the resolution.

[Baba2002a]. In other words, an optical system mapping an input near field onto an output near field has to be integrated.

If considering a Gaussian beam incident at a bulk dielectric (with refractive index n_0) / 2D photonic crystal interface, then the full spectral width at $1/e^2$ intensity is given by:

$$2\theta_D = \frac{\lambda}{\pi n_0 w_i} \tag{6.6}$$

where λ/n_0 is the wavelength in the bulk dielectric and $2w_i$ is the spot diameter at $1/e^2$ intensity. Although the light in the photonic crystal is not propagating as a Gaussian beam since each plane wave component is expanded into Bloch waves at the input facet of the photonic crystal, the envelope of the intensity profile still can be approximated by a Gaussian if $2\theta_D$ is sufficiently small so that the beam width $2w_r$ at a far distance L from the bulk/photonic crystal interface can be expressed as

$$\frac{w_r}{L} \cong 2\theta_D \left(\frac{\partial \theta_r}{\partial \theta_i}\right) = \frac{\lambda}{\pi n_0 w_i} \left(\frac{\partial \theta_r}{\partial \theta_i}\right) \equiv \frac{\lambda}{\pi n_0 w_i} p \cdot \tag{6.7}$$

$p = \partial\theta_r/\partial\theta_i$ represents a measure for the beam divergence in the photonic crystal, and $1/p$ therefore represents a measure for the beam collimation. The far field angle $2w_r/L$ is depending on the beam width $2w_r$ so that the wavelength resolution is given by

$$\frac{\Delta\lambda}{\lambda} = \frac{2w_r/L}{a/\lambda} \frac{\partial(a/\lambda)}{\partial\theta_r} \cdot \tag{6.8}$$

Using equation 6.7 and defining a measure for the angular dispersion inside the photonic crystal (or its wavelength sensitivity) $q = \partial\theta_r/\partial(a/\lambda)$ we obtain a final expression for the resolution of the superprism that depends on both the

wavelength sensitivity and the degree of beam collimation:

$$\frac{\Delta\lambda}{\lambda} \cong \frac{2\lambda^2}{\pi n_0 w_i a} \left(\frac{q}{p}\right)^{-1} . \qquad (6.9)$$

The combined parameter (q/p) serves as a measure for the resolution of the superprism and is referred to as the resolution parameter.

A resolution of 0.4 nm around 1550 nm as typically required by WDM applications corresponds to $\Delta\lambda/\lambda = 2.6 \cdot 10^{-4}$. With q/p in the range of 40, n=3.40, and a=266 nm for the triangular superprism design investigated here, the resolution is only in the range of $\Delta\lambda/\lambda = 1.7 \cdot 10^{-2}$. From (6.9) one can see that in order to achieve the desired resolution of $2.6 \cdot 10^{-4}$, the width of the incident beam has to be in the range of w_i=160 μm. Surprisingly, even for this large spot size, only small regions on the dispersion surfaces can meet these requirements [Baba2002a]. Therefore, despite large values for the angular dispersion, the superprism resolution is limited due to the divergence of the beam inside the crystal which coincides with the experimental observation presented in sections 6.4 and 6.5.

The resolution is further reduced as a result of beam divergence as the light leaves the semicircular superprism and propagates through the intermediate unpatterned region between the photonic crystal and the output waveguides. Therefore, a subsequent beam collimation after leaving the superprism would be highly desirable and can be implemented by defining a PhC between the superprism and the output waveguide with dimensions chosen such that it operates as a collimator. An additional problem is the considerable optical crosstalk between the output waveguides which will furthermore contribute to the poor mode suppression in the output signal. The latter problem can be overcome through the introduction of photonic crystals separating the output waveguides. The limited mode discrimination observed in these studies acknowledge similar earlier results obtained by other groups [Krau2002] and suggest a fundamental limitation of the design.

Recently, it has been proposed that k-vector superprisms can lead to comparable magnitudes of angular dispersion as already experimentally demonstrated for the S-vector superprism [Joa2004, Baba2004] while exhibiting a smaller beam divergence, therefore leading to larger resolution parameters q/p. Furthermore, it is

expected that the PhC dimensions can be reduced by using the phase velocity dispersion effect since the spatial separation of light of different energies (or incident angles) does not have to occur inside the crystal but occurs after leaving the crystal. A verification of these predictions will be of great interest.

Chapter 7
Conclusion

In conclusion, the extraordinary dispersion properties of two-dimensional photonic crystals have been investigated theoretically and experimentally.

The existence of a photonic bandgap has been exploited to confine the propagation of light in the lateral propagation directions of the waveguide plane. Two novel types of widely tunable laser diodes based on photonic crystal mirror segments have been demonstrated. The designs are based on the contradirectional coupling of two independently contacted resonators exhibiting slightly different longitudinal mode spacing. The resonators are separated by a photonic crystal coupling section and therefore allow for a control of the coupling properties between the two resonators through a variation of the photonic crystal lattice parameters and thickness.

In a first design, the longitudinal mode spectrum was defined by a binary superimposed grating that was structured laterally to ridge waveguide segments. Tuning ranges between 25 nm and 50 nm have been experimentally demonstrated for this design. While the side mode suppression exceeded 22 dB throughout a tuning range of about 25 nm, it could not be maintained upon fine tuning the discontinuous tuning range of 50 nm, which could be due to an insufficient coupling of the fundamental mode to the lateral complex-coupled distributed feedback grating in order to define all ten predefined longitudinal modes for this design. An extension of the resonator length to increase the coupling has the disadvantage of also increasing the internal absorption. The laser exhibited external quantum efficiencies of about 68 mW/A typical for InGaAsP-based quantum well lasers suffering from large Auger recombination rates. The monolithic integration with an amplifier section leads to a subsequent signal amplification that can be used to stabilize the optical output power over the tuning range of the laser.

In the photonic crystal coupled-cavity laser design, the photonic crystal waveguide boundary provides the longitudinal and lateral photon confinement. Tuning

ranges of up to 30 nm were demonstrated for this design. Since surrounding the waveguide with photonic crystals reduces the scattering losses in the waveguide plane, out-of-plane scattering due to the limited transverse photon confinement is believed to be the dominant loss channel in these structures. For example, out-of-plane scattering was found to produce a reduction in the transmission co-efficient of the photonic crystal intra-cavity coupling section from 33% to 27%. It was found that the minimum width of the channel waveguide should be W5 in order to ensure laser operation since cavities of smaller widths exhibit very limited current injection efficiencies and high waveguide losses. The external quantum efficiency of the laser is doubled from 25 mW/A if based on W7 chan-nel waveguides to 48 mW/A if based on W11 waveguides. Two forms of avoided crossings have been observed experimentally in this context. The first was a re-sult of the coupling of the fundamental mode in a PhC channel waveguide to counter-propagating higher order modes (HOM) of the same symmetry which in turn gave rise to the formation of mini-stopbands (MSB). These MSB's can be used to stabilize the laser operation. Secondly, the coupling of the fundamental modes of the partial resonators led to formation of avoided crossing points in the switching characteristics of the device.

The photonic crystal coupled-cavity laser design is more compact and has the potential to exhibit less in-plane waveguide losses compared to the design based on gain-coupled distributed feedback due to the prohibition of scattered light propagation into the surrounding photonic crystal. On the other hand, the de-sign based on gain-coupled distributed feedback can potentially exhibit a larger tuning range and more uniform output powers throughout its tuning range due to the increased freedom of selecting the spectral position and amplitude of the longitudinal modes of its partial resonators. Both designs operate single mode as HOM's feature larger modal overlaps with either the lateral metal grating or the surrounding photonic crystal waveguide boundary, therefore exhibiting higher thresholds compared to the fundamental mode.

The integration of two identical tunable photonic crystal coupled-cavity lasers with a photonic crystal based Y-coupler structure demonstrate that the PhC coupled-cavity laser design can be readily integrated with other photonic circuitry to build more complex and densely integrated photonic circuits. When design-

ing the coupler structure, it was found that a combination of a photonic crystal backbone and classical high-index contrast slit-like structures leads to the best transmission properties if used as an optical interconnect for densely integrated photonic circuits for which no further signal manipulation such as pulse compression or group delay is desired. The high index contrast slit-like structures reduce the adverse effects of mode conversions and coupling onto HOM's in waveguide bends. The significant out-of-plane scattering losses of these coupler structures between 10 and 35 dB, however, demonstrate the need for further optimization of fabrication techniques or alternative means of controlling the propagation of light in the vertical direction, for example by embedding 2D photonic circuits in a 3D photonic crystal backbone.

The fascinating dispersion properties of 2D photonic crystals at the edge of the photonic bandgap were experimentally demonstrated to result in large angular dispersions in the range of 0.5 °/nm upon a change of the incident wavelength for the examples of a semicircular S-vector superprism with both a triangular and square lattice topologies. The resolution of the device is compromised by the significant optical crosstalk between the output waveguides, strong divergence of light propagating inside the photonic crystal superprism and beam divergence of light propagating through the intermediate unpatterned region between the photonic crystal and the output waveguides. The propagation losses are in the range of 10 dB compared to a straight ridge waveguide reference. Hence, the resolution and signal attenuation of the S-vector superprism do not yet meet the requirements of wavelength division multiplexing applications, a result that agrees with earlier reports by other groups. With respect to the present studies, more effort has to be spent with respect to the control of the polarization state and a reduction of the proximity effect in order to fully appreciate the superprism effect. In order to improve the superprism resolution, an investigation of the phase velocity dispersion effect in combination with a monolithically integrated photonic crystal collimator[1] seems a promising approach to achieve the resolution requirements of WDM applications while simultaneously reducing the component size. A further integration with either an adjacent active region to

---

[1]by possibly gradually moving from lattice parameters emphasizing the k-vector superprism effect to lattice parameters that result in a subsequent beam collimation within one PhC block.

convert the optical signal into an electronic signal, or - provided the optical power transmitted through the superprism is sufficiently high - an adjacent nonlinear medium to convert the optical signal into a change of the refractive index will lead to dramatically reduced component sizes since until today, this functionality can only be accomplished by two or more independent devices, namely an arrayed waveguide for demultiplexing the optical stream and an array of photodetectors for detection. Signal attenuation can be reduced by decreasing the index contrast in the superprism region. Provided the photonic bands do not intersect which would lead to multi-branching effects, scattering losses can be reduced while the resulting reduction in the width of the photonic bandgap does not affect the superprism functionality as it depends on the curvature of isofrequency contours of the dispersion bands rather than the existence of a photonic bandgap.

In view of the initially articulated dream of an all-optical microchip, it is generally desirable to control signals solely by optical means and to delay a conversion into an electric signal as long as possible. By doing so, the circuitry is liberated from the physical limitations of electronics, therefore allowing for unprecedented switching speeds and data rates which was a key motivation for the investigation of optoelectronic devices based on photonic crystals. It appears therefore desirable to control the refractive index in tunable light sources such as those discussed in chapter 4 or 5 by optical means as well. This can be accomplished through nonlinear effects such as the all-optical Kerr effect. It can therefore be expected that beside the investigation of three-dimensional PhC's which offer the control of light in all space directions, the investigation of nonlinear effects will attract increased research attention for the next years to come.

Appendix A

Numerical Tools

Due to the complexity of solving the Master equation in three dimensions, it is typically necessary to resort to numerical methods for its solution. Additionally, the boundary conditions for the observables have to be expressed in three dimensions which leads to an addition in the complexity of the solution. Only certain components of the electrical and magnetic fields are continuous at the boundary, more specifically the electric field components that are parallel to the boundary surface ($E_{\parallel boundary}$) and the magnetic field components perpendicular to the boundary surface ($H_{\perp boundary}$).

Several methods have been proposed for the solution of the Master equation (3.43) for the case of periodic dielectric media as is the case for of one-, two-, and three-dimensional photonic crystals. Depending on the problem, algorithms working in the time or frequency domain on one hand or algorithms working in real or reciprocal space can be employed.

In this chapter, three algorithms that have been used for the computation of photonic crystal problems are briefly introduced. Firstly, the transfer matrix method for the calculation of transmission in both frequency and real space. Secondly, the plane wave expansion (PWE) method for the solution of the Master equation in frequency and reciprocal space, and finally the finite difference time domain algorithm for the computation of the transient properties in time and real space.

A.1 Transfer Matrix Method

The transfer matrix method presents a very efficient tool for the computation of the transmission and reflection through a system of optical devices. It presents a method for the computation of Maxwell's equation in both frequency and real

space. Rewriting Maxwell's equations leads to

$$\vec{\nabla} \times \vec{\nabla} \times \vec{E} = -\nabla^2 \vec{E} + \vec{\nabla}\left(\vec{\nabla}\vec{E}\right) = -\frac{\epsilon(r)}{c^2}\frac{\partial^2}{\partial t^2}\vec{E} \qquad (A.1)$$

Transformation to frequency space leads to [Pen1992]

$$\left(\vec{k} \cdot \vec{k}\right)\vec{E}(\vec{k}) - \vec{k}\left(\vec{k} \cdot \vec{E}(\vec{k})\right) = \frac{\omega^2}{c^2}\sum_{\vec{k}'}\epsilon(\vec{k}, \vec{k}')\vec{E}(\vec{k}') \qquad (A.2)$$

Through the discretization of this expression on a cubic lattice one obtains a system of transfer equations which on one hand expresses the electrical field of one lattice layer following the propagation direction as a function of the electrical and magnetic field of the previous lattice layer and on the other hand, the magnetic field through the electrical field of the same layer and the magnetic field of the previous layer. Hence, one can ultimately express the next field in terms of the previous field:

$$\mathcal{F}(\vec{r} + \vec{c}) = \sum_{\vec{\rho}}\mathcal{U}(\vec{r}, \vec{\rho})\mathcal{F}(\vec{\rho}) \qquad (A.3)$$

where $\vec{r}$ and $\vec{\rho}$ are vectors in the same lattice plane, $\mathcal{F}$ denotes the in-plane field components of the electrical and magnetic fields, and $\vec{c}$ denotes the propagation direction. The transfer matrix $\mathcal{U}$ describes the transfer of a set of waves travelling from left to right (+) and right to left (-) through a series of optical devices. The input and output vectors consist of the waveguide eigenmodes forming the input and output ports of the optical circuit. The vector of the transmitted modes is given by

$$\begin{pmatrix} \Phi_{left}^{+} \\ \Phi_{left}^{-} \end{pmatrix} = \begin{pmatrix} \mathcal{U}_{++} & \mathcal{U}_{+-} \\ \mathcal{U}_{-+} & \mathcal{U}_{--} \end{pmatrix}\begin{pmatrix} \Phi_{right}^{+} \\ \Phi_{right}^{-} \end{pmatrix} \qquad (A.4)$$

Hence, $\mathcal{U}_{++}$ describes the interaction between waves travelling from left to right, and $\mathcal{U}_{--}$ the interaction between the waves travelling from right to left. The cross-diagonal elements $\mathcal{U}_{+-}$ and $\mathcal{U}_{-+}$ represent the interaction between the two incident and two outgoing waves, respectively.

If the electrical and magnetic field at the input of the system are known, it is therefore possible to compute the electrical and magnetic field through a successive iteration over the propagation area. Hence, the system's response to an

incoming electromagnetic field can be computed immediately through a multipli-
cation of the system's composing transfer matrices:

$$\mathcal{F}(\vec{r} + \vec{c}) = \prod_{i=1}^{N} \mathcal{U}^{(i)} \mathcal{F}(\vec{r}) = \mathcal{U}^{(total)} \mathcal{F}(\vec{r}) \tag{A.5}$$

This fact will prove to be instrumental in section 5.2 to compute the amplified
spontaneous emission spectrum of a system of coupled resonators.

Here, we wish to use the set of transfer equations to solve Maxwell's equations
to compute the band structure. Since, as we have learnt in chapter 3.2.2, the
periodicity in the dielectric constant results in a periodicity of the wave functions,
we can apply Bloch's law to the fields:

$$\mathcal{F}(\vec{r} + \vec{a}) = \mathcal{F}(\vec{r}) e^{ik_x a'} \tag{A.6}$$

$$\mathcal{F}(\vec{r} + \vec{b}) = \mathcal{F}(\vec{r}) e^{ik_y b'} \tag{A.7}$$

$$\mathcal{F}(\vec{r} + \vec{c}) = \mathcal{F}(\vec{r}) e^{ik_z c'} \tag{A.8}$$

Equations (A.5) and (A.8) form an eigenvalue problem for matrix $\mathcal{U}^{(total)}$:

$$\mathcal{U}^{(total)} \mathcal{F}(\vec{r}) = e^{ik_z c'} \mathcal{F}(\vec{r}) \tag{A.9}$$

with equations (A.6) and (A.7) representing the respective boundary conditions
to the problem. To compute the band structure, one now proceeds as follows
[Ward1996]: for any given frequency ω, one first computes the transfer matrix
$\mathcal{U}^{(total)}$ and from its eigenvalues considers only those k_z with vanishing imaginary
part, thus only considering those that correspond to propagating waves. Re-
peating this procedure for other frequencies, one finally obtains the band struc-
ture $k_z(\omega)$. A convenient and fast implementation of this algorithm is found in
[Reyn2000] that was used to compute the transmission and reflection plots de-
picted in Figures 4.1 (a) and (b). A second code, extended from a C++ algorithm
developed at the University of Würzburg [Kamp] was used to compute Figs. 5.10
and 5.11.

A.2 Plane-Wave Expansion

In chapter 3.2.2, it has been shown that a direct consequence of the periodicity of
the dielectric function is the applicability of the Bloch theorem which results in a

spatial periodicity of the eigenfunctions $\vec{E}_{\vec{k}n}(\vec{r})$ and $\vec{H}_{\vec{k}n}(\vec{r})$. The solution of the Master equation (3.43) starts with a Fourier expansion for the inverse dielectric function $1/\epsilon(\vec{r})$ and the electric and magnetic fields $\vec{E}(\vec{r})$ and $\vec{H}(\vec{r})$:

$$\frac{1}{\epsilon(\vec{r})} = \sum_{\vec{G}} \kappa(\vec{G}) e^{i\vec{G}\vec{r}} \tag{A.10}$$

$$\vec{E}_{\vec{k}n}(\vec{r}) = u_{\vec{k}n}(\vec{r}) e^{i\vec{k}\vec{r}} = \sum_{\vec{G}} \vec{h}_{\vec{k}n}^{E}(\vec{G}) e^{i(\vec{k}+\vec{G})\vec{r}} \tag{A.11}$$

$$\vec{H}_{\vec{k}n}(\vec{r}) = v_{\vec{k}n}(\vec{r}) e^{i\vec{k}\vec{r}} = \sum_{\vec{G}} \vec{h}_{\vec{k}n}^{H}(\vec{G}) e^{i(\vec{k}+\vec{G})\vec{r}} \tag{A.12}$$

where $\kappa(\vec{G})$, $\vec{h}_{\vec{k}n}^{E}(\vec{G})$, and $\vec{h}_{\vec{k}n}^{H}(\vec{G})$ are the expansion coefficients.

Limiting the further discussion to a solution for the magnetic field and inserting the expansions for $1/\epsilon(\vec{r})$ and $\vec{H}_{\vec{k}n}(\vec{r})$ into the Master equation, one obtains the central eigenvalue problem for the expansion coefficients $\vec{h}_{\vec{k}n}^{H}(\vec{G})$:

$$-\sum_{\vec{G}'} \kappa(\vec{G}-\vec{G}')(\vec{k}+\vec{G}) \times [(\vec{k}+\vec{G}') \times \vec{h}_{\vec{k}n}^{H}(\vec{G}')] = \frac{\omega_{\vec{k}n}^{2}}{c^{2}} \vec{h}_{\vec{k}n}^{H}(\vec{G}) \tag{A.13}$$

After determining the expansion coefficients $\kappa(\vec{G})$ for which one can write

$$\kappa(-\vec{G}) = \frac{1}{V_0} \sum_{\vec{r}} \frac{1}{\epsilon(\vec{r})} \exp{-i(-\vec{G})\vec{r}} = \kappa^{*}(\vec{G}) \tag{A.14}$$

with V_0 being the volume of the unit cell, the numerical solutions of equation (A.13) result in the dispersion relations of the given structure [Ho1990, Leung1990, Zhang1990]. Equation (A.13) simplifies when considering two-dimensional photonic crystals as all z-dependencies vanish:

$$\sum_{\vec{G}_{\parallel}'} \kappa\left(\vec{G}_{\parallel} - \vec{G}_{\parallel}'\right)\left(\vec{k}_{\parallel} + \vec{G}_{\parallel}\right) \cdot \left(\vec{k}_{\parallel} + \vec{G}_{\parallel}'\right) \cdot h_{z,\vec{k}_{\parallel},n}(\vec{G}_{\parallel}') = \frac{\omega_n^2(\vec{k}_{\parallel})}{c^2} \cdot h_{z,\vec{k}_{\parallel},n}(\vec{G}_{\parallel})$$

$$\tag{A.15}$$

For the computation of the band structures in this work, an algorithm based on the PWE method described above has been used that includes a number of numerical optimizations developed at the Massachusetts Institute of Technology [Johns2001].

A.3   Finite Difference Time Domain

Starting at Maxwell's equations for linear, non-dispersive, and isotropic media with no free carriers present and introducing a magnetic field density $\vec{M}$ in correspondence to the current density $\vec{j}$, one obtains the following symmetrized Maxwell equations:

$$\vec{\nabla}\vec{D} = 0 \tag{A.16a}$$

$$\vec{\nabla}\vec{B} = 0 \tag{A.16b}$$

$$\vec{\nabla} \times \vec{E} + \frac{\partial}{\partial t}\vec{B} = -\vec{M} \tag{A.16c}$$

$$\vec{\nabla} \times \vec{H} - \frac{\partial}{\partial t}\vec{D} = \vec{j} \tag{A.16d}$$

This symmetrization will allow for the inclusion of optical losses when evaluating the propagation through the structure and will be appreciated later for the formulation of absorbing boundary conditions. The current density and the newly introduced magnetic field density are expressed in terms of their respective fields, i.e.

$$\vec{j} = \vec{j}^0 + \sigma_E \vec{E} \tag{A.17a}$$

$$\vec{M} = \vec{M}^0 + \sigma_H \vec{H} \tag{A.17b}$$

where σ_E and σ_H are the electric and magnetic conductivities, respectively. Restricting ourselves to 2D PhC's eliminates all z-dependencies in Maxwell's equations. Analogous to the discussion in chapter 3.2.2, from (c) and (d) one can separate the field components and obtains two groups of equations that describe the evolution of the electrical and magnetic fields, respectively:

1. The Transverse Electric (TE) Group

$$\frac{\partial}{\partial t}E_x = \frac{1}{\epsilon}[\frac{\partial}{\partial y}H_z - (j_x^0 + \sigma_E E_x)] \tag{A.18a}$$

$$\frac{\partial}{\partial t}E_y = \frac{1}{\epsilon}[-\frac{\partial}{\partial x}H_z - (j_y^0 + \sigma_E E_y)] \tag{A.18b}$$

$$\frac{\partial}{\partial t}H_z = \frac{1}{\mu}[\frac{\partial}{\partial y}E_x - \frac{\partial}{\partial x}E_y - (M_z^0 + \sigma_H H_z)] \tag{A.18c}$$
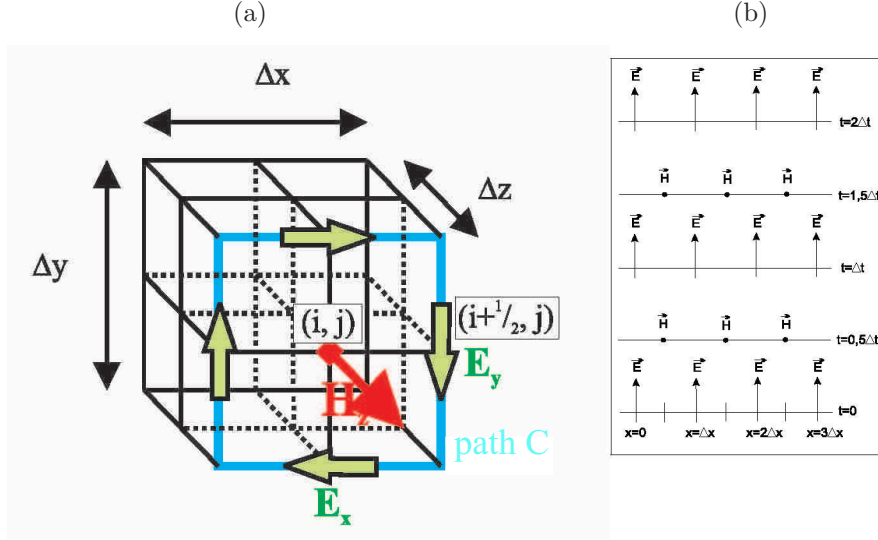
Figure A.1: Finite Difference Time Domain (FDTD) algorithm (a) Schematic of the Yee-cell (b) Illustration of leapfrog method [Sar2002].

2. The Transverse Magnetic (TM) Group

$$\frac{\partial}{\partial t}H_x = \frac{1}{\mu}[-\frac{\partial}{\partial y}E_z - (M_x^0 + \sigma_H H_x)] \tag{A.19a}$$

$$\frac{\partial}{\partial t}H_y = \frac{1}{\mu}[\frac{\partial}{\partial x}E_z - (M_y^0 + \sigma_H H_y)] \tag{A.19b}$$

$$\frac{\partial}{\partial t}E_z = \frac{1}{\epsilon}[\frac{\partial}{\partial x}H_y - \frac{\partial}{\partial y}H_x - (j_z^0 + \sigma_E E_z)] \tag{A.19c}$$

Again, focusing on the Transverse Electric (TE) group, the above stated system of scalar equations has to be solved for the TE-group. In the following, an algorithm, the so called Yee-algorithm [Yee1966], is presented to solve this set of equations. First, equation (A.18c) is discretized using the centered finite

difference method [Tafl2000][1]:

$$
\frac{\partial}{\partial t} H_z^{n+\frac{1}{2}} \;\; \rightarrow \;\; \frac{1}{\Delta t}\left(H_{z_{i,j}}^{n+1} - H_{z_{i,j}}^{n}\right) = \frac{1}{\mu_{i,j}}\left\{\frac{1}{\Delta y}\left(E_{x_{i,j+\frac{1}{2}}}^{n+\frac{1}{2}} - E_{x_{i,j-\frac{1}{2}}}^{n+\frac{1}{2}}\right)\right.
$$

$$
\left. -\frac{1}{\Delta x}\left(E_{y_{i+\frac{1}{2},j}}^{n+\frac{1}{2}} - E_{y_{i-\frac{1}{2},j}}^{n+\frac{1}{2}}\right) - M_{z_{i,j}}^{0,n+\frac{1}{2}} - \sigma_{H_{i,j}} H_{z_{i,j}}^{n+\frac{1}{2}}\right\} \quad \text{(A.22)}
$$

To further simplify the computational effort, the following approximation is introduced for the last term in the bracket: $H_{z_{i,j}}^{n+\frac{1}{2}} = \frac{1}{2}\left(H_{z_{i,j}}^{n+1} - H_{z_{i,j}}^{n}\right)$, in other words, the value of the magnetic field H_z at time $(n+\frac{1}{2})\Delta t$ is replaced by the average value of the neighboring time steps. For a cubic lattice where $\Delta x = \Delta y \equiv \Delta$, one obtains the central equation of the Yee algorithm:

$$
H_{z_{i,j}}^{n+1} = \overbrace{\frac{1 - \frac{\sigma_{H_{i,j}}\Delta t}{2\mu_{i,j}}}{1 + \frac{\sigma_{H_{i,j}}\Delta t}{2\mu_{i,j}}}}^{\equiv C_{i,j}^{a}} \cdot H_{z_{i,j}}^{n} + \overbrace{\frac{\frac{\Delta t}{\mu_{i,j}\Delta}}{1 + \frac{\sigma_{H_{i,j}}\Delta t}{2\mu_{i,j}}}}^{\equiv C_{i,j}^{b}} \cdot \left\{E_{x_{i,j+\frac{1}{2}}}^{n+\frac{1}{2}} - E_{x_{i,j-\frac{1}{2}}}^{n+\frac{1}{2}}\right. \quad \text{(A.23)}
$$

$$
\left. -E_{y_{i+\frac{1}{2},j}}^{n+\frac{1}{2}} + E_{y_{i-\frac{1}{2},j}}^{n+\frac{1}{2}} - M_{z_{i,j}}^{0,n+\frac{1}{2}}\,\Delta\right\}
$$

and similarly the terms for H_x, H_y, E_x, E_y, and E_z.

Considering the unit cell depicted in Figure A.1(a), called the Yee cell, and equation (A.23), one can see that the value for H_z consists of its old value at the same position and the symmetrically adjacent electric fields E_x and E_y in the x,y-plane.

The advantage of the selection of the Yee cell is that it implicitly satisfies the continuity of the electromagnetic field at interface boundaries. The time iteration is according to the leap frog method A.1(b). First, the electric field at time t_0 is computed over the entire space and saved. Then, the magnetic field is computed at time $t_0 + \Delta t/2$ and also saved. This is the basis for the computation of the

---

[1]The Taylor expansion of an arbitrary function $f(x,t)$ at position x_i is given by

$$
f(x_i + \Delta x, y_j, t_n) = f\big|_{x_i,y_j,t_n} + \Delta x \left.\frac{\partial f}{\partial x}\right|_{x_i,y_j,t_n} + \frac{\Delta x^2}{2}\left.\frac{\partial^2 f}{\partial x^2}\right|_{x_i,y_j,t_n} + \dots \quad \text{(A.20)}
$$

Subtracting the expansions of $f(x_i + \frac{1}{2}\Delta x, y_j, t_n)$ and $f(x_i - \frac{1}{2}\Delta x, y_j, t_n)$, one obtains

$$
\frac{\partial}{\partial x} f_{i,j}^n = \frac{1}{\Delta x}\left[f_{i+\frac{1}{2},j}^n - f_{i-\frac{1}{2},j}^n\right] + \mathcal{O}(\Delta x^2) \quad \text{(A.21)}
$$

using the notation $f(i\cdot\Delta x, j\cdot\Delta y, n\cdot\Delta t) \equiv f_{i,j}^n$.

electric field at time $t_0 + \Delta t$ and so forth.

One obtains a greater numerical stability of the algorithm if the electric and magnetic fields are determined at different positions within the unit cell. The algorithm used for the FDTD computations in this work is based on such a stacked discretization scheme. The computed magnetic field H_z is centered whereas the two complementary magnetic field vectors are computed at the cell boundary as depicted in Figure A.1(b).

The computational cell is truncated by boundary conditions such that incident waves are absorbed at the cell boundaries. The formulation of such absorbing boundary conditions (ABC) is a non-trivial task in the subwavelength regime. Mur's first and second order ABC's result in significant reflections, particularly in the presence of multilayered dielectrics, thus limiting the dynamic range of the computation. Berenger proposed an elegant method to express ABC's, called the perfect matched layer (PML) method [Ber1994]. It introduces an artificial reflectionless interface between the computational cell and the PML's at all incident angles. The layers themselves are lossy so that after a few layers the waves are significantly attenuated. Thanks to the introduction of a current and magnetic field density in the symmetrized Maxwell equations, the PML's themselves satisfy the symmetrized Maxwell equations.

The FDTD algorithm used in this work was implemented in C++ and developed at the University of Würzburg [Kamp].

Appendix B
Fabrication Technology

This chapter discusses the key processing technologies that allow the fabrication of the semiconductor devices investigated in this work, namely electron beam lithography (EBL) and three reactive ion etching technologies such as reactive ion etching (RIE), electron cyclotron resonance enhanced reactive ion etching (ECR-RIE), and chemically assisted ion beam etching (CAIBE). The chapter concludes with an overview of the fabrication steps that led to the various optoelectronic device designs explored in this work.

B.1   Electron Beam Lithography

An electron beam lithographic system allows the definition of structures with feature sizes as small as 10 nm. Within the framework of this work, an Eiko electron lithography system with 100 kV acceleration voltage is used. Fig. B.1(a) shows a schematic of this system. The electron beam is generated in a Schottky emitter (Wolfram coated with ZrO) heated to 1800 K. This configuration allows higher current densities compared to conventional LaB_6 cathodes while exhibiting similar current fluctuations ($\leq 2.5\%$/h) and beam diameters in the range of 2 nm. The electrons are accelerated in an electric field with up to 100 kV potential difference and focused by an electrostatic and an electromagnetic condenser lens onto the center of an aperture. A blanker allows turning the electron beam on and off. Two stigmators allow the definition of a circular beam shape. A coordinated change of the both condenser lenses allows an adjustment of the current without any readjustments of the electromagnetic objective lens. The objective lens projects the electron beam onto the wafer surface and has an integrated deflection unit that allows the 100 keV electron beam to be moved by 200 μm in both x- and y-direction. In order to write larger areas, the wafer is mounted onto a stage that can be moved by stepper motors. The stage position is controlled

by two laser interferometers that have a resolution of 2.5 nm so that the sample can be positioned with an error of < 20 nm.

The electrons hit the resist where they destroy its molecular chains, thereby increasing the solubility of the exposed areas in a developer. The exposed areas can therefore be subsequently selectively removed using a developer comprising methyl-isobutylketon (MIBK) and 2-isopropanol at a ratio of 1:3.

The dose is determined by the number of electrons hitting the resist in a given time interval Δt and by the distance d between two adjacently exposed dots, $D = \frac{I\Delta t}{d^2}$. For the Eiko EB-100 system used in the Würzburg microstructure laboratory, each 200 μm $\times$ 200 μm exposure field is discretized into 50,000$\times$50,000 dots that can be addressed and exposed individually. Therefore the minimum distance d between two adjacently exposed dots is 4 nm.

The spatial distribution of primary electrons around each exposed dot can be well approximated by a Gaussian with the origin of the exposed dot:

$$I^{pri}(r) = \frac{1}{r_0^2}e^{-r^2/r_0^2} \tag{B.1}$$

with r_0 being the electron beam radius so that the resolution is in a first approximation determined by r_0.

The primary electrons are forward scattered without a major impact on their direction when entering and propagating through the resist and generate low-energetic secondary electrons that have a mean path length of 10 nm in PMMA resist, therefore providing an improved estimate for the resolution of the system. The primary electrons continue to propagate through the PMMA until they hit a material with high atomic number, usually either the semiconductor material or a mask layer such as SiO$_2$ where they experience strong scattering effects. They again create secondary electrons, this time in the semiconductor or mask that propagate back through the PMMA layer. Given a sufficiently high energy of the primary electrons, these secondary electrons can expose a relatively wide area around the dot initially hit by the primary electrons, for energies of 100 keV a radius of about a $R = 10$ μm, therefore contributing to the total dose of the exposed dot. This contribution of course depends on the number of secondary electrons generated in the semiconductor/mask. The ratio η of secondary electrons to primary electrons is in the range of 1, i.e. each primary electron is
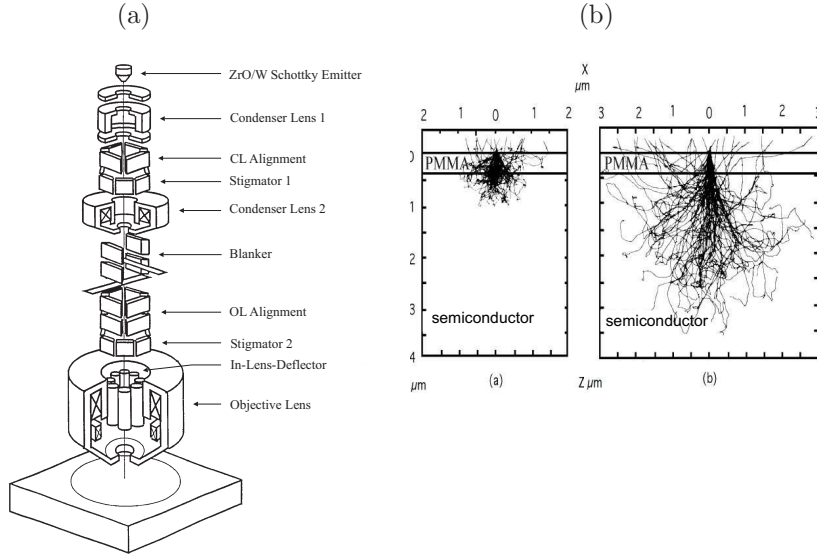
Figure B.1: (a) Cross-sectional schematic of an Eiko electron beam lithography system (b) Monte-Carlo simulation of proximity effect for 100 kEV primary electrons.

typically generating one secondary electron (η=0.9 for GaAs and 1.1 for InP). This effect becomes very significant when exposing dots that are in close proximity (for example when exposing a mesa or the superprism structure discussed in chapter 6) and is therefore referred to as the *proximity effect*. The total dose can therefore be approximated as the sum of two exposures, one by the primary electrons with a small exposure radius r_0 but high intensity and one from the secondary electrons with a large radius R but reduced intensity:

$$I^{total}(r) = \frac{1}{1+\eta}[\frac{1}{r_0^2}e^{-r^2/r_0^2} + \frac{\eta}{R^2}e^{-r^2/R^2}] \tag{B.2}$$

B.2 Reactive Ion Etching

In order to structure features with dimensions in the range of 10 nm at high aspect ratios, the use of reactive ion etching techniques is preferred. Wet chemical etching techniques do not provide the kind of anisotropy required to define features with dimensions in the range of 10 nm to a satisfactory depth. The etching is entirely based on chemical processes which can lead to an underetching of the etch mask. In this section, the basic principle of reactive ion etching (RIE) and

electron cyclotron resonance (ECR) assisted RIE will be outlined. Two other similar etch processes are the chemically assisted ion beam etching (CAIBE) and inductively coupled plasma (ICP) etching technique. The advantage of all these dry etching techniques is the addition of a physical sputtering process to a chemical etching process which is essential for pattering feature sizes in the range of 10 nm with an isotropic etching pattern.

In the classical reactive ion etching process, an electric field modulated at radio frequency (RF) through an adaptive capacitor network is coupled to a gas. The gas concentration is regulated by mass flow controllers for the individual gases and its pressure is in the range of 0.1 to 1 Pa. The electric field ionizes the atoms in the gas and ignites a plasma discharge. As the electrons have a much larger mobility compared to the ions due to their significantly larger charge to mass ratio, upon every positive half-wave of the electric field, the electrons are preferably accelerated to the sample holder and the walls of the chamber. The grounded walls are permanently discharged whereas the sample holder increasingly obtains a negative potential so that a bias voltage is established between the gas and the sample through the adaptive capacitor network. The bias voltage depends on the pressure of the gas and on the RF power. The negative potential of the sample holder now accelerates the positive ions of the plasma vertically onto the sample. Consequently, one obtains a combined etching process that has both a chemical and mechanical component as depicted in Figure B.2(a). The chemical etch component is a result of the gas ion's and radical's reaction with the atoms of the sample to build new molecules. For III-V semiconductors, Chlorine proved to be particular appropriate. Three Chlorine radicals connect with one group III semiconductor atom to build a new molecule. The mechanical component is a result of the sputtering effect of the positively charged ions vertically hitting the sample surface. For the mechanical component one additionally uses Argon with its low ionization potential energy and high masses resulting in an effective sputtering effect. The Argon ions have two effects: the kinetic energy breaks the chemical bonds of the semiconductor material on one hand, and secondly helps to desorb the heavy molecules obtained from the chemical etching component. The vertical direction of the ions results in the often desired anisotropy of the etching process that are essential to obtain high aspect ratios. A careful selection
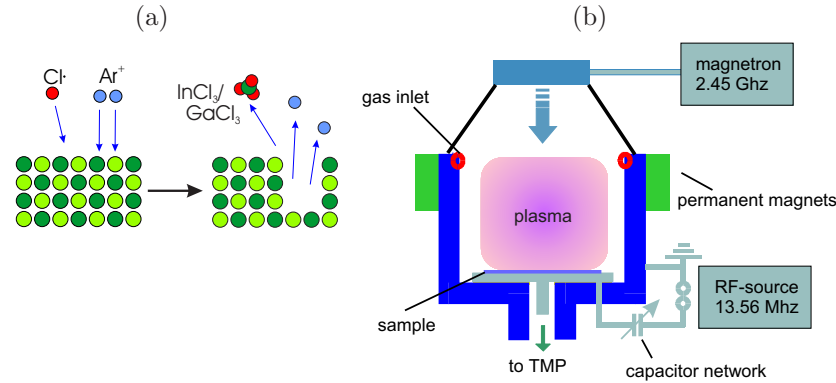
Figure B.2: (a) Schematic of the etching mechanism (b) Schematic of an ECR-RIE system.

of the RF-power and mass-flows of the gases in principle allows the fabrication of the frequently desired vertical side walls of the patterns. This etching process will be used to transfer the photonic crystal pattern from the resist to the SiO_2 etch mask.

 Disadvantage of the RIE process is the very limited penetration of the RF-field into the plasma resulting in a small ionization density of the gas (plasma density). Furthermore, an independent control of the RF-power and bias voltage can lead to a better control of the etch process. In the RIE process described above, as an increase in the RF-power always results in a simultaneous increase of the plasma density as well as the bias voltage so that an independent control of these two etch parameters is impossible.

This can be achieved by introducing a second mechanism to couple energy into the gas by the ECR-RIE etch process [Prost1997]. Here, the cyclotron resonance of the electrons in the magnetic field B_0 of a permanent magnet is used to additionally couple microwave energy through a magnetron resonantly into the plasma. Its frequency of 2.45 GHz is chosen to satisfy the cyclotron resonance condition $\omega = -e\, B_0/m_e$. The electrons' path lengths are extended as they are forced onto spiral traces in the plasma. This results in larger plasma densities which facilitate higher etch rates. The small bias voltages involved in this process lead to reduced damages at the semiconductor surface.

Fig. B.2(b) shows a schematic of an ECR-RIE etching system. Mass-flow controllers are ensuring a continuous flow of gases into the etching chamber that is

Parameter	PhC SiO$_2$	PhC InP	RWG	slanted pores
Process	RIE	ECR-RIE	ECR-RIE	CAIBE
Ar-flow	7.2 cm^3	19 cm^3	2 cm^3	5 cm^3
Cl$_2$-flow	-	4 cm^3	19 cm^3	1 cm^3
CHF$_3$-flow	15 cm^3	-	-	U$_{acc}$=400 V
RF-power	50 W	150 W	180 W	I$_{acc}$=2 mA
magnetron power	-	1000 W	1000 W	U$_{beam}$=600 V
U$_{DC}$	250 V	180-400 V	100-400 V	I$_{beam}$=44 mA
Process duration	2000 s	5:30 min	3:30 min	15:00 min
Process pressure	N/A	2.6 10^{-3} mbar	2.2 10^{-3} mbar	0.15 mbar

Table B.1: Etch parameters used for device fabrication

initially in a state of an ultra-high vacuum with pressures in the range of 5-15 10^{-7} mbar. Two electrodes are located in the chamber that are connected to a voltage that alternates at a radio frequency (RF) of about ν_{RF}=13.56 MHz. The electric field generated by this RF voltage ionizes the gases flowing into the chamber, therefore generating a plasma with a density in the range of 10^{10} cm^{-3}. In summary, the ECR-RIE process has the following major advantages compared to the classical RIE process:

- Introduction of a new degree of freedom for the selection of the plasma density.

- The RF-power can be reduced while maintaining or even increasing the etch rate facilitating reduced surface damages.

- Due to the more effective ionization of the gas, the gas density can be reduced. Consequently, the chamber pressure can be reduced by one order of magnitude which is essential for the desorption of the heavy InCL$_3$ molecules from the semiconductor surface.

The ECR-RIE process has been used to transfer the photonic crystal pattern from the SiO$_2$ mask to the semiconductor on one hand and, and secondly to define ridge segments for the design with lateral gain-coupled distributed feedback.
The etch parameters used throughout this work are listed in table B.1.

Appendix C
Device Characterization

In order to characterize the fabricated devices, a number of different measurement setups can be utilized to measure the power characteristics and the spectrum under continuous wave (cw) and pulsed pumping conditions, the relative intensity noise, small signal response, and linewidth of the device. For passive structures, measurement setups for transmittance and reflectance spectroscopy can be utilized to measure the intensity of light transmitted through or reflected off the structure. Typically the instruments are driven by a personal computer that is connected to the devices by a general purpose interface bus (GPIB).

C.1 Static laser properties: Continuous-wave and pulsed measurement setup

The continuous wave (cw) measurement setup is schematically displayed in Figure C.1. The laser sample is placed onto a heat sink whose temperature can be controlled in a range from 10 to 120°C through a Peltier element located underneath the sample holder surface. The heat sink simultaneously serves as the n-contact of the setup. The circuit is closed by positioning electric probes onto the p-contacts of the sample. The probes can be precisely positioned through the appropriate adjustment of screws and checking its position through a microscope. Throughout the measurements, a Profile Pro800 serves as the current source.

To measure the emission spectra (Figure C.1(a), the light emitted from the sample's cleaved facet is launched into a multimode glass fiber that is positioned at a distance of a few micrometers in front of the sample's cleaved output facet through appropriate adjustment of the xyz-table it is mounted on. The light is guided through the multimode glass fiber into a spectrum analyzer (Ando) with a double monochromator that can spectrally resolve the light in a wavelength

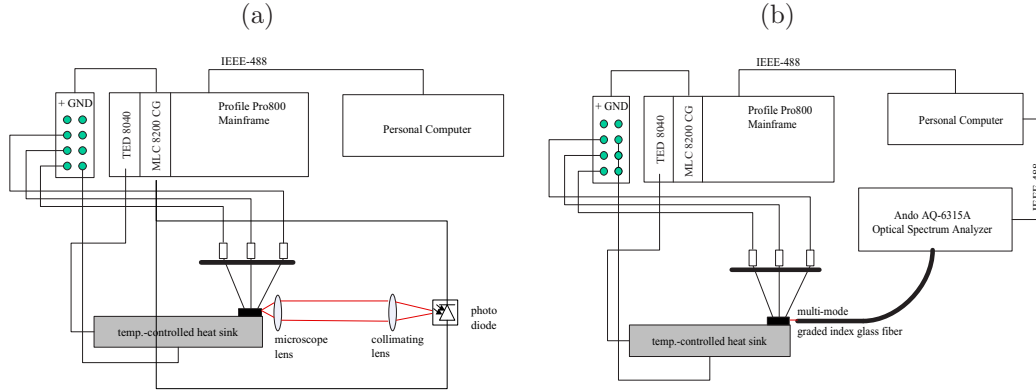(a)   (b)

Figure C.1: (a) Schematic of experimental setup to measure PI-characteristics continuous wave (cw) conditions (b) Schematic of experimental setup to measure the spectrum under cw conditions.

range from 350 nm to 1750 nm with a maximum resolution of 0.05 nm.

To measure the aggregate intensity of the emitted light and the voltage drop across the diode as a function of the injection current into the laser diode, i.e. the laser characteristics, the light is collected by a microscope lens with a numerical aperture of 0.5 and converted into a photocurrent using an InGaAs photodiode. The photodiode can detect light of wavelengths in the range of 1.55 μm with a maximum power of 15 mW.

 In many cases, it is interesting to investigate effects the properties of a semiconductor laser in the absence of ohmic heating in the laser. The heating occurs as during continuous operation, the heat generated in the device cannot timely dissipate into the heat sink. The thermal heating significantly alters the laser's device characteristics. If the sample is instead driven with a pulsed source that applies a current in a certain time interval and no current in a time interval that is equal to the period minus the load time and the trigger rate which equals the load time divided by the period of the signal is chosen sufficiently small, the heat has sufficient time to dissipate into the heat sink during the time intervals where no current is injected.

Figure C.2(a) shows a schematic of the pulsed laser measurement setup. Also here, the sample is fixated onto the Peltier controlled heat sink by applying a low pressure channel in pores located under the sample. The heat sink again

serves as the n-contact and probers that connect to the sample's p-contacts close the circuit. A current source (HP8814A) generates current pulses of up to 2 A at variable periods and duty cycles. The light emitted from the laser is focused onto a beam splitter (BS). One part of the light is launched onto a photodiode whereas the other part is focused onto a glass fiber. The photocurrent of the photodiode is integrated in a boxcar amplifier, that is triggered via the pulser and read into the computer through a multimeter. Through a second boxcar integrator, the voltage drop across the diode is measured for the calculation of the injected current. The light that has been launched into the glass fiber is guided to a spectrum analyzer where it is spectrally resolved.

C.2   Dynamic laser properties: Relative intensity noise and linewidth

A schematic of the measurement setup of RIN can be seen in Figure C.2. Using brackets, the sample is placed on a heat sink that is cooled by a Peltier element located under the sample holder surface which serves as the n-contact. A microscope is used to precisely position the electric probes on the sample's p-contact. The device is operated under stationary bias conditions, i.e. no change of injection currents into the various resonators of the device. The light of the laser is launched into a lensed single mode fiber. The lens-like entry facet of the fiber improves the coupling efficiency into the fiber and reduces back reflections into the laser cavity. The remaining back reflections off the measurement instruments are reduced by inserting an optical isolator into the light path. The light is detected with a fast photodiode whose signal is separated into its frequency components from 100 kHz to 22 GHz using a lightwave signal analyzer HP70004.

 In order to determine the intensity noise of the laser signal, one has to independently determine the noise of the measurement setup and the spectrum analyzer in particular. The main contributions to the noise of the spectrometer are the shot noise of the current from the photodiodes and thermal noise of the amplifier. The shot noise is simply due to the quantum nature of light and independent from the frequency and temperature of the laser. At high frequencies, the noise level
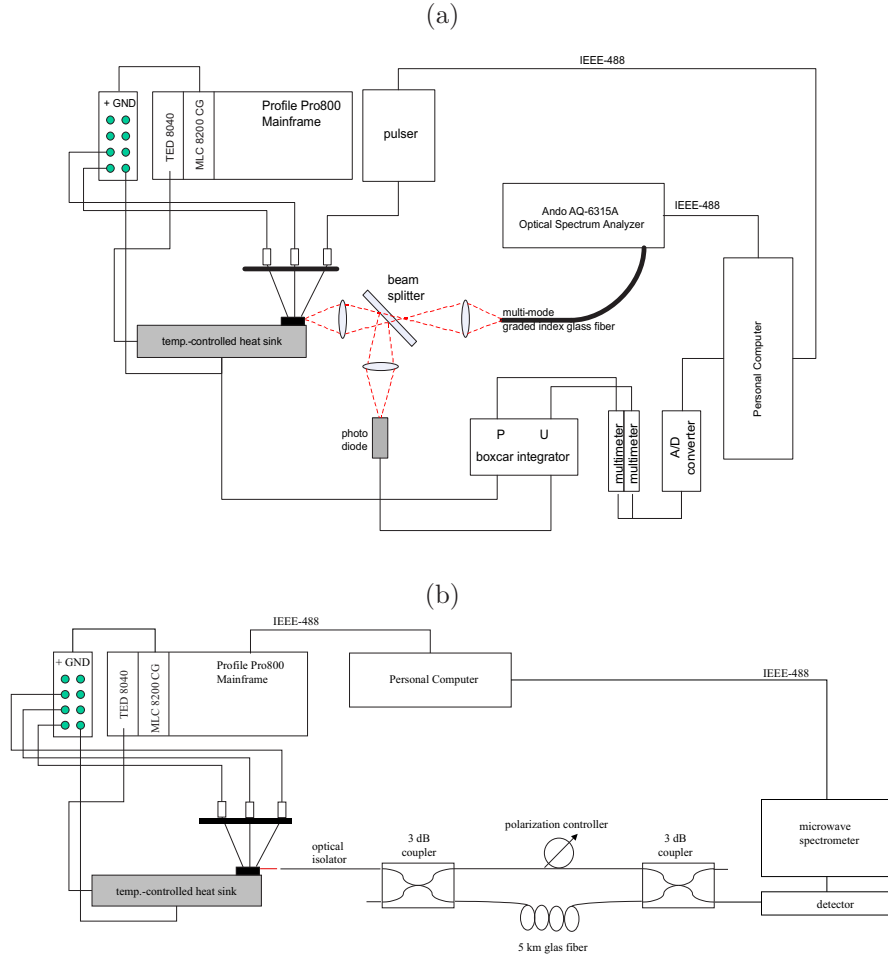
(a)

(b)

Figure C.2: (a) Schematic of experimental setup to measure PI-characteristics and spectrum under pulsed pumping conditions (b) Schematic of experimental setup to measure the linewidth of a laser.

always drops to the shot noise level of the photo detector. In order to subtract these two noise sources from the aggregate measurement, the noise level of the measurement setup is detected prior to each measurement and then subtracted from the aggregate measurement to obtain the true intensity noise from the laser source.

The setup for the measurement of the laser linewidth is very similar to the setup for the measurement of the RIN. The linewidth is detected using the self-homodyne method after which the signal is split into two components. One path is delayed using a delay line realized through a 50 km long fiber path, and then

coupled back to the second path.

Another setup allows the measurement of the laser's response to a electrical signal that has been modulated with a high frequency, the so called small signal response (SSR). Here, the current is injected into the laser diode through a clamp with three pins that are 500 μm apart. The center pin carries the signal and is bracketed by to pins that are connected to ground. In order to facilitate a contact between the outer pins with the n-contact of the heat sink, a small Zn plate is used to overcome the height difference between the sample surface and the heat sink. In a laser designed optimized for high frequency modulation, one would etch mesas deep into the n-doped region of the laser and apply contacts for the ground pins.

C.3   Passive device characterization: transmission measurement

A schematic of the transmission spectroscopy measurement setup is displayed in Figure C.3(a). The light from an external tunable laser source is launched into a fiber polarization controller consisting of a sequence of polarizing filter, a $\lambda/4$- (quarter-wave) optical fiber coil, and a $\lambda/2$- (half-wave) optical fiber coil. The two fiber coils can be independently rotated along the longitudinal axis inducing stress in the fiber which results in birefringence through the photoelastic effect. The amount of birefringence is inversely proportional to the radius squared of the coil. Any desired 'wave plate' can be created through appropriate selection of coil diameter and number of coil turns.

The polarization control is similar to the Levèvre configuration[1]. Light with generally elliptical polarization state is incident on the linear polarizer where it is converted to a fixed linear polarization (LP) state. The half-wave plate (HWP) then rotates the linear polarization state to a desired orientation. The quarter-wave plate (QWP) finally converts the linear polarization state into any desired polarization state if required. The Stokes vector of light leaving this configuration

---

[1]In the Levèvre configuration, two quarter-wave plates are bracketing a half-wave plate
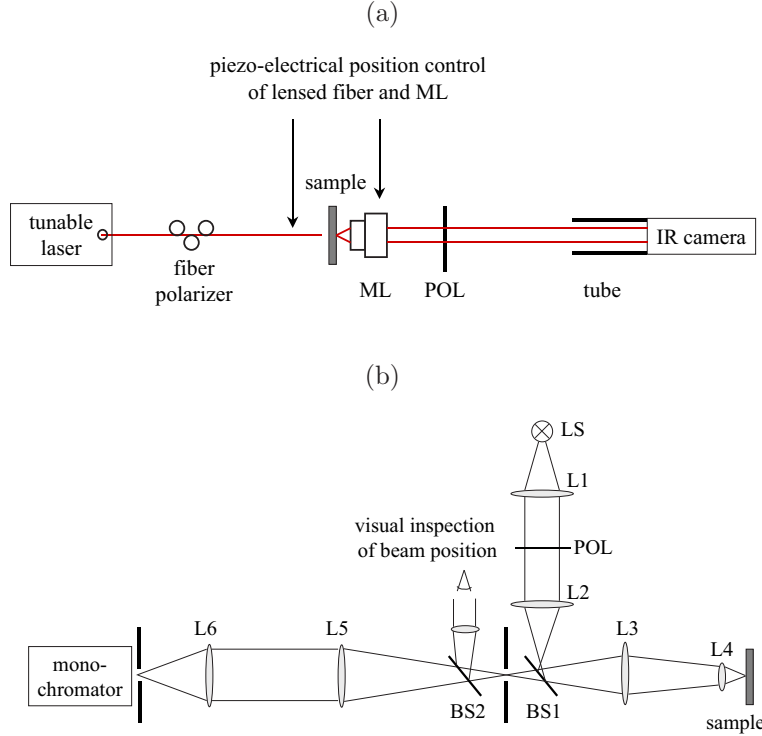
(a)

(b)

Figure C.3: (a) Schematic of experimental setup to measure the transmission through a passive waveguide structure (b) Schematic of experimental setup to measure the reflectance off a passive structure.

is therefore given by

$$\mathcal{S}^{(out)} = \mathcal{M}^{(HWP)} \cdot \mathcal{M}^{(QWP)} \cdot \mathcal{S}^{(LP)} \tag{C.1}$$

$$= \begin{pmatrix} 1 & 0 & 0 & 0 \\ 0 & \cos 4\gamma & \sin 4\gamma & 0 \\ 0 & \sin 4\gamma & -\cos 4\gamma & 0 \\ 0 & 0 & 0 & -1 \end{pmatrix} \cdot \begin{pmatrix} 1 & 0 & 0 & 0 \\ 0 & \cos^2 2\beta & \sin 2\beta \cos 2\beta & \sin 2\beta \\ 0 & \sin 2\beta \cos 2\beta & \sin^2 2\beta & -\cos 2\beta \\ 0 & -\sin 2\beta & \cos 2\beta & 0 \end{pmatrix}$$

$$\cdot \begin{pmatrix} 1 \\ \cos 1\alpha \\ \sin 2\alpha \\ 0 \end{pmatrix} = \begin{pmatrix} 1 \\ \frac{1}{2}\left[\cos\left(2\alpha - 4\beta + 4\gamma\right) + \cos\left(2\alpha - 4\gamma\right)\right] \\ \frac{1}{2}\left[\sin\left(2\alpha - 4\beta + 4\gamma\right) - \sin\left(2\alpha - 4\gamma\right)\right] \\ -\sin\left(2\alpha - 2\beta\right) \end{pmatrix}$$

where $\mathcal{M}^{(HWP)}$, $\mathcal{M}^{(QWP)}$, $\mathcal{S}^{(LP)}$, and $\mathcal{S}^{(out)}$ represent the Müller matrices of the half- and quarter-wave plates, and the Stokes vectors of the (linearly polarized) incident light and outgoing light, respectively. Throughout the experiments un-

dertaken in this work, the wave plates are rotated such that the outgoing light has maximum intensity in TE-polarization. It is very critical to note that the above described configuration to control the polarization state is highly wavelength sensitive and has to be re-adjusted when operating at a different wavelength.

The light which is now TE-polarized is leaving the lensed single mode glass fiber and enters the semiconductor access waveguide which has an initial width of typically 5 μm. The position of the lensed fiber can be adjusted through piezo-electric control elements in the x-, y, and z-directions. The light transmitted through the device is collimated using a microscope lens, filtered again to ensure the polarization state of the transmitted light is unchanged, and finally detected using a Hamamatsu frame grabber card that can digitize the image information to provide an absolute measure of the integrated number of photon counts in the frame grabber card besides providing information of the spatial intensity distribution.

Appendix D
Overview of Wafer Epitaxy

In this chapter, the epitaxial structure of the wafers used throughout this work is presented. As mentioned in chapter 3.1.1, the $In_xGa_{1-x}As_yP_{1-y}$ material system has two degrees of freedom. The free parameters x and y are chosen such to match the lattice constant of InP and the photoluminescence emission wavelength. All lasers are based on gas source molecular beam epitaxy grown InGaAsP quantum well structures with four or six compressively strained (1%) wells and lattice matched barriers. Separate confinement heterostructures are used for transversal photon confinement. In the following tables, the photoluminescence wavelength is given in brackets in μm.

The integrated active/ passive structure is fabricated by first growing a 300 nm thick passive layer onto the substrate by metal organic vapor phase epitaxy. The active /passive separation is then defined using optical lithography and subsequent dry etching of those areas targeted for the active structure. An 1.55 μm InGaAsP quantum well structure with six compressively strained (1%) wells separated by five quaternary lattice matched barriers, and a separate confinement heterostructure is grown between the passive areas by gas source molecular beam epitaxy. Finally, a common 1500 nm thick p-InP cladding and 200 nm thick In-GaAs contact layer ultimately result in a planar waveguide structure with active areas and adjacent passive areas.

A52980: Laser, λ=1530 nm, grown by GSMBE at Alcatel Research & Innovation, Groupement Opto+

p-contact layer	InGaAs (Q1.65)	150 nm	p=1.8 10^{19} cm^{-3}
p-intermediate layer	InGaAsP (Q1.17)	50 nm	p=7.8 10^{18} cm^{-3}
p-cladding	InP	1450 nm	p=1 10^{18} cm^{-3}
etch stop	InGaAs	5 nm	p=9.9 10^{17} cm^{-3}
p-cladding	InP	100 nm	p=1 10^{18} cm^{-3}
SCH	InGaAsP (Q1.17)	110 nm	undoped
SCH	InGaAsP (Q1.16)	10 nm	undoped
QW (4×)	InGaAsP (Q1.55)	5.6 nm	undoped
barrier (3×)	InGaAsP (Q1.16)	10 nm	undoped
SCH	InGaAsP (Q1.16)	10 nm	undoped
SCH	InGaAsP (Q1.17)	110 nm	undoped
buffer	InP	500 nm	n=2 10^{18} cm^{-3}
substrate	InGaAs (Q1.65)		n+

A52406: Laser, λ=1530 nm, grown by GSMBE at Alcatel Research & Innovation, Groupement Opto+

p-contact layer	InGaAs (Q1.65)	150 nm	p=2.4 10^{19} cm^{-3}
p-intermediate layer	InGaAsP (Q1.17)	50 nm	p=1 10^{19} cm^{-3}
p-cladding	InP	1655 nm	p=1 10^{18} cm^{-3}
SCH	InGaAsP (Q1.17)	50 nm	undoped
SCH	InGaAsP (Q1.16)	9.4 nm	undoped
QW (4×)	InGaAsP (Q1.55)	5.7 nm	undoped
barrier (3×)	InGaAsP (Q1.16)	9.4 nm	undoped
SCH	InGaAsP (Q1.16)	9.4 nm	undoped
SCH	InGaAsP (Q1.17)	50 nm	undoped
buffer	InP	500 nm	n=2 10^{18} cm^{-3}
substrate	InGaAs (Q1.65)		n+

A31136X/Y: integrated active/passive laser structure, λ=1530 nm, grown by GSMBE at Alcatel Research & Innovation, Groupement Opto+

p-contact layer	InGaAs (Q1.65)		150 nm		p=2.5 10^{19} cm^{-3}
p-interm. lay.	InGaAsP (Q1.17)		50 nm		p=1 10^{19} cm^{-3}
p-cladding	InP		1500 nm		p=2 10^{18} cm^{-3}
common layer	InP	150 nm	InP	150 nm	p=1 10^{18} cm^{-3}
SCH	InGaAsP (Q1.17)	45 nm			undoped
QW (6×)	InGaAsP (Q1.55)	8 nm	InGaAsP (Q1.4)	300 nm	undoped
barrier (5×)	InGaAsP (Q1.16)	10 nm			undoped
SCH	InGaAsP (Q1.17)	45 nm			undoped
buffer	InP	812 nm	InP	700 nm	n=1 10^{18} cm^{-3}
substrate	InP				n+
	← **active (1.5 mm)** →		← **passive (1 mm)** →		

Appendix E
Publication List

Parts of this work have already been published as shown in the following list.

1. S. Mahnkopf, M. Kamp, A. Forchel, and R. März
   'Tunable distributed feedback laser with photonic crystal mirrors'
   Appl. Phys. Lett., vol. 82, no. 18, pp. 2942-2944, May 2003

2. S. Mahnkopf, M. Kamp, A. Forchel, and R. März
   'Tunable distributed feedback laser with photonic crystal mirrors'
   Virt. J. of Nanoscale Science & Technology, vol. 7, Iss. 19, May 2003

3. S. Mahnkopf, M. Kamp, R. März, and A. Forchel
   'Unidirectional ring laser diode with gain-coupled distributed feedback'
   Electronics Letters, vol. 39, no. 14, pp. 1055-1056, Jul. 2003

   also discussed in 'Single-mode ring laser diode emits stably and unidirectionally'
   Laser Focus World, vol. 39, no. 10, p. 11, Oct. 2003

4. S. Mahnkopf, R. März, M. Kamp, V. Colson, G.-H. Duan, and A. Forchel
   'Wavelength switching by mode interference of coupled cavities with photonic crystal reflectors'
   Appl. Phys. B, vol. 77, no. 8, pp. 733-737, Dec. 2003

5. S. Mahnkopf, H. Hsin, G.-H. Duan, F. Lelarge, T.D. Happ, M. Kamp, R. März and A. Forchel
   'Wavelength switching by mode interference between longitudinally coupled photonic crystal channel waveguides'
   Electronics Letters, vol. 40, no. 1, pp. 29-30, Jan. 2004

   also discussed in 'Photonic-crystal laser has selectable wavelength'
   Laser Focus World, vol. 40, no. 3, pp. 42-43, Mar. 2004

6.   S. Mahnkopf, M. Arlt, M. Kamp, V. Colson, G.-H. Duan, and A. Forchel
   'Two channel tunable laser diode based on photonic crystals'
   IEEE Photonics Technol. Lett., vol. 16, no. 2, pp. 353-355, Feb. 2004

7.   M. Kamp, T. Happ, S. Mahnkopf, G. Duan, S. Anand, and A. Forchel
   'Semiconductor photonic crystals for optoelectronics'
   Physica E - Low-dimensional systems & nanostructures, vol. 21, nos. 2-4,
   pp. 802-808, Mar. 2004

8.   S. Mahnkopf, M. Kamp, M. Arlt, R. März, F. Lelarge, G.-H. Duan, and A.
   Forchel
   'Widely tunable complex-coupled distributed feedback laser with photonic
   crystal mirrors and integrated optical amplifier'
   IEEE Photonics Technol. Lett., vol. 16, no. 3, pp. 729-731, Mar. 2004

9.   S. Mahnkopf, M. Kamp, R. März, G.-H. Duan, V. Colson, and A. Forchel
   'Integration of active and passive photonic crystal based optoelectronic com-
   ponents'
   SPIE Proc., vol. 5360, pp. 24-33, Jul. 2004

10.   S. Mahnkopf, M. Kamp, A. Forchel, F. Lelarge, G.-H. Duan, and R. März
   'Mode anti-crossing and carrier transport effects in tunable photonic crystal
   coupled cavity lasers'
   Optics Communications, vol. 239, nos. 1-3, pp. 187-191, Sep. 2004

11.   S. Mahnkopf, R. März, M. Kamp, G.-H. Duan, F. Lelarge, and A. Forchel
   'Tunable photonic crystal coupled cavity laser'
   IEEE J. of Quantum Electron., vol. 40, no. 9, pp. 1306-1314, Sep. 2004

12.   M. Kamp, S. Mahnkopf, A. Forchel, G.-H. Duan, and S. Anand
   'Technology and properties of photonic-crystal-based active and passive op-
   toelectronic devices'
   SPIE Proc., vol. 5597, pp. 97-101, Oct. 2004

13.   S. Mahnkopf, J. Khoo, H. Scherer, M. Kamp, O. Toader, S. John, and A.
   Forchel

'Demonstration of unidirectional photonic bandgap based on three-dimensional photonic crystal structure with slanted pore topology'
to be submitted

14. *Invited Paper*: S. Mahnkopf, R. März, M. Kamp, and A. Forchel
'From single laser diodes to active and passive integrated optoelectronic components based on photonic crystals'
OSA Integrated Photonics Research and Applications, San Diego, Apr. 2005

Patents (rights reserved to Infineon Technologies AG)

15. S. Mahnkopf and R. März
'Tunable semiconductor laser and production method'
US Patent Application US 2004/0125832 A1

16. R. März and S. Mahnkopf
'Widely tunable laser based on contra-directionally coupled photonic crystal channel waveguides with intrinsically defined chirped superstructure'
Patent application, filed May 2004

Books / Book Chapters

17. M. Kamp, T. Happ, S. Mahnkopf, A. Forchel, S. Anand, and G.-H. Duan
'Photonic crystal based active optoelectronic devices'
in 'Photonic Crystals - Advances in Design, Fabrication, and Characterization',
Wiley-VCH, Edited by K. Busch, S. Lölkes, R.B. Wehrspohn, H. Föll
ISBN 3-527-40432-5

Bibliography

[Acker1998]   D.A. Ackerman, L.M. Zhang, L.J-P. Ketelsen, J.E. Johnson, "Characterizing residual reflections within semiconductor lasers, integrated sources, and coupling optics," IEEE J. Quantum Electron., vol. QE-34, no. 7, pp. 1224-1230 (1998)

[Agio2002]   M. Agio, *Optical properties and wave propagation in semiconductor-based two-dimensional photonic crystals*, Dissertation, University of Pavia and Iowa State University (2002)

[Arlt2003]   M. Arlt, *Abstimmbare Laser auf Basis photonischer Kristalle*, Thesis, Bayerische Julius-Maximilians-Universität, Würzburg, Germany (2003)

[Avr1998]   I.A. Avrutsky, D.S. Ellis, A. Tager, H. Anis, J.M. Xu, "Design of widely tunable semiconductor lasers and the concept of binary superimposed gratings (BSG's)," IEEE Journal of Quant. El., vol. 34, no. 4, pp. 729-741 (1998)

[Bach2001]   L. Bach, J.P. Reithmaier, A. Forchel, J.L. Gentner, and L. Goldstein, "Multiwavelength laterally complex coupled distributed feedback laser arrays with monolithically integrated combiner fabricated by focused-ion-beam lithography," Appl. Phys. Lett., vol. 79, no. 15, pp. 2324-2326 (2001)

[Baba2001]   T. Baba and D. Ohsaki, "Interfaces of photonic crystals for high efficiency light transmission," Jpn. J. Appl. Phys., vol. 40, no. 10, pp. 5920-5924 (2001)

[Baba2002a]   T. Baba and T. Matsumoto, "Resolution of photonic crystal superprism," Appl. Phys. Lett., vol. 81, no. 13, pp. 2325-2327 (2002)

[Baba2002b]   T. Baba and M. Nakamura, "Photonic crystal light deflection devices using the superprism effect," IEEE J. Quantum Electron., vol. 38, no. 7, pp. 909-914 (2002)

[Baba2004]   T. Matsumoto and T. Baba, "Design and FDTD simulation of photonic crystal k-vector superprism," IEICE Trans. Electron., vol. E87-C, no. 3, pp. 393-397 (2004)

[Baets2003]   W. Bogaerts, P. Bienstman, R. Baets, "Sidewall Roughness in Photonic Crystal Slabs: A Comparison of High-Contrast Membranes and Low-Contrast III-V Epitaxial Structures," European Conference on Integrated Optics (ECIO), Czech Republic, p.349-352 (2003)

[Baets2004]   L. H. Frandsen, P. I. Borel, Y. X. Zhuang, A. Harpøth, M. Thorhauge, M. Kristensen, W. Bogaerts, P. Dumon, R. Baets, V. Wiaux, J. Wouters, and S. Beckx, "Ultralow-loss 3-dB photonic crystal waveguide splitter," Optics Letters, vol. 29, no. 14, pp. 1623-1625 (2004)

[Bay2000]   M. Bayindir, B. Temelfuran, and E. Özbay, "Tight-binding description of the
             coupled defect modes in three-dimensional photonic crystals," Phys. Rev. Lett.,
             vol. 84, no. 10, pp. 2140-2143 (2000)

[Ben1999]   H. Benisty, C. Weisbuch, D. Labilloy, M. Rattier, C.J.M. Smith, T.F. Krauss,
             R.M. De la Rue, R. Houdre, U. Oesterle, C. Jouanin, D. Cassagne, "Optical
             and confinement properties of two-dimensional photonic crystals," J. Lightwave
             Tech., vol. 17, no. 11, pp. 2063-2077 (1999)

[Ben2000]   H. Benisty, D. Labilloy, C. Weisbuch, C.J.M. Smith, T.F. Krauss, D. Cas-
             sagne, A. Béraud, and C. Jouanin, "Radiation losses of waveguide-based two-
             dimensional photonic crystals: Positive role of the substrate," Appl. Phys. Lett.,
             vol. 76, no. 5, pp. 532-534 (2000)

[Ben2002]   H. Benisty, S. Olivier, C. Weisbuch, M. Agio, M. Kafesaki, C.M. Soukoulis,
             M. Qiu, M. Swillo, A. Karlsson, B. Jaskorzynska, A. Talneau, J. Moosburger,
             M. Kamp, A. Forchel, R. Ferrini, R. Houdre, U. Oesterle, "Models and mea-
             surements for the transmission of submicron-width waveguide bends defined in
             two-dimensional photonic crystals," IEEE J. Quantum Electron., vol. 38, no. 7,
             pp. 770-785 (2002)

[Ber1994]   J. P. Berenger, 'A perfectly matched layer for the absorption of electromagnetic
             waves,' J. Comp. Phys., vol. 114, no. 2, pp. 185-200 (1994)

[Ber2002]   M.Csörnyei, T.Berceli, T.Bánky, T.Marozsák, P.R.Herczfeld, "A new approach
             for RIN peak and phase noise suppression in microchip lasers", International
             Microwave Symposium IMS2002, Seattle, USA, June 2-7, pp.1377-1380 (2002)

[Bra1994]   C. Braagaard, B. Mikkelsen, T. Durhuus, K.E. Stubkjaer, "Modeling the dy-
             namics of wavelength tuning in DBR-lasers," IEEE Photon. Technol. Lett., vol.
             6, no. 6, pp. 694-696 (1994)

[Chu1971]   R.S. Chu and T. Tamir, "," Electron. Lett., vol. 7, no. , pp. 410-411 (1971)

[Chung2002] K.B. Chung and S.W. Hong, "Wavelength demultiplexers based on the super-
             prism phenomena in photonic crystals," Appl. Phys. Lett., vol. 81, no. 9, pp.
             1549-1551 (2002)

[Chut2000]   A. Chutinan and S. Noda, "Waveguides and waveguide bends in two-dimensional
             photonic crystal slabs," Phys. Rev. B, vol. 62, no. 7, pp. 4488-4492 (2000)

[Chut2003]   A. Chutinan, S. John, and O. Toader, "Diffractionless flow of light in all-optical
             microchips," Phys. Rev. Lett., vol. 90, no. 12, pp. 123901-1-4 (2003)

[Col1993]   V. Jayaraman, A. Mathur, L.A. Coldren, P. D. Dapkus, "Extended tuning range
             in sampled grating DBR lasers," IEEE Photon. Techn. Lett., vol. 5, no. 5, pp.
             489-491 (1993)

[Col1995]   L.A. Coldren and S.W. Corzine, *Diode lasers and photonic integrated circuits*, John Wiley & Sons, ISBN 0-471-11875-3 (1995)

[Col1998]   B. Mason, G.A. Fish, S.P. DenBaars, L. A. Coldren, "Ridge waveguide sampled grating DBR lasers with 22-nm quasi-continuous tuning range," IEEE Phot. Techn. Lett., vol. 10, no. 9, pp. 1211-1213 (1998)

[Col1999]   B. Mason, G.A. Fish, S.P. DenBaars, L. A. Coldren, "Widely tunable sampled grating DBR laser with integrated electroabsorption modulator," IEEE Phot. Techn. Lett., vol. 11, no. 6, pp. 638-640 (1999)

[Del1998a]   F. Delorme, G. Alibert, C. Ougier, S. Slempkes, H. Nakajima, "Sampled-grating DBR lasers with 101 wavelengths over 44nm and optimised power variation for WDM applications," Electr. Lett., vol. 34, no. 3, pp. 279-281 (1998)

[Del1998b]   F. Delorme, "Widely tunable 1.55-mu m lasers for wavelength-division multiplexed optical fiber communications," IEEE Journal of Quant. El., vol. 34, no. 9, pp. 1706-1716 (1998)

[Eich2002]   G. Böttger, C. Liguda, M. Schmidt, and M. Eich, "Improved transmission characteristics of moderate refractive index contrast photonic crystal slabs," Appl. Phys. Lett., vol. 81, no. 14, pp. 2517-2519 (2002)

[Fan2002]   W.T. Lau and S. Fan, "Creating large bandwidth line defects by embedding dielectric waveguides into photonic crystal slabs," Appl. Phys. Lett., vol. 81, no. 21, pp. 3915-3917 (2002)

[Gaug1997]   H.-P. Gauggel, H. Artmann, C. Geng, F. Scholz, and H. Schweizer, "Wide-range tunability of GaInP-AlCaInP DFB lasers with superstructure gratings," IEEE Phot. Techn. Lett., vol. 9, no. 1, pp. 14-16 (1997)

[Happ2001]   T.D. Happ, A. Markard, M. Kamp, A. Forchel, A. Patel, S. Anand, J.-L. Gentner, N. Bouadma, "Nanofabrication of two-dimensional photonic crystal mirrors for 1.5 mu m short cavity lasers," J. Vac. Sci. Technol. B, vol. 19, no. 6, pp. 2775-2778 (2001)

[Happ2002]   T.D. Happ, *Zweidimensionale Photonische Kristalle: Untersuchungen zu Defektkavitäten und optoelektronischen Bauelementen*, Dissertation, Bayerische Julius-Maximilians-Universität, Würzburg, Germany (2002)

[Happ2003]   T.D. Happ, M. Kamp, A. Forchel, J.L. Gentner, L. Goldstein, "Two-dimensional photonic crystal coupled-defect laser diode," Appl. Phys. Lett., vol. 82, no. 1, pp. 4-6 (2003)

[Ho1990]   K.M. Ho, C.T. Chan, and C.M. Soukoulis, "Existence of a photonic gap in periodic dielectric structures," Phys. Rev. Lett., vol. 65, no. 25, 3152-3155 (1990)

[Hofst1998]   D. Hofstetter and R.L. Thornton, "Measurement of optical cavity properties in semiconductor lasers by Fourier analysis of the emission spectrum," IEEE J. Quantum Electron., vol. QE-34, no. 10, pp. 1914-11923 (1998)

[Hun1998]   E.H. Huntington, B.C. Buchler, C.C. Harb, T.C. Ralph, D.E. McClelland, and H.-A. Bachor, "Feedback control of the intensity noise of injection locked lasers," Opt. Comm., vol. 145, no. 1, pp. 359-366 (1998)

[Jay1993]   V. Jayaraman, Z.-M. Chuang, L.A. Coldren, "Theory, design, and performance of extended tuning range semiconductor-lasers with sampled gratings," IEEE Journal of Quant. El., vol. 29, no. 6, pp. 1824-1834 (1993)

[Joa1995]   J.D. Joannopoulos, R.D. Meade, J.N. Winn, *Photonic Crystals: Molding the flow of light.* Princeton: Princeton University Press (1995)

[Joa2004]   C. Luo, M. Soljačić, and J.D. Joannopoulos, "Superprism effect based on phase velocities," Opt. Lett., vol. 29, no. 7, pp. 745-747 (2004)

[John1987]   S. John, "Strong localization of photons in certain disordered dielectric super-lattices," Phys. Rev. Lett., vol. 58, no. 23, pp. 2486-2489 (1987)

[Johns2001]   S.G. Johnson, J.D. Joannopoulos, "Block-iterative frequency-domain methods for Maxwell's equations in a planewave basis," Optics Express, vol. 8, no. 3, pp. 173-190, Jan. 2001, the program code can be freely downloaded at http://ab-initio.mit.edu/mpb/

[Kamp]   M. Kamp, Transfer matrix and 2D finite difference time domain algorithms in C++ code, E-Mail: martin.kamp@physik.uni-wuerzburg.de

[Kamp1999]   M. Kamp, J. Hofmann, F. Schäfer, A. Forchel, and J.P. Reithmaier, "Low-threshold high-quantum-efficiency laterally gain-coupled InGaAs/AlGaAs distributed feedback lasers," Appl. Phys. Lett., vol. 74, no. 4, pp. 483-485 (1999)

[Kos1998]   H. Kosaka, T. Kawashima, A. Tomita, M. Notomi, and T. Tamamura, "Super-prism phenomena in photonic crystals," Phys. Rev. B, vol. 58, no. 16, pp. R10 96-99 (1998)

[Kos1999]   H. Kosaka, T. Kawashima, A. Tomita, M. Notomi, T. Tamamura, T. Sato, and S. Kawakami, "Self-collimating phenomena in photonic crystals," Appl. Phys. Lett., vol. 74, no. 9, pp. 1212-1214 (1999)

[Krau2002]   L. Wu, M. Mazilu, T. Karle, and T.F. Krauss, "Superprism phenomena in planar photonic crystals," IEEE J. Quantum Electron., vol. 38, no. 7, pp. 915-918 (2002)

[Krau2003]   L. Wu, M. Mazilu, J.-F. Gallet, and T.F. Krauss, "Square-lattice photonic crystal collimator," Photon. and Nanostr., vol. 1, no. 1, pp. 915-918 (2003)

[Krau2004]   T.F. Krauss, "Photonic crystal waveguides (Invited Paper)," Photonics West Conference SPIE, San Jose, 24-29 January (2004)

[Lee2002]   H.G. Park, J.K. Hwang, J. Huh, H.Y. Ryu, S.H. Kim, J.S. Kim, Y.H. Lee, "Characteristics of modified single-defect two-dimensional photonic crystal lasers," IEEE J. Quantum Electron., vol. QE-38, no. 10, pp. 1353-1365 (2002)

[Leung1990]   K. Leung and Y. Liu, "Full vector wave calculation of photonic band structures in face-centered-cubic dielectric media," Phys. Rev. Lett., vol. 65, no. 21, pp. 2646-2649 (1990)

[Lin1996]   S.-Y. Lin, V.M. Hietala, L. Wang, and E.D. Jones, "Highly dispersive photonic band-gap prism," Opt. Lett., vol. 21, no. 21, pp. 1771-1773 (1996)

[Lin2003]   Y. Xu, W. Liang, A. Yariv, J.G. Fleming, S.Y. Lin, "High-quality-factor Bragg onion resonators with omnidirectional reflector cladding," Opt. Lett., vol. 28, no. 22, pp. 2144-2146 (2003)

[Mah1998]   S. Mahnkopf, *Effects of optical feedback on the quantum noise properties of semiconductor lasers*, Thesis, University of Miami (1998)

[März1995]   R. März, *Integrated Optics: Design and Modeling* Norwood: Artech House, pp. 201-210 (1995)

[März2000]   R. März, G. Hilliger, "On the transfer matrix theory of contradirectional devices," Opt. Quantum Electron., vol. 32, no. 6-8, pp. 829-842 (2000)

[Mekis1996]   A. Mekis, J.C. Chen, I. Kurland, S. Fan, P.R. Villeneuve, J.D. Joannopoulos, "High transmission through sharp bends in photonic crystal waveguides," Phys. Rev. Lett., vol. 77, no. 18, pp. 3787-3790 (1996)

[Mig2001]   H. Míguez, E. Chomski, F. García-Santamaría, M. Ibisate, S. John, C. López, F. Meseguer, J. P. Mondia, G. A. Ozin, O. Toader, H. M. van Driel, "Photonic bandgap engineering in germanium inverse opals by chemical vapor deposition," Adv. Mat., vol. 13, no. 21, pp. 1634-1637 (2001)

[Min2004]   S.F. Mingaleev and Y.S. Kivshar, "Self-trapping and stable localized modes in nonlinear photonic crystals," Phys. Rev. Lett., vol. 86, no. 24, pp. 5474-5477 (2001)

[Mor1999]   G. Sarlet, G. Morthier, and R. Baets, "Wavelength and mode stabilization of widely tunable SG-DBR and SSG-DBR lasers," IEEE Photon. Technol. Lett., vol. 11, no. 11, pp. 1351-1353 (1999)

[Muel2001]   M. Müller, M. Kamp, A. Forchel, J.-L. Gentner, "Wide-range-tunable laterally coupled distributed feedback lasers based on InGaAsP-InP," Appl. Phys. Lett., vol. 79, no. 17, pp. 2684-2686 (2001)

[Muel2004]   M. Müller, *Abstimmbare Halbleiterlaser und schmalbandige Laserarrays mit verteilter lateraler Rückkopplung*, Dissertation, Bayerische Julius-Maximilians-Universität Würzburg, Würzburg, Germany (2004)

[Neum1929]   J.v. Neumann and E. Wigner, "Über das Verhalten von Eigenwerten bei adiabatischen Prozessen," Phys. Zeitschr., vol. 30, pp. 467-470 (1929)

[Nod2000b]   S. Noda, A. Chutinan, M. Imada, "Trapping and emission of photons by a single defect in a photonic bandgap structure," Nature, vol. 407, no. 6804, pp. 608-610 (2000)

[Not2001]   M. Notomi, K. Yamada, A. Shinya, J. Takahashi, C. Takahashi, and I. Yokohama, "Extremely large group-velocity dispersion of line-defect waveguides in photonic crystal slabs," Phys. Rev. Lett., vol. 8725, no. 25, pp. 253902-1-4 (2001)

[Och2001a]   T. Ochiai and K. Sakoda, "Dispersion relation and optical transmittance of a hexagonal photonic crystal slab," Phys. Rev. B, vol. 63, no. 12, pp. 125107-1-7 (2001)

[Och2001b]   T. Ochiai and J. Sanchez-Dehesa, "Superprism effect in opal-based photonic crystals," Phys. Rev. B, vol. 64, no. 24, pp. 245113-1-7 (2001)

[Ol2001]   S. Olivier, M. Rattier, H. Benisty, C. Weisbuch, C.J.M. Smith, R.M. De la Rue, T.F. Krauss, U. Oesterle, R. Houdre, "Mini-stopbands of a one-dimensional system: The channel waveguide in a two-dimensional photonic crystal," Phys. Rev. B, vol. 63, no. 11, art. no. 113311 (2001)

[Ol2003]   S. Olivier, H. Benisty, C. Weisbuch, C.J.M. Smith, T.F. Krauss, and R. Houdre, "Coupled-mode theory and propagation losses in photonic crystal waveguides," Opt. Expr., vol. 11, no. 13, pp. 1490-1496 (2003)

[Öttl2001]   A. Öttl, *Ultra-refractive photonic crystals, colloidal opals, and photonic band gaps in the THz-range*, Thesis, Albert-Ludwigs-Universität, Freiburg, Germany (2001)

[Oug1996]   A. Talneau, C. Ougier, S. Slemkes, "Multiwavelength grating reflectors for widely tunable laser," IEEE Phot. Techn. Lett., vol. 8, no. 4, pp. 497-499 (1996)

[Oz1994]   E. Özbay, E. Michel, G. Tuttle, R. Biswas, M. Sigalas, and K.M. Ho, "Micromachined millimeter-wave photonic band-gap crystals," Appl. Phys. Lett., vol. 64, no. 16, pp. 2059-2061 (1994)

[Park2002]   W. Park and C.J. Summers, "Extraordinary refraction and dispersion in two-dimensional photonic-crystal slabs," Opt. Lett., vol. 27, no. 17, pp. 1397-1399 (2002)

[Pen1992]   J.B. Pendry and A. MacKinnon, "Calculation of photon dispersion relations," Phys. Rev. Lett, vol. 69, no. 19, pp. 2772-2775 (1992)

[Prost1997]   W. Prost, *Technologie der III/V-Halbleiter*, Springer-Verlag, Berlin, First Edition (1997)

[Reyn2000]   A.L. Reynolds, J.B. Pendry, P.M. Bell, A.J. Ward, and L.M. Moreno, "Translight," http://www.elec.gla.ac.uk/ãreynolds (2000)

[Rob1996]   K. Robbie and M.J. Brett, "Chiral sculptured thin films," Nature, vol. 384, no. 6610, pp. 616-616 (1996)

[Sak2001]   K. Sakoda, *Optical properties of photonic crystals.* Springer Verlag, Berlin (2001)

[Sar2002]   B.K. Saravanan, *Chromatic dispersion measurements in photonic crystal waveguides*, Thesis, Technische Universität Hamburg-Harburg, Germany (2002)

[Schatz1994]   R. Schatz, E. Berglind, and L. Gillner, "Parameter Extraction from DFB Lasers by Means of a Simple Expression for the Spontaneous Emission Spectrum," IEEE Photon. Techn. Lett., vol. 6, no. 10, pp. 1182-1184 (1994)

[Sche1999]   O. Painter, R.K. Lee, A. Scherer, A. Yariv, J.D. O'Brien, P.D. Dapkus, I. Kim, "Two-dimensional photonic bandgap defect mode laser," Science, vol. 284, no. 5421, pp. 1819-1821 (1999)

[Shevy1993]   Y. Shevy, J. Kitching, and A. Yariv, "Linewidth reduction and frequency stabilization of semiconductor laser with a combination of FM sideband locking and optical feedback," Opt. Lett., vol. 18, no. 13, pp. 1071-1073 (1993)

[Shevy1999]   Y. Shevy, H. Deng, S. Mahnkopf, J. Kitching, and A. Yariv, "Quantum noise limits of a semiconductor laser with dispersive optical feedback," SPIE Proc. 3611, pp. 56-64 (1999)

[Sig2004]   J.S. Jensen and O. Sigmund, "Systematic design of photonic crystal structures using topology optimization: low-loss waveguide bends," Appl. Phys. Lett., vol. 84, no. 12, pp. 2022-2024 (2004)

[Smith2002]   C.-H. Wang, L.R. Chen, and P.W.E. Smith, "Analysis of chirped-sampled and sampled-chirped fiber Bragg gratings," Applied Optics, vol. 41, no. 9, pp. 1654-1660 (2002)

[Sol2004]   M. Soljačić and J.D. Joannopoulos, "Enhancement of nonlinear effects using photonic crystals," Nature Materials, vol. 3, no. 4, pp. 211-219 (2004)

[Sold2002]   W. Soldner, *Untersuchung von gekrümmten Lichtwellenleitern in zweidimensionalen photonischen Kristallen auf der Basis von GaAs/AlGaAs*, Thesis, Bayerische Julius-Maximilians-Universität, Würzburg, Germany (2002)

[Tafl2000]   A. Taflove and S.C. Hagness, "Computational Electrodynamics: The Finite-Difference Time-Domain Method," Artech House, Boston, Second Edition (2000)

[Tal1999]   A. Talneau, M. Allovon, N. Bouadma, S. Slempkes, A. Ougazzaden, and H. Nakajima, "Agile and fast switching monolithically integrated four wavelength selectable source at 1.55 μm," IEEE Photonics Technol. Lett., vol. 11, no. 1, pp. 12-14 (1999)

[Tal2002]   A. Talneau, P. Lalanne, M. Agio, C.M. Soukoulis, "Low-reflection photonic-crystal taper for efficient coupling between guide sections of arbitrary widths," Optics Lett., vol. 27, no. 17, pp. 1522-1524 (2002)

[Toh1993a]   F. Kano, H. Ishii, Y. Tohmori, M. Yamamoto, Y. Yoshikuni, "Broad range wavelength switching in superstructure grating distributed-Bragg-reflector lasers," Electr. Lett., vol. 29, no. 12, pp. 1091-1092 (1993)

[Toh1993b]   Y. Tohmori, Y. Yoshikuni, H. Ishii, F. Kano, T. Tamamura, Y. Kondo, M. Yamamoto, "Broad-range wavelength-tunable superstructure grating (SSG) DBR lasers," IEEE Journal of Quant. El., vol. 29, no. 6, pp. 1817-1823 (1993)

[Toh1996]   H. Ishii, H. Tanobe, F. Kano, Y. Tohmori, Y. Kondo, Y. Yoshikuni, "Quasicontinuous wavelength tuning in super-structure-grating (SSG) DBR lasers," IEEE Journal of Quant. El., vol. 32, no. 3, pp. 433-441 (1996)

[Ward1996]   A.J. Ward, "Transfer Matrices, Photonic Bands and Related Quantities," Dissertation, University of London, London, United Kingdom (1996)

[Yabl1987]   E. Yablonovitch, "Inhibited spontaneous emission in solid-state physics and electronics," Phys. Rev. Lett., vol. 58, no. 20, pp. 2059-2062 (1987)

[Yariv1999] A. Yariv, Y. Xu, R.K. Lee, and A. Scherer, "Coupled resonator optical waveguide: a proposal and analysis," Opt. Lett., vol. 24, no. 11, pp. 711-713 (1999)

[Yee1966]   K. Yee, 'Numerical solutions of initial boundary value problems involving Maxwell's equations in isotropic media,' IEEE Transactions on Antennas and Propagation, vol. AP-14, pp. 302-307 (1966)

[Zhang1990] Z. Zhang and S. Satpathy, "Electromagnetic wave propagation in periodic structures: Bloch wave solution of Maxwell equations," Phys. Rev. Lett., vol. 65, no. 21, pp. 2650-2653 (1990)

Appendix F
Acknowledgments

Appendix G
Curriculum Vitae

Sven Mahnkopf was born in Berlin-Lichterfelde on April 2, 1973. He studied Physics at Berlin University of Technology, the University of Heidelberg, both Germany, and the University of Miami where he held a teaching assistantship. He obtained the M.Sc. degree in 1998 with an investigation on the effects of dispersive optical feedback on the quantum noise properties of semiconductor lasers, a work carried out with Prof. Shevy. He joined Infineon Technologies Pte. Ltd., Singapore and commenced his Ph.D. studies in collaboration with Infineon Technologies Corporate Research in 2000 focusing on the integration of active and passive optoelectronic devices based on photonic crystals.

Sven Mahnkopf held a Fulbright Grant in 1997 and is a member of SPIE and the European and German Physical Societies.

Ehrenwörtliche Erklärung

gemäß § 5 Abs. 2 Ziff. 2 und 5
der Promotionsordnung
der Fakultät für Physik und Astronomie
der Universität Würzburg

Hiermit erkläre ich ehrenwörtlich, daß ich die Dissertation selbständig und ohne die Hilfe eines Promotionsberaters angefertigt und keine anderen als die angegebenen Quellen und Hilfsmittel benutzt habe.

Die Dissertation wurde bisher weder vollständig noch teilweise einer anderen Hochschule mit dem Ziel, einen akademischen Grad zu erwerben, vorgelegt.

Am 1. Mai 1998 wurde mir von der University of Miami, Coral Gables, Florida, U.S.A. der akademische Grad Master of Science, verliehen. Dieser wurde am 1. Februar 2001 als Grundlage für die Anerkennung zur Promotion anerkannt. Weitere akademische Grade habe ich weder erworben noch versucht zu erwerben.

Würzburg, den 20. Januar 2005

Sven Mahnkopf